Side Impact Test and Analyses of a DOT-111 (CPC-1232) Tank Car

REPORT DOCUMENTATION PAGE

The public reporting burden for this collection of information is estimated to average 1 hour per response, including the time for reviewing instructions, searching existing data sources, gathering and maintaining the data needed, and completing and reviewing the collection of information. Send comments regarding this burden estimate or any other aspect of this collection of information, including suggestions for reducing the burden, to Department of Defense, Washington Headquarters Services, Directorate for Information Operations and Reports (0704-0188), 1215 Jefferson Davis Highway, Suite 1204, Arlington, VA 22202-4302. Respondents should be aware that notwithstanding any other provision of law, no person shall be subject to any penalty for failing to comply with a collection of information if it does not display a currently valid OMB control number.
PLEASE DO NOT RETURN YOUR FORM TO THE ABOVE ADDRESS.

1. REPORT DATE *(DD-MM-YYYY)* October 2020	2. REPORT TYPE Technical Report		3. DATES COVERED *(From - To)* October 30, 2018
4. TITLE AND SUBTITLE Side Impact Test and Analyses of a DOT-111 (CPC-1232) Tank Car		**5a. CONTRACT NUMBER** DTFR53-11-D-00008	
		5b. GRANT NUMBER	
		5c. PROGRAM ELEMENT NUMBER	
6. AUTHOR(S) Shaun Eshraghi* 0000-0002-8152-0838 Shawn Trevithick** 0000-0001-6155-5526 Michael Carolan* 0000-0002-8758-5739 Przemyslaw Rakoczy** 0000-0002-1924-7172 Nicholas Wilson** 0000-0003-1140-7108		**5d. PROJECT NUMBER**	
		5e. TASK NUMBER Task Order 008	
		5f. WORK UNIT NUMBER	
7. PERFORMING ORGANIZATION NAME(S) AND ADDRESS(ES) *Volpe National Transportation Systems Center 55 Broadway, Cambridge, MA 02142 **Transportation Technology Center, Inc. 55500 DOT Road, Pueblo, CO 81001		**8. PERFORMING ORGANIZATION REPORT NUMBER**	
9. SPONSORING/MONITORING AGENCY NAME(S) AND ADDRESS(ES) U.S. Department of Transportation Federal Railroad Administration Office of Railroad Policy and Development Office of Research, Development and Technology Washington, DC 20590		**10. SPONSOR/MONITOR'S ACRONYM(S)**	
		11. SPONSOR/MONITOR'S REPORT NUMBER(S) DOT/FRA/ORD-20/43	

13. SUPPLEMENTARY NOTES
COR: Francisco González, III

14. ABSTRACT
The Federal Railroad Administration (FRA) conducted a side impact test on a DOT-111 tank car at the Transportation Technology Center (TTC) to evaluate its performance under dynamic impact conditions, and to provide data for the verification and refinement of a computational model. The tank car was filled with water to approximately 95 percent of its volume and sealed, but not pressurized. The tank car was impacted at 13.9 mph by a 297,150-pound ram car with 12-inch by 12-inch ram head fitted to the ram car. The impact caused significant deformation of the tank and resulted in the failure of the tank wall under the right edge of the ram head. The crack that formed under the edge of the ram head continued to propagate vertically above and below the ram leading to a tear running from the bottom to the top of the reference grid painted on the side of the tank (about 8 ft.). The Volpe National Transportation Systems Center (Volpe) performed pre-test finite element (FE) modeling to estimate the overall response of the tank to the impact. This pre-test models gave results in good agreement with the test results. Researchers updated the post-test FE models to include the actual material behavior and to better represent the test setup. The post-test FE results were in even better agreement with the test results than the pre-test estimates.

The modeling and testing performed in this program demonstrate the ability of the fluid response of an impacted tank car to dominate the general force-displacement response, underscoring the importance of modeling the fluid-structure interactions with appropriate techniques. The intention of the test data is to be used to better understand the shell impact performance of the new specification DOT-111 tank car. The validated FE model can be used to examine additional impact scenarios beyond the tested scenario.

15. SUBJECT TERMS
Impact test, DOT-111 tank car, tank car performance, transportation safety, toxic by inhalation, TIH, finite element analysis, FEA, finite element, FE, hazardous materials, rolling stock

16. SECURITY CLASSIFICATION OF:			17. LIMITATION OF ABSTRACT	18. NUMBER OF PAGES	19a. NAME OF RESPONSIBLE PERSON Nicholas Wilson, Chief Scientist, TTCI
a. REPORT Unclassified	**b. ABSTRACT** Unclassified	**c. THIS PAGE** Unclassified		136	**19b. TELEPHONE NUMBER** *(Include area code)* 719-584-0573

METRIC/ENGLISH CONVERSION FACTORS

ENGLISH TO METRIC

LENGTH (APPROXIMATE)

1 inch (in)	=	2.5 centimeters (cm)
1 foot (ft)	=	30 centimeters (cm)
1 yard (yd)	=	0.9 meter (m)
1 mile (mi)	=	1.6 kilometers (km)

AREA (APPROXIMATE)

1 square inch (sq in, in^2)	=	6.5 square centimeters (cm^2)
1 square foot (sq ft, ft^2)	=	0.09 square meter (m^2)
1 square yard (sq yd, yd^2)	=	0.8 square meter (m^2)
1 square mile (sq mi, mi^2)	=	2.6 square kilometers (km^2)
1 acre = 0.4 hectare (he)	=	4,000 square meters (m^2)

MASS - WEIGHT (APPROXIMATE)

1 ounce (oz)	=	28 grams (gm)
1 pound (lb)	=	0.45 kilogram (kg)
1 short ton = 2,000 pounds (lb)	=	0.9 tonne (t)

VOLUME (APPROXIMATE)

1 teaspoon (tsp)	=	5 milliliters (ml)
1 tablespoon (tbsp)	=	15 milliliters (ml)
1 fluid ounce (fl oz)	=	30 milliliters (ml)
1 cup (c)	=	0.24 liter (l)
1 pint (pt)	=	0.47 liter (l)
1 quart (qt)	=	0.96 liter (l)
1 gallon (gal)	=	3.8 liters (l)
1 cubic foot (cu ft, ft^3)	=	0.03 cubic meter (m^3)
1 cubic yard (cu yd, yd^3)	=	0.76 cubic meter (m^3)

TEMPERATURE (EXACT)

[(x-32)(5/9)] °F = y °C

METRIC TO ENGLISH

LENGTH (APPROXIMATE)

1 millimeter (mm)	=	0.04 inch (in)
1 centimeter (cm)	=	0.4 inch (in)
1 meter (m)	=	3.3 feet (ft)
1 meter (m)	=	1.1 yards (yd)
1 kilometer (km)	=	0.6 mile (mi)

AREA (APPROXIMATE)

1 square centimeter (cm^2)	=	0.16 square inch (sq in, in^2)
1 square meter (m^2)	=	1.2 square yards (sq yd, yd^2)
1 square kilometer (km^2)	=	0.4 square mile (sq mi, mi^2)
10,000 square meters (m^2)	=	1 hectare (ha) = 2.5 acres

MASS - WEIGHT (APPROXIMATE)

1 gram (gm)	=	0.036 ounce (oz)
1 kilogram (kg)	=	2.2 pounds (lb)
1 tonne (t)	=	1,000 kilograms (kg)
	=	1.1 short tons

VOLUME (APPROXIMATE)

1 milliliter (ml)	=	0.03 fluid ounce (fl oz)
1 liter (l)	=	2.1 pints (pt)
1 liter (l)	=	1.06 quarts (qt)
1 liter (l)	=	0.26 gallon (gal)
1 cubic meter (m^3)	=	36 cubic feet (cu ft, ft^3)
1 cubic meter (m^3)	=	1.3 cubic yards (cu yd, yd^3)

TEMPERATURE (EXACT)

[(9/5) y + 32] °C = x °F

QUICK INCH - CENTIMETER LENGTH CONVERSION

0	1	2	3	4	5

Inches

Centimeters

0	1	2	3	4	5	6	7	8	9	10	11	12	13
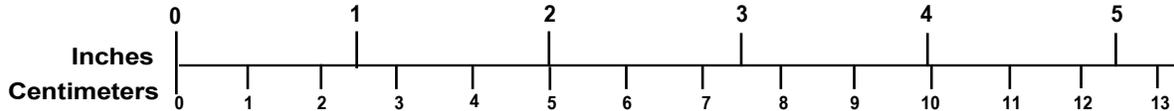
QUICK FAHRENHEIT - CELSIUS TEMPERATURE CONVERSIO

°F	-40°	-22°	-4°	14°	32°	50°	68°	86°	104°	122°	140°	158°	176°	194°	212°
°C	-40°	-30°	-20°	-10°	0°	10°	20°	30°	40°	50°	60°	70°	80°	90°	100°
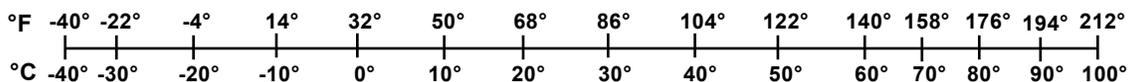
For more exact and or other conversion factors, see NIST Miscellaneous Publication 286, Units of Weights and Measures. Price $2.50 SD Catalog No. C13 10286

Updated 6/17/98

Acknowledgements

Contents

Illustrations

Tables

Executive Summary

The tests and analyses described in this report support the overall objective of the Federal Railroad Administration (FRA) research program to improve transportation safety for tank cars. This report documents the combined efforts of Transportation Technology Center, Inc. (TTCI) and the Volpe National Transportation Systems Center (Volpe) to test and analyze the side impact puncture performance of a DOT-111A100W1 (DOT-111) tank car that meets voluntary industry standard CPC-1232. FRA conducted the side impact test on October 30, 2018, at the Transportation Technology Center to evaluate the performance of the tank car and to provide data for the validation and refinement of a computational model. All test requirements were met. Volpe performed both pre-test and post-test analyses of the impact response to evaluate and improve the puncture modeling capabilities of modeling tank car puncture involving fluid-structure interaction and material failure.

The tank car was filled with water to approximately 95 percent of its volume. It was then sealed but not pressurized, leaving the 5 percent outage at atmospheric pressure. Pre-test modeling estimated a puncture range between 11 and 15 mph, depending on the specific material properties of the steel making up its shell. Based on these results, the target test speed was 13.5 mph +/-0.5 mph. The tank car was impacted by a 297,150-pound ram car traveling at 13.9 mph. A 12-inch by 12-inch indenter fitted to the ram car impacted the tank center. The impact caused significant deformation of the tank and resulted in the failure of the tank wall under the right edge of the indenter. The crack that formed under the edge of the indenter continued to propagate vertically above and below the ram leading to a tear running from the bottom to the top of the reference grid painted on the side of the tank (~8 feet).

The use of the pre-test finite element (FE) modeling was to estimate the overall response of the tank to the impact, including the force-displacement response. Pre-test material behavior for the TC128 shell of the car was estimated using information gathered from previous tensile tests of other samples of TC128 steel.

After the test, material coupons were cut from the tank car shell and subjected to tensile testing. The update of the post-test FE model included the actual material behavior. Volpe ran the post-test model using several conditions for the outage to help investigate the effects of water leakage through the manway and top fittings that were observed during the test.

1. Introduction

1.1 Background

In the past decade, significant research has been conducted to analyze and improve the impact behavior and puncture resistance of railroad tank cars. Ultimately, the results of this research will be used by the Government regulatory agencies (i.e., the Federal Railroad Administration [FRA] and Transport Canada [TC]) to establish performance-based testing requirements and to develop methods to evaluate the crashworthiness and structural integrity of different tank car designs when subjected to a standardized shell impact scenario. A performance-based requirement for tank car head impact protection has already been defined within the current regulations (Pipeline and Hazardous Materials Safety Administration, DOT, 2015).

FRA has a continuing research program to provide the technical basis for rulemaking on enhanced and alternative performance standards for tank cars and review of new and innovative designs that are developed by the industry and other countries. In support of this ongoing research program, full-scale tests are necessary to provide the technical information to validate modeling efforts and to inform regulatory activities. These tests evaluate the crashworthiness performance of tank cars used in the transportation of hazardous materials including designs that comply with current regulations as well as innovative new designs that have improved puncture resistance. FRA is currently working closely with key industry stakeholders to use the information being generated from these programs to revise and refine the construction, design, and use of tank cars.

This report documents the analyses and test results for a side impact test performed on a DOT-111 tank car that meets voluntary industry standard CPC-1232 (Dorsey, K. B., 2011). Previously tested tank cars in this research program have all featured an exterior jacket; however, the DOT-111 tank car used in this test was unjacketed. The exposed tank shell made it possible to directly observe the tear propagate on the exterior of the tank shell for the first time in this testing program. This report documents the impact test and describes the finite element (FE) model development and pre-test estimates, the comparisons of the test and analyses, and the subsequent post-test analyses performed to address the variations between the pre-test analyses and actual test conditions.

1.2 Objectives

The objective of the test was to quantify the deformation mode, impact load-time history, and puncture resistance of a tank car in a side impact. Moreover, the impact conditions were developed so that the side impact test was: 1) safe, 2) repeatable, and 3) analyzable. The test conditions were similar to the impact tests previously performed on a DOT-111 (Kirkpatrick, S. W., Rakoczy, P., & MacNeill, R. A., 2015), a DOT-112 (Rakoczy, P., & Carolan, M, 2016), and a DOT 117 tank car (Rakoczy, P., Carolan, M., Gorhum, T., & Eshraghi, S., 2019) with the exception that this tank car does not have an exterior jacket or insulation.

The objective of the analyses was to provide estimates of the tank car impact response both for pre-test planning and for the validation of tank car impact and puncture modeling capabilities.

1.3 Scope

This report includes a discussion of developing and executing the FE models used in this program, including modeling the tank car steel, modeling the water within the tank, and modeling the gas phase outage within the tank. This report presents the test results, discusses the execution of the test, and summarizes the overall results of the test. A discussion of the post-test modeling adjustments is also included in this report. Finally, this report presents a comparison between the test measurements and the model results.

This report does not include any results from further analyses using the DOT-111 tank car model, such as impact conditions outside of the conditions of the test. While this report refers to previously performed shell impact tests on tank cars of different specifications (Kirkpatrick, S. W., Rakoczy, P., & MacNeill, R. A., 2015) (Rakoczy, P., & Carolan, M, 2016) (Rakoczy, P., Carolan, M., Gorhum, T., & Eshraghi, S., 2019) (Carolan, M., & Rakoczy, P., 2019) (Kirkpatrick, S. W, 2010), no comparison of results from different tests are included within the scope of this report. Research into the puncture resistance of tank cars is ongoing, and such further simulations or comparisons may be considered in future work.

1.4 Overall Approach

Because of the difficult-to-control variables of testing, such as wind speed, unknown weld qualities, and the inherent variability of material behavior even within a single plate, there is no such thing as a certain test outcome. It is useful to frame the discussion of test planning in terms of likelihood of puncture versus impact speed, as Figure 1 shows. In an ideal test, the target test speed would be chosen to fall somewhere in the shaded range in Figure 1, where puncture is possible, but not certain.
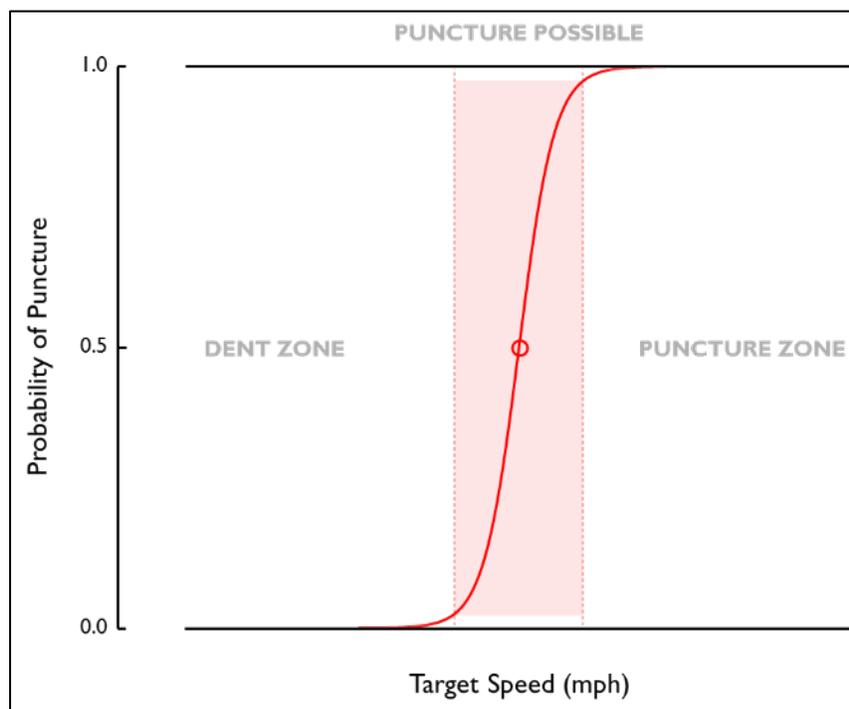
Figure 1. Schematic Illustrating Probability of Puncture vs. Impact Speed

The value of a test can be increased by targeting an impact speed that is very close to the threshold speed between where the tank car punctures and where it does not puncture for a given impactor shape, size, and mass. If the tested impact speed is close to this threshold speed, regardless of whether or not the tank punctures, the data that is collected can be extremely valuable both for model validation and for estimating the threshold puncture speed under the given impact conditions. From the standpoint of test execution, the ideal range of test speeds provides a practical target to maximize the value of the test. One target for maximizing the value of the test data would be to run a test in which the impactor is brought to a complete stop at the instant the tank punctures. Such a test would be an experimental demonstration of the threshold puncture speed, as all of the ram car's initial kinetic energy has been transferred into the tank car at the same instant that the tank car reaches the limit of its capacity. An incrementally slower test would have been a non-puncture test, and an incrementally faster test would have exceeded the capacity of the tank car to resist puncturing.

In the same spirit, making a blanket statement as to the superiority of a puncture test or a non-puncture test does not provide for a useful discussion without considering proximity to the theoretical threshold puncture speed. As the test speed moves further from the center of the puncture threshold range, the value of the test data decreases. Neither a test that causes catastrophic damage to the tank car structure nor a test that scarcely creates a dent would be an effective tool for evaluating the puncture resistance of the car. These tests also would not provide much utility for model validation, evaluating the relative impact resistance offered by different tank car designs, or for evaluating new or novel methods of simulating impacts. The extremely unlikely-to-puncture case would not provide enough information to assess the model sufficiently to make a comparison, and the overwhelmingly likely-to-puncture case could result in a mode of tank failure that does not truly represent the way tank cars experience puncture near their puncture/non-puncture thresholds.

The highly nonlinear force response of an impacted tank car makes extrapolation or interpolation of test results to attempt to calculate the threshold speed between puncture and non-puncture problematic. The uncertainty of an interpolation or extrapolation increases when the test speed is either significantly higher or significantly lower than the threshold speed. Thus, if test results are obtained at speeds far away from the theoretical threshold puncture speed, the threshold puncture speed will not be known with a high degree of certainty.

A test that punctures the tank, but does not leave the impactor with an excessive amount of residual kinetic energy can be used to verify that a model captures both the overall response of the tank car and the suitability of the puncture modeling techniques defined for the materials of the car. However, achieving this outcome can be challenging. The threshold puncture speed is typically estimated from pre-test models. If the pre-test model predicts a higher threshold puncture speed than the tank car actually possesses, then a test that is planned to be performed at the threshold puncture speed may in fact be an excessively fast test. While the energy absorbed by the tank up to the point of puncture in the test can be used to estimate the energy necessary to cause puncture, this estimate becomes less reliable as the actual impact speed gets further from the threshold puncture speed. At the same time, if the pre-test model is overly conservative, then a test that is planned for just below the threshold puncture speed, may in fact result in an impact speed that is well below the threshold puncture speed.

Figure 2 presents a flowchart with the overall approach of testing and analyses followed in this program. This flowchart presents a schematic view of the approach followed by Volpe National

Transportation Systems Center (Volpe) in its model development and by Transportation Technology Center, Inc. (TTCI) in developing and executing the test. Figure 2 illustrates the collaboration between Volpe and TTCI throughout the testing and modeling process, all of which was coordinated with FRA. For example, the instrumentation placement described in the testing plan could be used to guide requests for corresponding results in the FE model. The model results could then be used to estimate the magnitude of the response (e.g., pressure or displacement) that the instrumentation would experience at that location. If necessary, the instrumentation in the test plan could be updated to account for the expected response from the model.
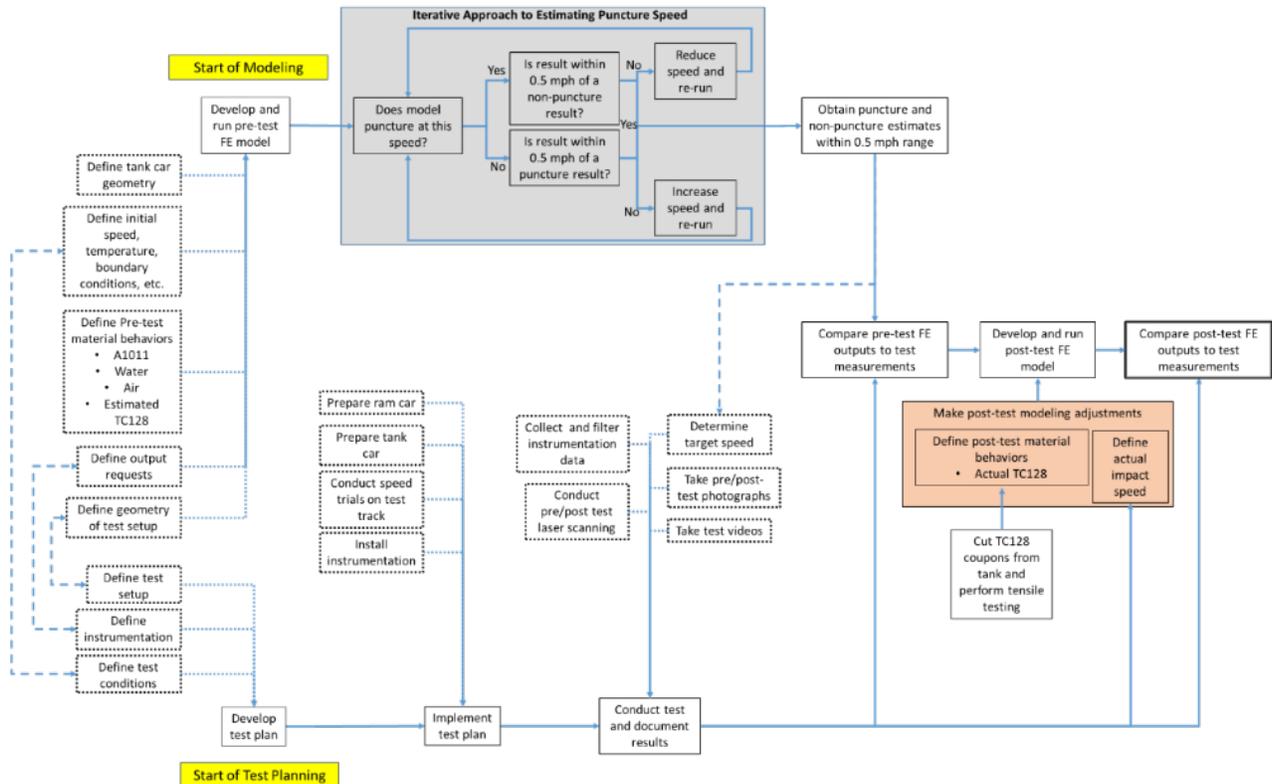
Figure 2. Flowchart Summarizing Overall Modeling and Testing Approach

Volpe, TTCI, and FRA collaborated before the test to determine the target test speed based on the model estimates, the desired outcome of the test, and such factors as ambient conditions (e.g., wind speed influencing actual impact speed) at the time of the test. After the test, material coupon test data from the TC128 shell of the car and the measured test speed were used to update the pre-test model to reflect the actual test conditions. Finally, a comparison of the post-test model results and the test measurements took place .

1.5 Organization of the Report

Section 1 introduces the work performed for research project, including the objectives and scope.

Section 2 describes the tank car undergoing testing and analysis, and the shell impact test setup.

Section 3 describes the instrumentation used during the test and its placement, which includes a discussion of the cameras used to capture the impact event.

Section 4 presents the results of the test that include a description of the actual conditions of the impact, the test itself, and a summary of the measured test data.

Section 5 describes the development of the FE models used in this program, which includes the geometry used in the model, the different material models developed, and modeling techniques used in the pre-test and post-test models.

Section 6 presents test measurements alongside the corresponding estimates from the pre-test FE models.

Section 7 presents test measurements alongside the corresponding estimates from the post-test FE models.

Section 8 includes a summary of the research performed and concluding remarks.

Appendix A describes the positions of the cameras and targets used in the test.

Appendix B contains the full set of test data, and the material data measured during the tensile coupon tests for the TC128 steel making up the tank car's shell.

Appendix C contains a full set of comparisons between test measurements and FE estimates, including comparisons for pre-test models using two different material behaviors, and for the post-test model using the actual TC128 steel behavior.

Appendix D describes the geometry and mesh on each part used in the FE models.

Appendix E contains a description of the modeling techniques used in both the pre-test and post-test FE models.

Appendix F contains a description of the development of each material behavior in the FE models.

2. Test Conditions

2.1 Tank Car

The test was performed on a DOT-111 tank car that meets voluntary industry standard CPC-1232. It is a non-pressurized tank car used in North America to carry flammable liquids, such as crude oil and ethanol.[1] The tank is built from two cylinders slightly inclined toward the bottom and seamed at the center. The 0.5-inch-thick tank car shell is constructed with TC-128 Grade B steel (TC128) and has an inside diameter of 122.5 inches. The 0.5-inch-thick head shields are constructed with the American Society of Testing and Materials (ASTM) A572 Grade 50 steel. The pressure relief valve (PRV) installed on this car has a start-to-discharge pressure of 75 psi. Figure 3 shows drawings for the general arrangement of an example DOT-111 tank car (not CPC-1232 compliant) (Elkins, A, 2017).
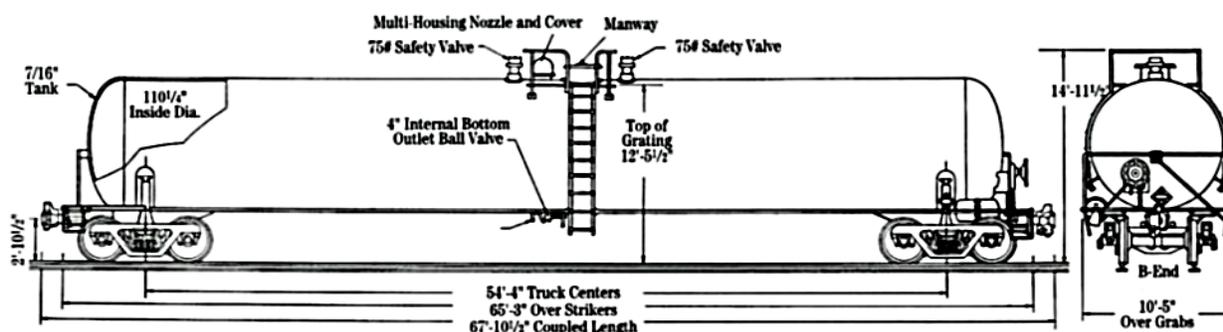
Figure 3. Example DOT-111 Tank Car Design Specification

The capacity of the tank car was reported in two sources as slightly different values. The builder's specification listed its full water capacity as 31,808 gallons. The tank car itself had a stenciled capacity of 31,720 gallons. While these two values represent a small difference in tank capacity, a difference in tank capacity introduces uncertainty into determining the actual outage volume. In particular, when filling the car to achieve a small outage, the uncertainty in outage volume can be on the same order of magnitude as the desired outage itself. To obtain the outage for the test condition, researchers used the loading procedure described in Section 2.2.

Figure 4 shows the tank car used for this test. This tank car had been involved in a derailment which resulted in significant damage to the tank head at the A-end of the car. To ensure the integrity of the test, a visual inspection and a magnetic particle scan of the head were performed. The inspections found no indication of cracks in the metal. In addition to the damage to the head, a small rectangular section had been cut out of the tank wall about halfway between the A-end of the car and the manway. This damage was repaired on-site, at the Transportation Technology Center (TTC) near Pueblo, CO. An oversized rectangular piece of 0.5-inch TC-128 Grade B steel plate, which had been rolled to match the inside diameter of the tank car, was purchased. The hole in the tank car was opened (red arrow in Figure 4) to match the dimensions of the patch, and

---

[1] Non-jacketed DOT-111 tank cars meeting CPC-1232 are to be phased-out of flammable liquid service in the United States according to schedules published under 49 CFR Part 173, Subpart F. Non-jacketed CPC-1232 cars in flammable liquid service in Canada are subject to a separate phase-out schedule published in Protective Direction No. 39.

then the edges of the patch and the hole in the tank car were beveled to ensure complete weld penetration. The patch was welded in, and then the area around the weld was heat treated.
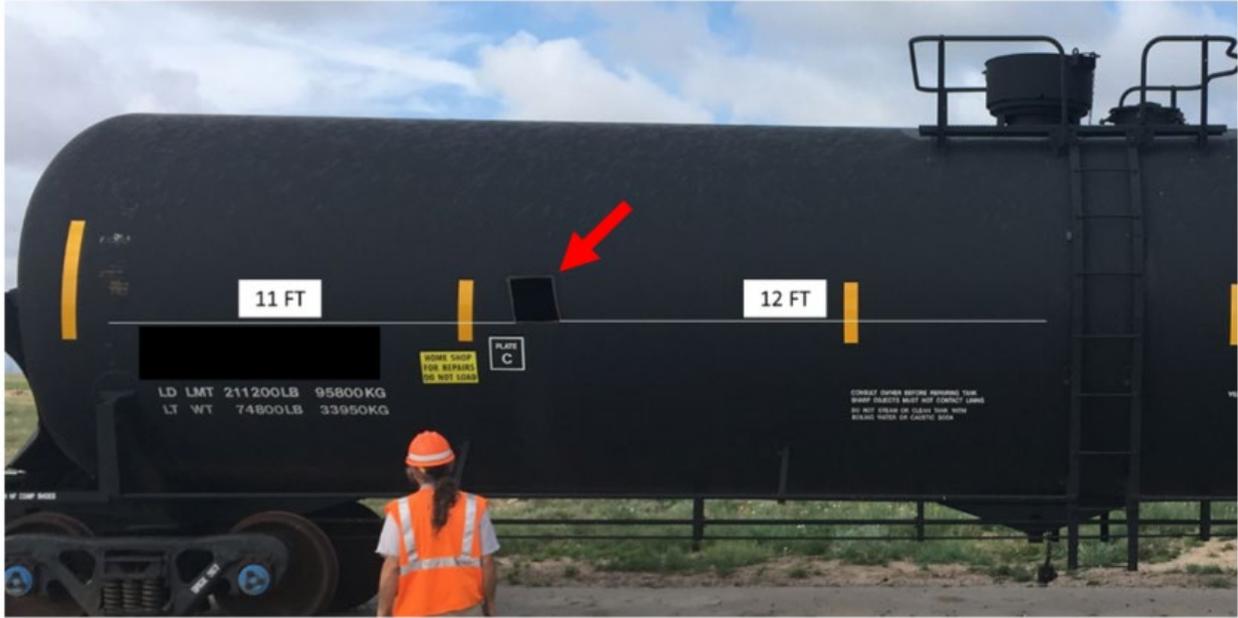
Figure 4. Location of Cutout in Tank Shell (see red arrow)

2.2 Test Setup

FRA performed the side impact test on October 30, 2018, at the TTC in Pueblo. The test was performed by sending a ram car into the side of the tank car, which was mounted on skids and backed by a rigid impact barrier, as Figure 5 shows. Note the damaged A-end head of the car can be seen on the left side of this figure, and the repaired patch of shell is approximately midway between the head and the painted grid.

Figure 5. Target Tank Mounted on Support Skids

Figure 6(a) shows one of the skids that the tank car was placed on, oriented parallel to the track with one end near the impact barrier. Four sections of I-beams were welded to the tank car and skids for the attachment, as Figure 6(b) shows. The tank car with skids attached was placed on 1-inch steel plates. This test configuration designed minimized the tank car rollback and allowed the tank car on the skids to slide on the steel plates during the impact.

| (a) Support skids | (b) Welded I-beam connection |

Figure 6. Tank Support Skid System

Figure 7 shows the DOT-111 tank car was equipped with a bottom valve protection structure. Because of low clearance at the center of the tank, the skid plates were placed on several plywood sheets. Additionally, the bottom outlet valve extension that projected past the bottom of the protective housing was removed before the test.

Figure 7. Tank Car's Bottom Valve Protection Structure

The tank car's ladders would have interfered with the impactor on one side and the impact wall on the other; therefore, they were also removed before the test.

The sloped geometry of this tank car kept empty volume at both ends of the shell even when filled full at the manway. These volumes (referred to as void space) were not accessible from the car's exterior when the car is filled and cannot be measured. Thus, the test team calculated the outage based on the amount of water required to fill the car at the manway. Water was added to the tank until the water level reached the bottom of the manway insert within the tank. Then 5 percent of the total volume that was required to fill the tank car to this level was pumped back out to achieve the desired 95 percent fill level. The manway lid was sealed, but no additional pressure was introduced to the tank car. The lading pressure and volume were like a loaded flammable liquid tank car in service conditions.

The indenter was positioned to align with the mid height of the target tank car as closely as possible. The ram car was a modified flat car with an 8-foot indenter installed on the leading end. This ram car was used in previous tank car tests and has a shortened tank attached to the ram end. Figure 8 shows the ram car. For this test, a 12-inch by 12-inch indenter with 1.0-inch radii on the edges and corners was used. The same indenter was used in the impact test of a DOT-111 tank car (Kirkpatrick, S. W., Rakoczy, P., & MacNeill, R. A., 2015), a DOT-112 tank car (Rakoczy, P., & Carolan, M, 2016), a DOT-117 tank car (Rakoczy, P., Carolan, M., Gorhum, T., & Eshraghi, S., 2019), and a DOT-105 tank car (Carolan, M., & Rakoczy, P., 2019). This large indenter was expected to result in a considerable amount of fluid motion (i.e., "sloshing") during the test, and it required careful modeling of the lading to be able to capture this motion. Figure 9 shows the 12-inch by 12-inch indenter attached to the ram car, and Figure 10 shows the ram car aligned with the tank car. The ram car was weighed before the test to confirm the actual weight. The measured weight was 297,150 pounds.

Figure 8. Ram Car and Head

Figure 9. Ram Arm with 12-inch by 12-inch Indenter

Figure 10. Ram Arm with 12-inch by 12-inch Indenter Aligned with Center of the Tank Car

3. Test Instrumentation

3.1 Overview

The test configuration and instrumentation were consistent with the specifications of the test implementation plan (Transportation Technology Center, Inc., 2016). Table 1 lists all instrumentation used for this test. Additional descriptions of the various types of instrumentation are provided in the following subsections.

Table 1. Instrumentation Summary

Type of Instrumentation	Channel Count
Accelerometers	11
Speed Sensors	2
Pressure Transducers	13
String Potentiometers	10
Total Data Channels	36
Digital Video	6 cameras (including 4 high-speed cameras)

3.2 Ram Car Accelerometers and Speed Sensors

The local acceleration coordinate systems were defined relative to the ram car. Positive x, y, and z directions are forward, left, and up relative to the lead end of the ram.

Three triaxial accelerometers were mounted on the longitudinal centerline of the ram car at the front, rear, and near the middle of the car. Two uniaxial accelerometers were mounted on the left and right sides of the ram car to supplement recording of longitudinal acceleration. Figure 11 illustrates the positions of these accelerometers. Table 2 provides a summary of the ram car accelerometer types and positions.
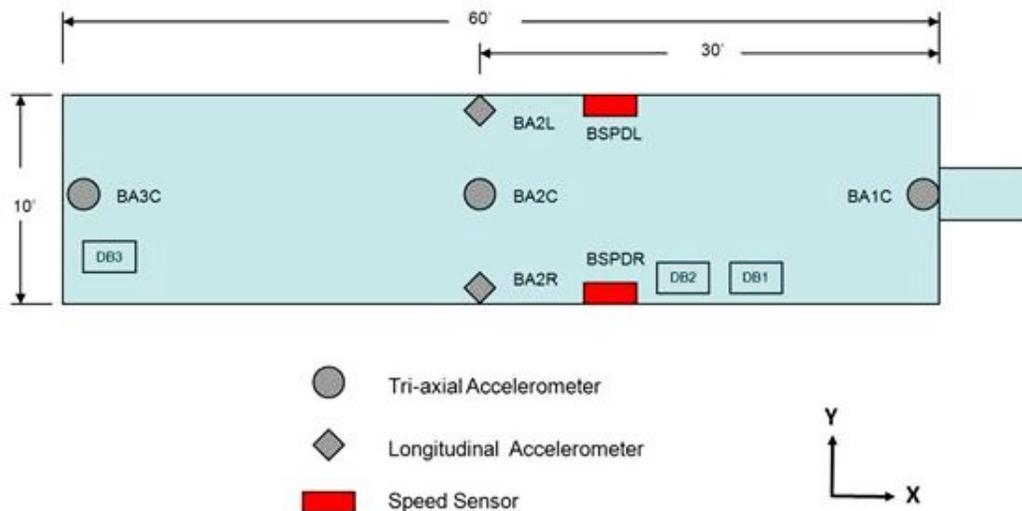
Figure 11. Ram Car Instrumentation

Table 2. Ram Car Accelerometers

Channel Name	Sensor Description	Range
BA1CX	Leading End, Centerline, X Accel	200 g
BA1CY	Leading End, Centerline, Y Accel	100 g
BA1CZ	Leading, Centerline, Z Accel	200 g
BA2LX	Middle, Left Side X Accel	100 g
BA2CX	Middle, Centerline, X Accel	50 g
BA2CY	Middle, Centerline, Y Accel	50 g
BA2CZ	Middle, Centerline, Z Accel	50 g
BA2RX	Middle, Right Side X Accel	100 g
BA3CX	Trailing End, Centerline, X Accel	200 g
BA3CY	Trailing End, Centerline, Y Accel	100 g
BA3CZ	Trailing End, Centerline, Z Accel	200 g

Speed sensors were mounted on both sides of the ram car to provide accurate measurement of the car's velocity within 20 inches of the impact point. The speed sensors were reflector-based light sensors, which use reflectors on the ground separated by a known distance in conjunction with light sensors mounted on the car. They were triggered as the ram car passed over the reflectors. The last reflector was positioned to align with the sensor when the indenter was within a few inches of the impact point. The time interval between passing the reflectors was recorded, and the speed was calculated from distance and time. A handheld radar gun was also used to take supplemental speed measurements.

3.3 Tank Car String Potentiometers and Pressure Transducers

The local displacement coordinate systems (except for the tank heads) were defined relative to the tank car. Positive x, y, and z directions were forward, right (away from the wall), and up relative to the A-end of the tank car. Tank head displacements were positive toward the impact wall.

Six string potentiometers were used to measure the tank crush displacements around the immediate impact zone during the test. Five measured the dent formation of the tank at the tank center and at locations 24 inches and 48 inches on both sides of the impact point. The sixth string potentiometer measured the vertical deformations of the tank at the center (aligned with the impact point). Four additional string potentiometers were used to measure the tank motions. These string potentiometers were attached to each of the tank skids and to the center of the tank heads at both ends of the tank car. Fixed anchor positions were established so that these measurements were limited to the longitudinal motions of the tank heads and skids. Table 3 lists

all string potentiometers inside and outside the tank car. Figure 12 and Figure 13 show their placement.

Table 3. Tank Car String Potentiometers

Area	Location	Axis	Channel Name	Range inches
Impact Area	B-end – 48-inch offset	Y	TD1Y	40
Impact Area	B-end – 24-inch offset	Y	TD2Y	50
Impact Area	Center	Y	TD3Y	50
Impact Area	Center	Z	TD3Z	40
Impact Area	A-end – 24-inch offset	Y	TD4Y	50
Impact Area	A-end – 48-inch offset	Y	TD5Y	40
Tank Head	A-end	Y	TDBend	50
Tank Head	B-end	Y	TDAend	50
Skid	A-end	Y	TDBskid	50
Skid	B-end	Y	TDAskid	50
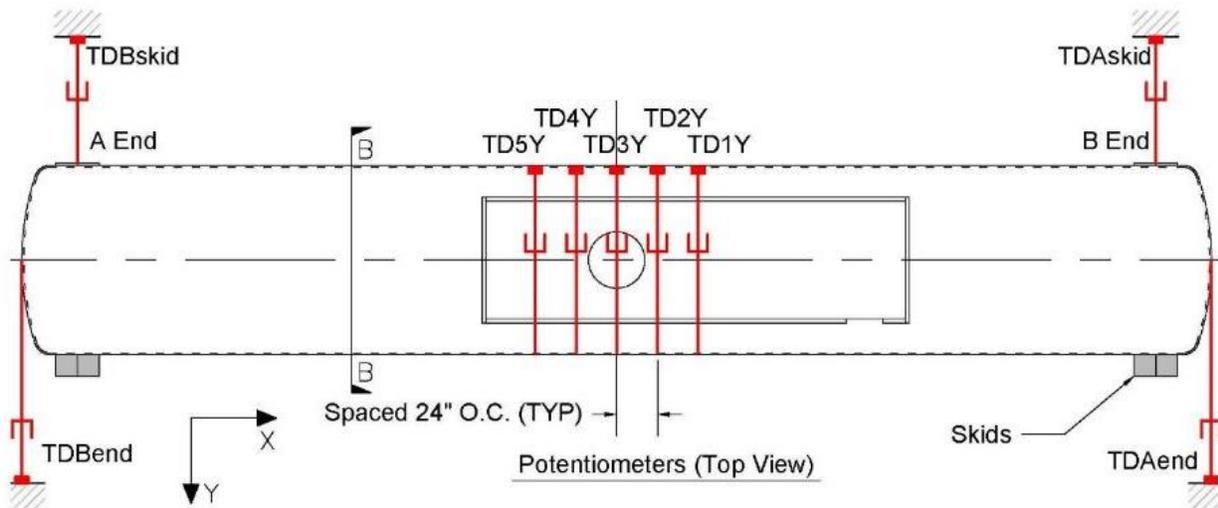
Figure 12. Tank Car String Potentiometers (top)
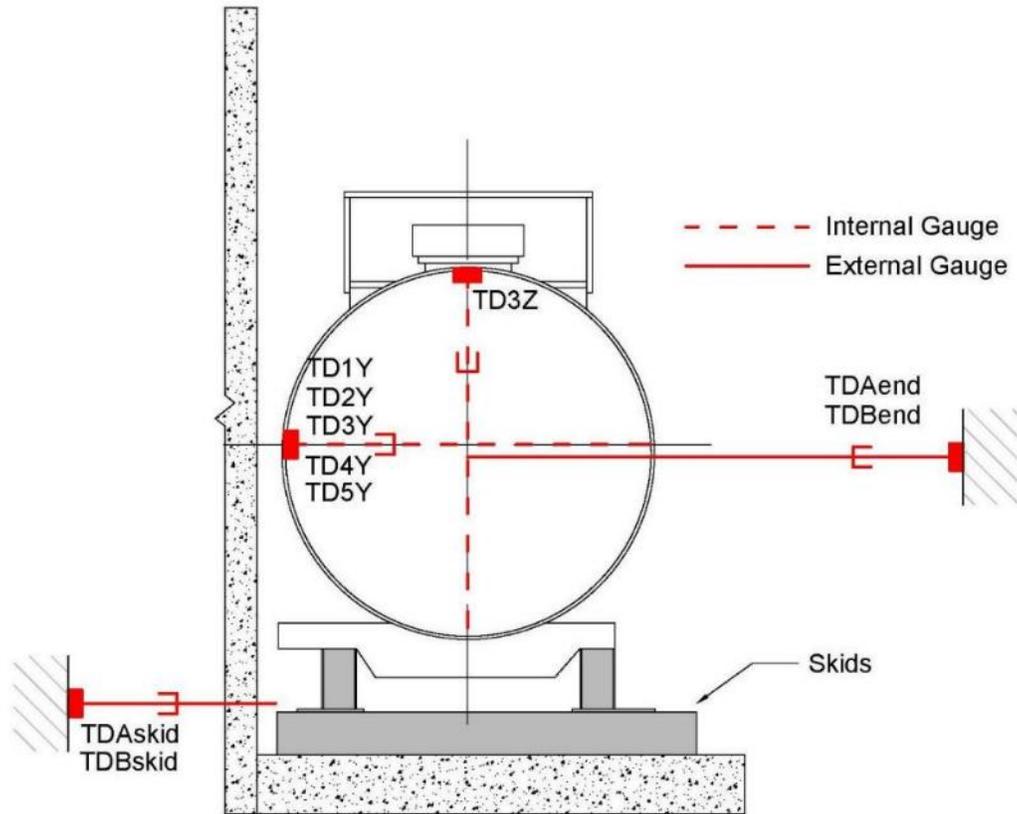
Section B-B (Typical Cross Section At Pressure Gauges)

Figure 13. Tank Car String Potentiometers (end)

An array of 13 pressure transducers was set up within the tank to record the pressure pulse through the lading. These pressure transducers were mounted in three sections on the top, sides, and bottom of the tank. Table 4 lists all pressure transducers used inside the tank car. Figure 14 and Figure 15 show their placement.

Table 4. Tank Car Pressure Transducers

Location	Channel Name	Sensor Description	Range psi
B Top	TP1000	B-end Top Pressure	300
B Back wall	TP1090	B-end Back Wall Pressure	300
B Front wall	TP1270	B-end Front Wall Pressure	300
B Floor	TP1180	B-end Floor Pressure	300
M Top	TP2000	Mid-length Top Pressure	300
M Back wall	TP2090	Mid-length Back Wall Pressure	300
M Front wall	TP2270	Mid-length Front Wall Pressure	300
M Floor	TP2180	Mid-length Floor Pressure	300
C Back wall	TP3090	Center Back Wall Pressure	300
C Floor	TP3180	Center Floor Pressure	300
C Front wall	TP3270	Center Front Wall Pressure	300
Manhole Lid	TPMH	Outage Pressure in the Manway	500
PR Valve	TPRV	Pressure Relief Valve	500
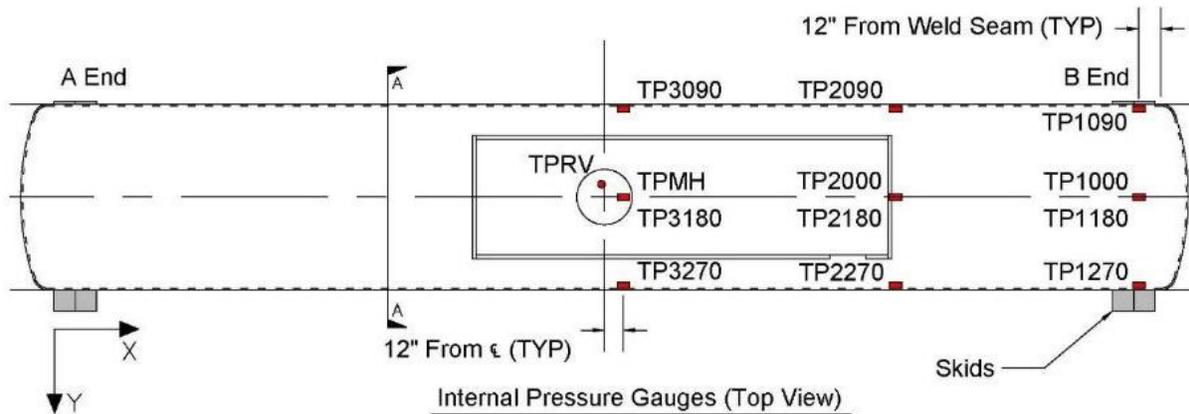
Figure 14. Tank Car Pressure Transducers (top)
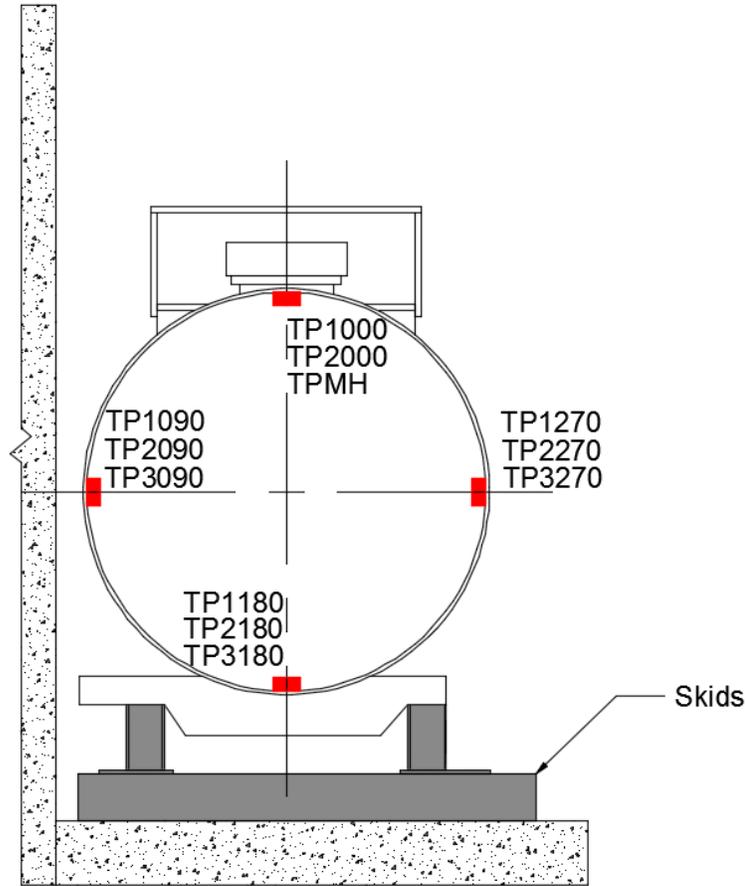
Section A-A (Typical Cross Section At Pressure Gauges)

Figure 15. Tank Car Pressure Transducers (end)

3.4 Real Time and High-Speed Photography

Four high-speed (HS) and two real time high definition (HD) video cameras were used to document the impact event. All HS cameras used were crashworthy and rated for peak accelerations of 100 g. The ram car and the impact barrier were painted with flat light gray paint. The tip of the indenter was painted red. High contrast targets were applied to the ram car and the indenter Appendix A contains a schematic of the locations of the cameras and positions of the targets.

3.5 Data Acquisition

A set of 8-channel, battery-powered, onboard data acquisition systems was used to record the data from the instrumentation mounted on the ram car. These systems provided excitation to the instrumentation, analog anti-aliasing filtering of the signals, analog-to-digital conversion, and recording of each data stream. A similar set of ground-based data acquisition systems was used to record data from the pressure transducers on the tank car.

The data acquisition systems were GMH Engineering Data BRICK Model III units. Data acquisition complied with the appropriate sections of SAE J211 (SAE International, 2007). Data from each channel were anti-alias filtered at 1,735 Hz, then sampled and recorded at 12,800 Hz.

Data recorded on the data bricks were synchronized to time zero at initial impact. The time reference came from closure of the tape switches on the front of the test vehicle. Each data brick was ruggedized for shock loading up to at least 100 g. Onboard battery power was provided by GMH Engineering 1.7 Amp-hour 14.4 Volt NiCad Packs. Tape Switches, Inc., model 1201-131-A tape switches provided event initial contact.

Software in the data bricks was used to determine zero levels and calibration factors rather than relying on set gains and expecting no zero drift. The data bricks were set to record 1 second of data before initial impact and 4 seconds of data after initial impact.

4. Results

4.1 Test Conditions

As described in Sections 2.1 and 2.2, this was a side impact test on an unjacketed DOT type 111A100W1 tank car, performed on October 30, 2018. The test involved a 13.9 mph side impact by a structurally rigid 297,150-pound ram car with a 12-inch-square indenter into the side of the tank car. The tank car was backed by a rigid impact barrier. The test tank car was filled to approximately 95 percent capacity with water to simulate standard commodity lading volume of a DOT-111 tank car, and it was sealed but not pressurized above atmospheric pressure.

At the time of the test, the ambient conditions included a wind speed of 4 mph out of the N-NE and an air temperature of 47 °F.

4.2 Details of Test

Pre-test simulations estimated a puncture speed range of 11 to 15 mph, based on estimated material properties. The target speed for the test was 13.5, ±0.5 mph, near the center of this speed range. Regardless of whether the tank punctured or remained intact, one objective in choosing this target test speed was to ensure the actual impact speed was close to the threshold puncture/non-puncture speed. Section 6 discusses of the pre-test simulations used to help select the target test speed. The actual calculated impact speed from the speed sensors was 13.9 mph.

The indenter punctured the tank car under a corner on the right-hand side of the indenter. The initial puncture created a tear about 8 feet high in the wall of the tank car. The ram car was brought to a stop and rebounded from the tank car following impact. Figure 16 shows the impact area after the test. The repair welded area of the tank is visible on the left side of this photograph. The presence of the repair weld did not affect the puncture, and the repair-welded area did not appear to experience any failure or tearing.

Figure 16. Tank Car after the Impact (impact side)

After the impact, the ram car rebounded and stopped due to the activated airbrake. The tank car also rebounded after striking the impact wall. Figure 17 shows the post-test position of the tank car relative to the supporting wall.

Figure 17. Post-Test Position of Tank Car (wall side)

4.3   Observations from Test Videos

Review of the test videos provided several insights into behaviors of the tank car during the impact test. This section discusses these test video observations

4.3.1   Puncture Initiation and Propagation

During the test, a video camera onboard the ram car captured several frames showing the puncture initiate and propagate. Since this was an unjacketed tank car, the tank car's shell was clearly visible during the impact. The puncture initiated near the upper-right corner of the impactor, as seen in Figure 18. This frame is the first video frame in which water was observed escaping from the tank, indicating the tear had extended through the full thickness of the shell. Review of 60 frame-per-second (FPS) video from the onboard ram car indicated that 22 frames had elapsed between the approximate time of first contact by the ram car until the frame extracted below. Thus, this frame demonstrates that the shell had torn through its thickness by approximately 370 milliseconds (ms) after impact. Note that because this camera was mounted above the impactor, any fracture initiation and propagation that occurred below the impactor was not captured by this view.

Figure 18. Frame Extracted from Onboard Ram Car Video (t~370 ms) Showing Water Escaping Tank Under Corner of Impactor

A subsequent frame extracted from the video camera onboard the ram car (Figure 19) shows the crack had begun to propagate from the top-right corner. The crack was propagating inboard (toward the centerline of the car) and upward. A larger quantity of water is visible in this frame compared to the last extracted frame, as the now-pressurized tank shell propels water through the growing tear in the tank's shell.
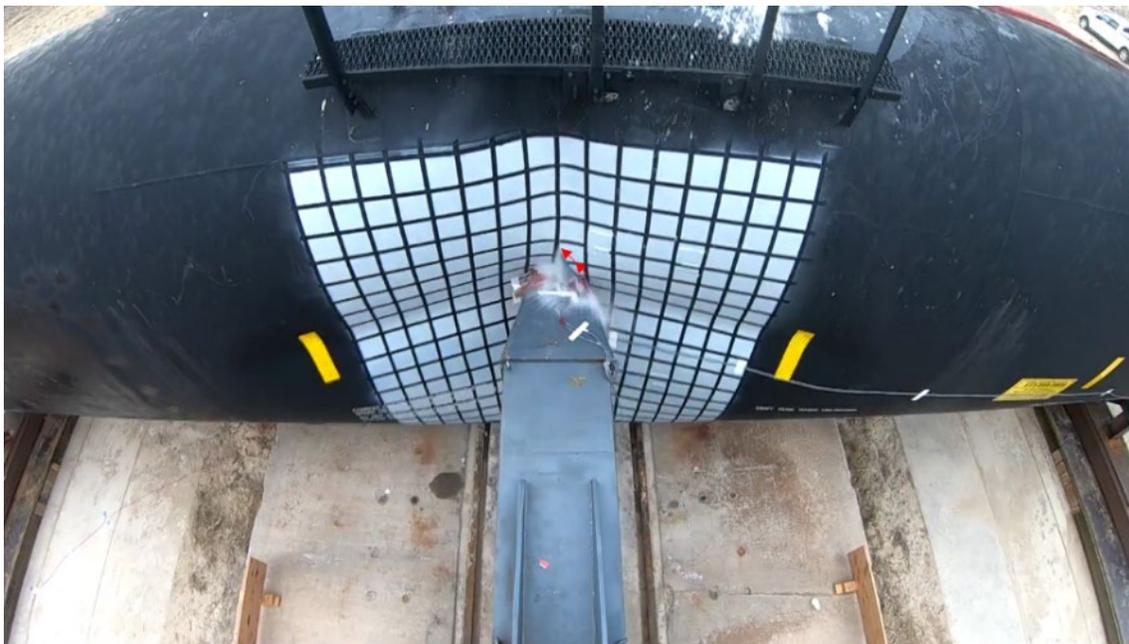
Figure 19. Subsequent Frame Extracted from Onboard Ram Car Video Showing Direction of Tear Propagation

A third frame was extracted from the onboard video and is shown in Figure 20. This frame shows the crack at the limit of its propagation. The crack propagation direction had turned nearly straight up, in the circumferential direction of the tank. For the DOT-111 tank used in this test, there is a circumferential weld between two rings used to form the tank's shell at the center of the impact location.

Figure 20. Third Frame Extracted from Onboard Ram Car Video Showing Direction of Tear Propagation at Extent of Tearing

Taken together, these video frames indicate that the puncture initiated in the base material of the tank car shell beneath the corner of the impactor, approximately 6 inches from the center weld. The presence of the weld did not appear to influence the initial puncture of the tank beneath the corner of the impactor. However, the presence of the weld did influence the propagation behavior of the crack once it had already formed.

4.3.2 Leakage Around Top Fittings

Examination of the HS video showing the top fittings of the tank car revealed water leakage from three different locations at three different periods between impact and puncture. Beginning at approximately 160 ms, water visibly escaped from the gasket to the manway cover plate through which the valves are attached to the car. This leakage was observable until the cover plate begins to move out of the overhead camera's view starting at approximately 210 ms. Figure 21 shows two frames captured from the overhead HS camera where a barely visible spray of water is observed at 160 ms (left) and water leakage is clearly seen at 170 ms (right).
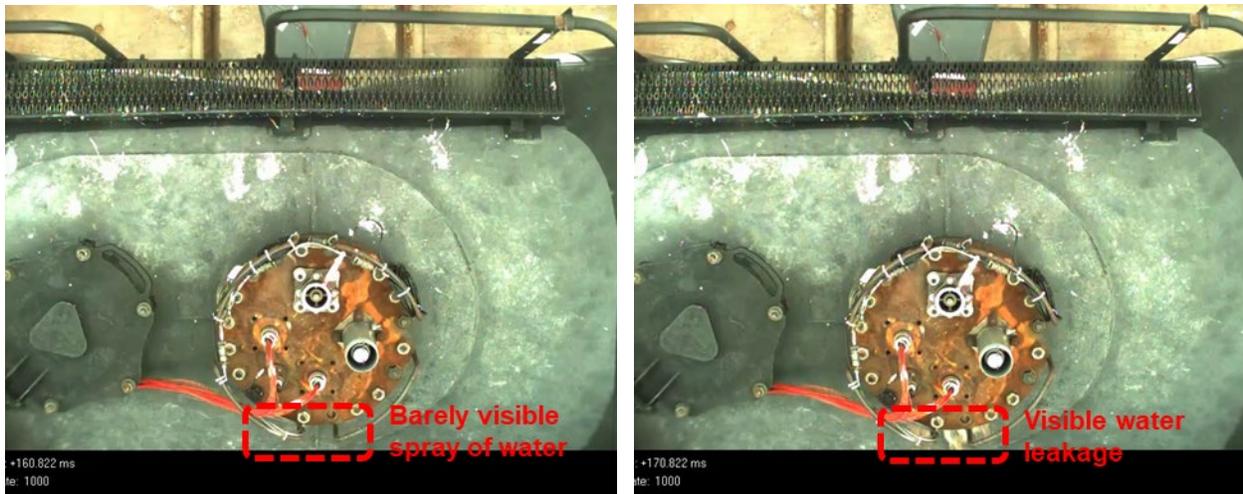
**Figure 21. Two Frames Captured from the Overhead HS Camera
at 160 ms (left) and 170 ms (right)**

Starting at approximately 180 ms, water was also observed to be escaping through the bolted manway. This manway leakage could be observed through the time of tank puncture at approximately 360 to 370 ms. Figure 22 shows a frame extracted from the HS video at approximately 180 ms on the left, and a frame taken at approximately 370 ms on the right. The frame on the right is also annotated to show the visible water leakage from the puncture under the corner of the impactor as previously described in Section 4.3.1.
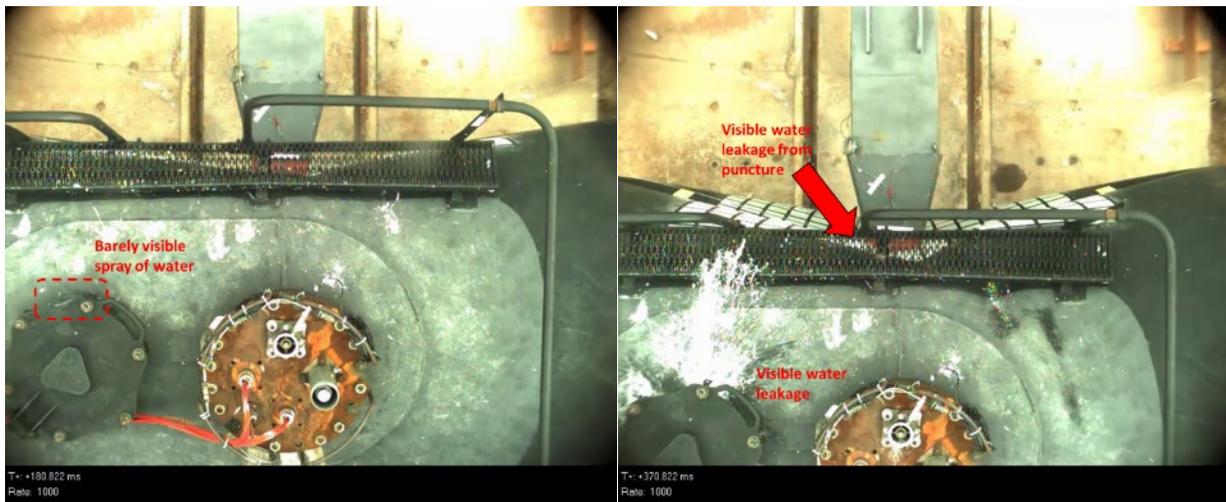
**Figure 22. Two Frames Captured from Overhead HS Camera
at 180 ms (left) and 370 ms (right) Showing Leakage from Bolted Manway**

Beginning at approximately 310 ms, water was observed to be venting through the PRV at the top of the tank. This PRV venting continued through the time of tank puncture at approximately 360 to 370 ms. Figure 23 shows a frame extracted from the HS video at approximately 310 ms on the left and a frame extracted at approximately 370 ms on the right.

**Figure 23. Two Frames Captured from Overhead HS Camera
at 310 ms (left) and 370 ms (right) Showing Water Venting through PRV**

4.4 Laser Scanning

TTCI laser-scanned a surface of the tank car in the impact zone measuring approximately 8-foot by 8-foot. Scans were performed before and after the impact test. Figure 24 shows a composite image where the geometry from the scan was overlaid on a photograph of the punctured tank car to show the extents of the scan geometry. Figure 25 shows two exterior views of the deformed shape surface from the post-test geometry scan.
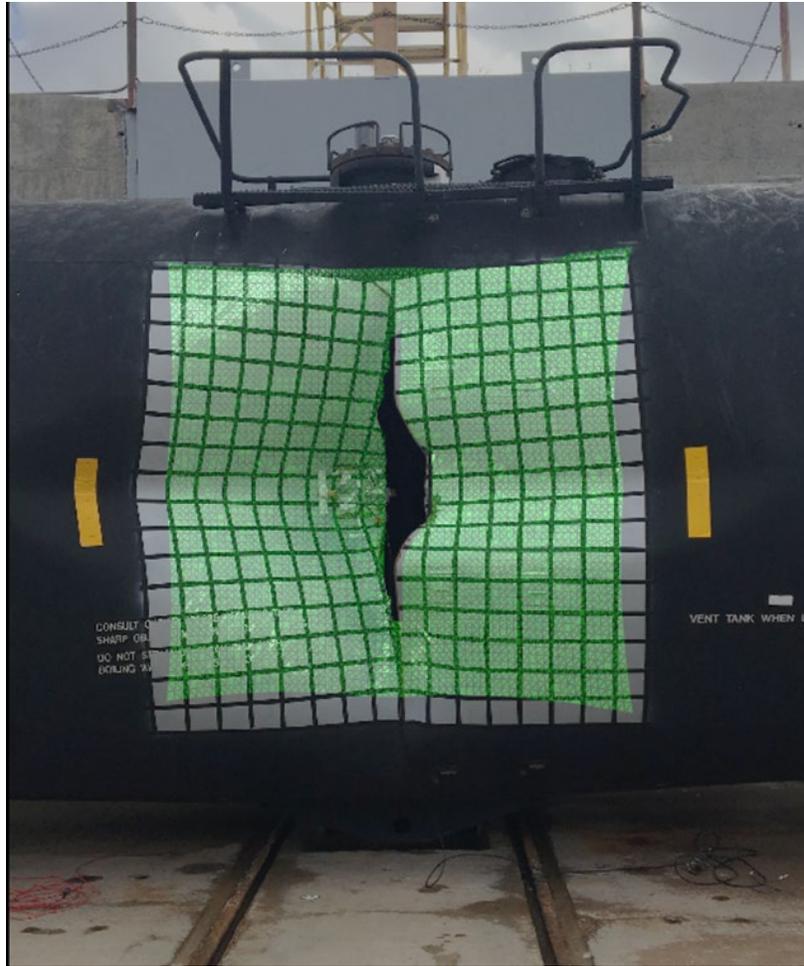
Figure 24. **Composite Image of Scan Geometry Overlaid on Photograph of Post-test Tank Car**
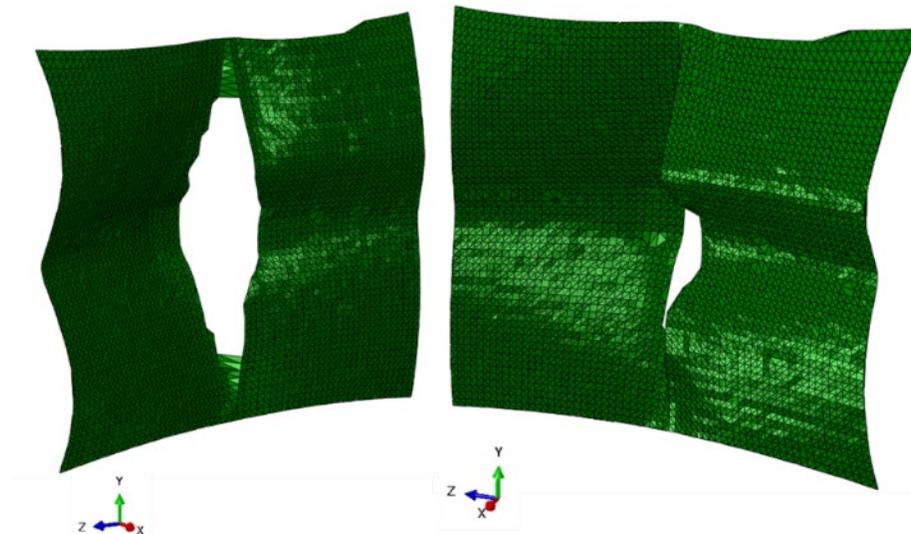
Figure 25. Two Views of Deformed Shape Surface from Post-test Scan

Figure 26 shows a comparison of the cross-sections of the impact location from the pre- and post-test scans aligned using reference points located on the tank car. The image on the left corresponds to the section of the tank that was on the left side of the impact area, and the image on the right corresponds to the section of the tank that was to the right of the impact.
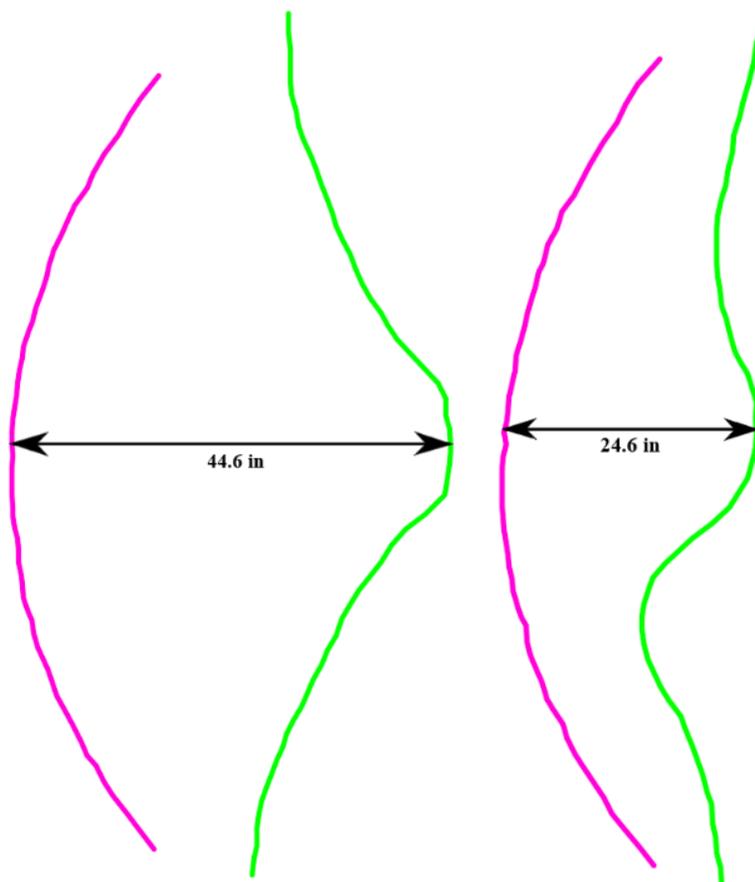
Figure 26. Comparison of Pre-test and Post-test Surface Scans—Cross-section at the Impact

It is clear from the figure that the deformation of the shell is much larger to the left of the point of impact. This is also apparent in the post impact picture of the tank car (Figure 16) above. The reason for this difference was the way in which the tank tore during impact. The section of the tank under the right edge of the impactor sheared, allowing the impactor to slide by. The left side, which was still in contact with the impactor, remained intact, resulting in that side undergoing more deformation. The maximum permanent (plastic) deformation on the impact surface was approximately 44.6 inches.

To determine the relative indentation of each point in the scanned point cloud, it was first necessary to calculate the original coordinates of each point on the undeformed tank surface. Since the tank was originally a cylinder of known radius, the Y (vertical) and Z (axial) coordinates of each point in the deformed point cloud could be used to calculate the X (horizontal) coordinate of the corresponding point on the outer surface of the cylinder. Using the maximum dent depth of 44.6 inches (shown in Figure 26), the deformed scan could be positioned relative to its undeformed position. For each point in the deformed point cloud, the difference

between the X-coordinate in the deformed point cloud and the calculated X-coordinate on the surface of the undeformed tank equals the depth of the dent at that point. These dent depths were then overlaid onto the scan geometry using the Abaqus/CAE preprocessor to import the dent depth values as an analytical field.[2] Figure 27 shows two views of the deformed tank scan with overlaid contours of residual dent depth.
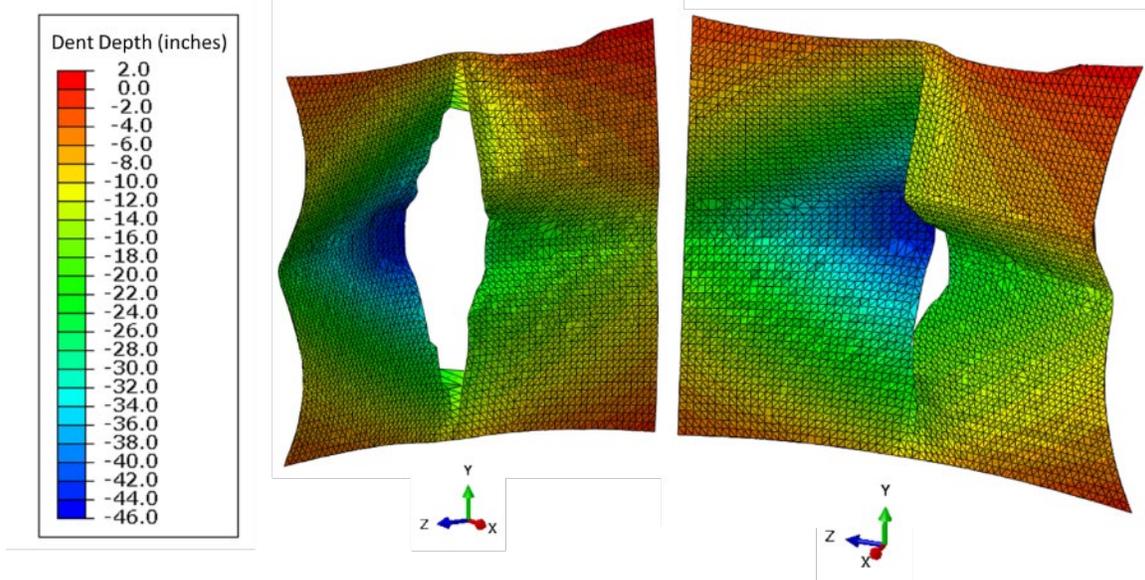
Figure 27. Two Views of Deformed Shape Surface from Post-test Scan with Overlaid Contours of Residual Dent Depth

4.5   Measured Data

The data collected in the test was processed (e.g., offset corrections, filtering, etc.) initially by TTCI and provided to Volpe for comparison to the analyses. The offset adjustment procedure ensured that the plotted and analyzed data contained only impact-related accelerations and strains and excluded electronic offsets or steady biases in the data. The data collected before impact was averaged to determine the necessary offset. This offset was then subtracted from the entire data set for each channel. This post-test offset adjustment was independent of, and in addition to, the pre-test offset adjustment made by the data acquisition system.

The post-test filtering of the data was accomplished with a phaseless four-pole digital filter algorithm consistent with the requirements of SAE J211 (SAE International, 2007). A 60 Hz channel frequency class (CFC) filter was applied for the filtered acceleration data shown in this report. A brief summary of the measured data is provided in this section. Appendix B contains the plots of filtered data from all transducers.

The longitudinal acceleration of the ram car was one of the primary measurements in the test. Multiple accelerometers were used on the ram car to capture this data. The data was used to derive the impact energy, deceleration of the ram car, and contact forces between the indenter

---

[2] It was necessary to assign this analytical field to a meaningless temperature variable to allow Abaqus to calculate the initial dent depth distribution and produce contour plots.

and target tank car. Figure 28 shows the ram car average longitudinal acceleration history from all the ram accelerometers.
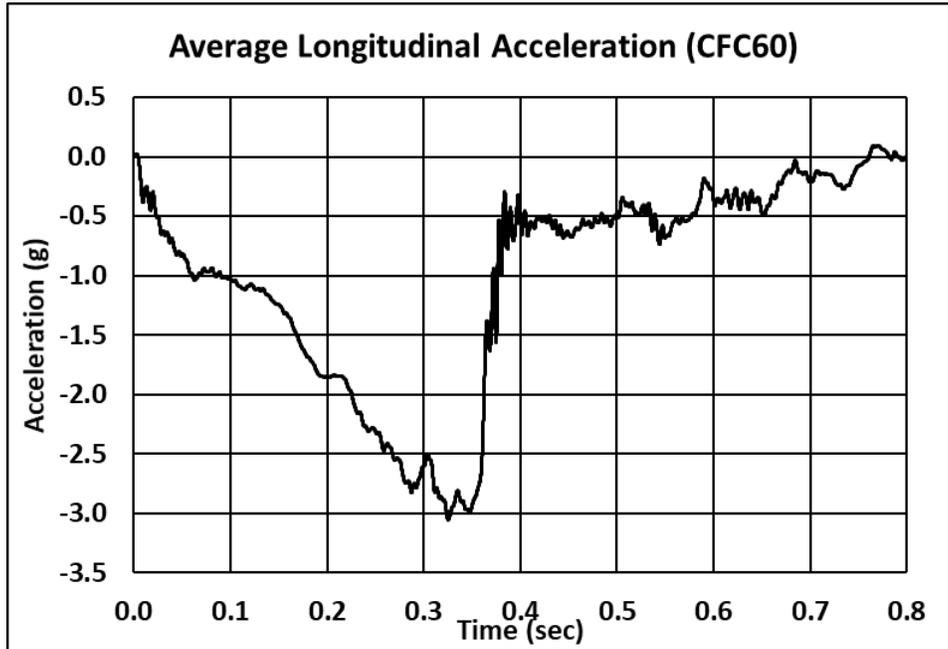
Figure 28. Longitudinal Acceleration Data (averaged)

The ram car velocity-time history in the test was calculated by integrating the average longitudinal acceleration of the ram car and using the impact speed measurement as an initial condition. Contact forces between the ram and target tank car were calculated as the product of the average acceleration and the mass of the ram car. Figure 29 shows both the force-time and velocity-time histories, where negative velocity is the speed of the rebounding ram car. This data shows that the ram car was traveling at less than 1 mph at the time of the force drop that corresponds to puncture.
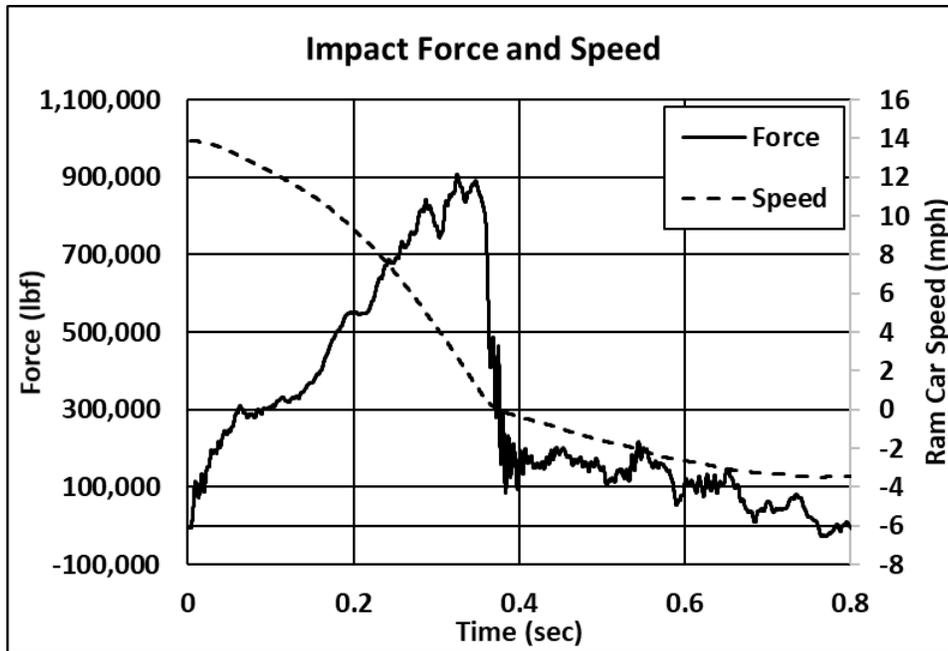
Figure 29. Impact Force and Ram Car Speed

Similarly, the kinetic energy of the ram car was calculated from its speed-time history and weight. Figure 30 shows the kinetic energy time history of the ram car and energy absorbed by the tank car. The energy absorbed by the tank car was capped at the time when the puncture occurred at approximately 0.36 second.
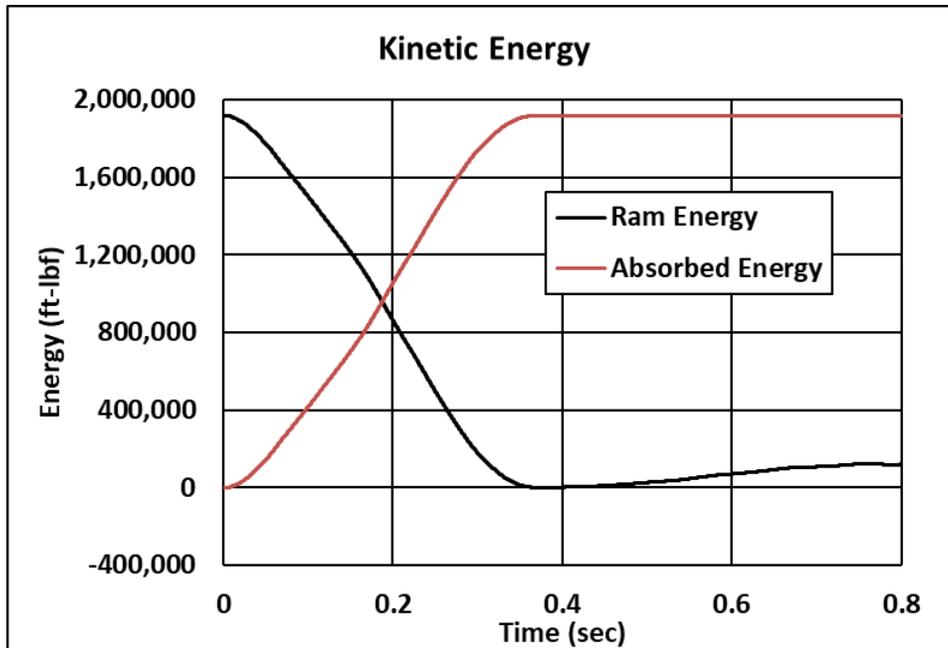
Figure 30. Kinetic Energy

The total kinetic energy of the ram car was approximately 1,917,000 ft.-lbf and the energy absorbed by the tank car before puncture 1,913,000 ft.-lbf. The difference between the initial kinetic energy and the energy absorbed by the tank before puncture was only 4,000 ft-lbf of excessive energy, or

30

slightly over 0.2 percent of the total kinetic energy. This difference is consistent with an impact in which the ram car is brought nearly to a stop at the time of tank car puncture.

Another significant impact response measured in the test was the effects of the internal pressure as the tank indentation formed and reduced the volume of the tank. The tank was filled to approximately a 5 percent outage volume with water, but the tank was not pressurized relative to atmospheric pressure. Water can be approximated as incompressible for the impact behavior. As a result, the small air volume in the outage, initially at one atmosphere, was compressed as the dent formation reduced the tank volume. This caused the internal pressure to rapidly increase. As described in Section 3.3, pressure transducers were mounted at several locations inside the tank car, both within the water and at the pressure release valve and manhole within the air.

As described in Section 4.3.2, videos taken during the test revealed that the cover plate, manway, and PRV all permitted water to leak from the tank at different periods during the test. While water venting through the PRV could be expected for an impact of sufficient severity to cause a pressure rise above the start-to-discharge pressure of the PRV, leakage through the cover plate and manway were unexpected. Regardless of the source of the water leakage, the effect on the tank car would be the same: a reduction in tank car stiffness compared to a perfectly sealed vessel. Since the car came to be imperfectly sealed during the test, the internal pressure had a means of escaping to atmosphere rather than building up inside the tank car.

Figure 31 shows pressure data from the center of the tank car (i.e., transducers TP3090 shown as Back Wall, TP3180 shown as Bottom, TP3270 shown as Front Wall, and TPMH shown as Outage). At about 0.18 second there was a sudden jump in the readings from several of the pressure transducers. Due to the tank's "ovalization" (i.e., increase in tank diameter at the top and bottom as a result of indentation on the side) upon impact, a gap formed between the back of the car and the support wall. By approximately 0.18 second, the car was pushed back and impacts against the support wall. While most of the pressure transducers recovered, TP3180 (center Bottom) and TP3270 (center Front Wall) appeared to have been permanently damaged by the shock of the impact. It is believed that the test car's lack of a jacket and insulation contributed to the severity of the response, because a jacket and insulation would have absorbed part of the energy of the collision and would have reduced the severity of the shock to the tank.

Prior to puncture, the overall pressure in the tank rose to about 80 psi. Additionally, the sloshing motions of the water in the tank created local pressure variations of up to 60 psi.
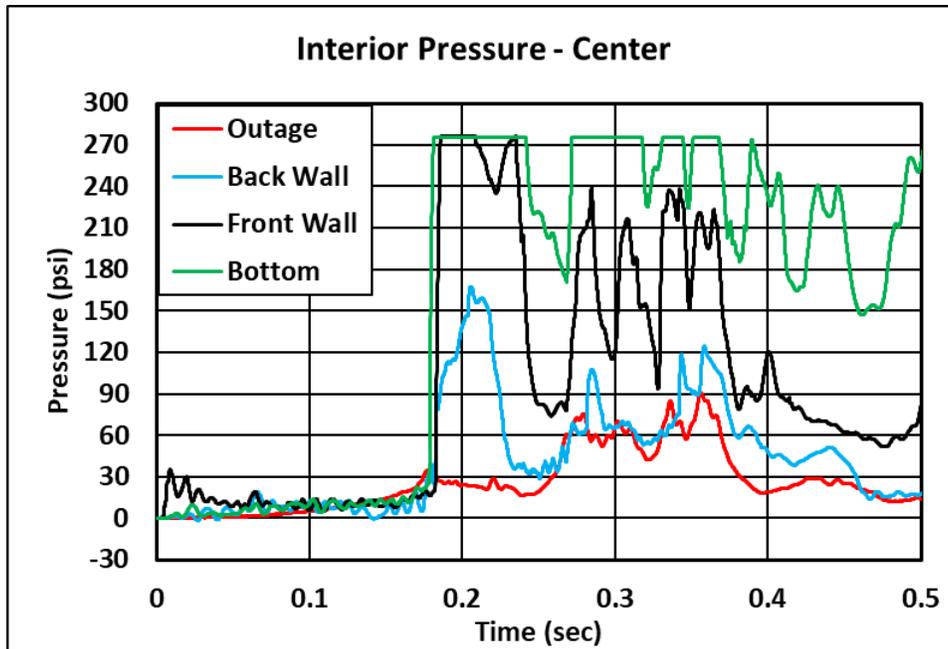
Figure 31. Pressure Data Measured at the Center of the Tank Car

The remaining quantitative measurements made of the tank impact behavior were displacement histories recorded with string potentiometers, which included both internal tank deformations and external tank movements at both ends of the tank. Section 3.3 describes the layout of the string potentiometers.

Figure 32 shows the measured displacements for the tank internal string potentiometers (DY1Y through TD5Y). Note that all but one of the string potentiometers reached the limit of their range before the longitudinal crush deformation reached its maximum. Larger-range string potentiometers were not available for this test. TD5Y (48 inches from center A-end) was the only string potentiometer to provide a complete record of the longitudinal crush displacements. TD3Y (Center) and TD4Y (24 inches from center A-end) appeared to have been damaged. The data from TD1Y (48 inches from center B-end) and TD5Y (inches from center A-end) indicated that tank deformation was greater on the side of the tear in the tank wall toward the B-end, which was also evident in the post impact photos of the tank car. Figure 33 shows the vertical tank deformation during impact recorded by TD3Z. There does not appear to have been any problems with this channel.
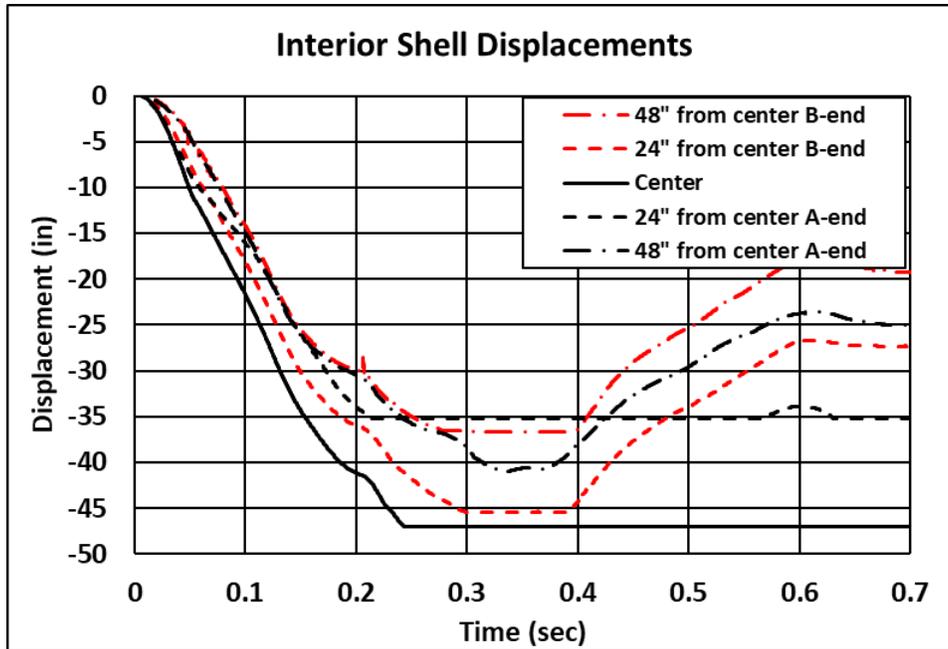
Figure 32. Internal Displacements
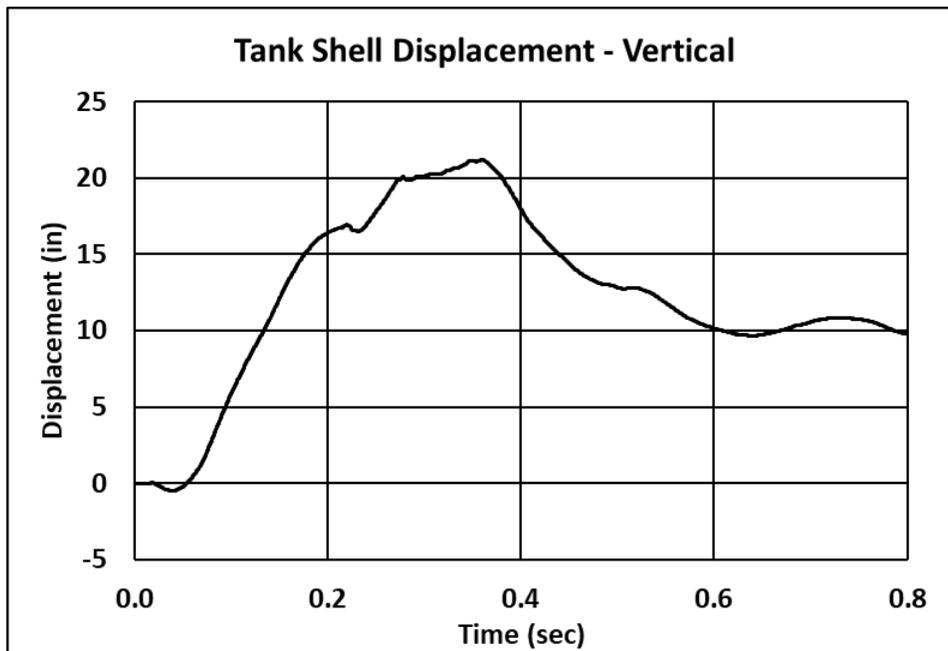
Figure 33. Internal Vertical Displacement

The measured displacements for the tank car external string potentiometers are shown in Figure 34 for the head-mounted string potentiometers and in Figure 35 for the skid-mounted string potentiometers. The displacements of the car ends were significantly delayed from the motions in the impact zone, and little displacement is seen for the first 0.1 second of the response. The measurements of the car end head displacements and the skid displacements were nearly

identical, and the response was symmetric between the A-end and B-end of the tank until rebound occurred approximately 0.4 second after the impact.

Figure 34. External Displacements – Tank Car Heads

Figure 35. External Displacements – Skids

5. FE Model Development

FE models of the DOT-111 tank car were developed prior to the test to help estimate the desired impact speed. These pre-test FE models provided estimates of the speed range where puncture could be expected to occur, while considering unknown parameters, such as the exact material behavio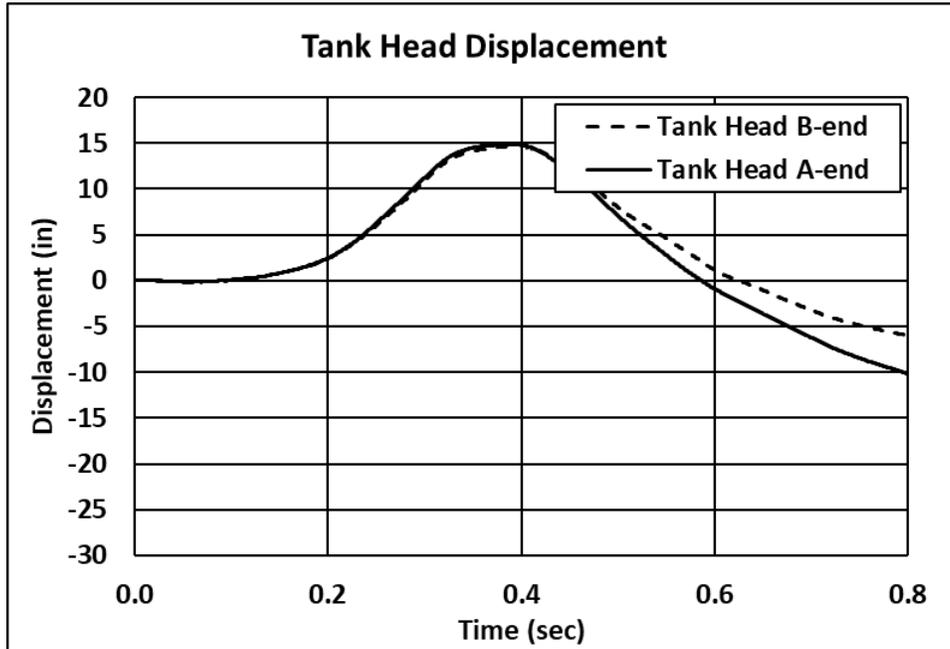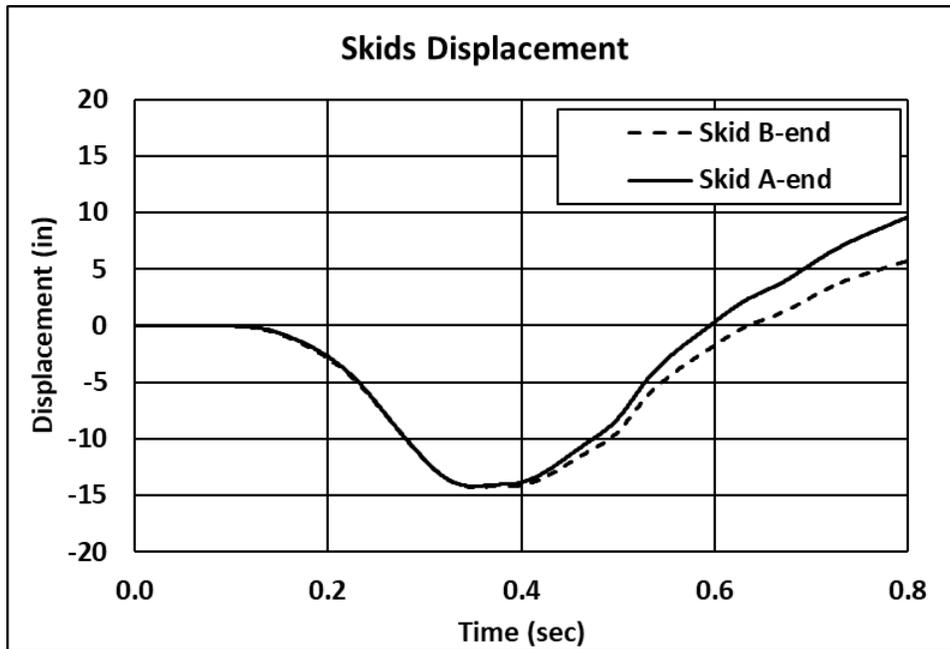r in the tank car's shell. Volpe developed the FE models, which incorporated and expanded upon several modeling techniques used during simulations of previous tank car impact tests (Kirkpatrick, S. W., Rakoczy, P., & MacNeill, R. A., 2015) (Kirkpatrick, S. W, 2010). The DOT-111 models required definition of the tank car geometry, geometry of the impact setup (e.g., impact wall, impactor, etc.), definition of boundary conditions, constraints, initial conditions, and development of several material models. Additionally, modeling features such as element types, mesh sizes, and fluid/structure interactions were selected.

The models were developed using the Abaqus/CAE preprocessor and executed in Abaqus/Explicit (Dassault Systemes Simulia Corp, 2014). Abaqus/Explicit is a commercially available, general purpose nonlinear FE solver capable of simulating impacts involving complex material behaviors such as plasticity and puncture. The Abaqus software also includes several modeling techniques to represent the water and air phases of the lading, permitting these two parts to be modeled explicitly. The solid mechanics simulation features used in the DOT-111 models included modeling an elastic-plastic material response for the tank and jacket, and ductile failure implementation of the Bao-Wierzbicki (B-W) triaxiality-based damage initiation model (Bao, Y., & Wierzbicki, T., 2004). Following the test, the model underwent several adjustments to better represent the actual test conditions.

In an ideal pre-test model, the actual yield strength (YS), ultimate strength (UTS), elongation at break (EB), and the shape of the plastic stress-strain response would be known, and these properties would be used as inputs to the model. Before this test, this tank's material properties could not be known without excising coupons from the tank. The development of the pre-test upper and lower bound estimates of the TC128 material response is described in detail in [Section F3.1](#).

The impact conditions for the test, and therefore the FE model, were chosen specifically to permit comparison between this 2018 test of a DOT-111 tank car that meets CPC-1232 and the 2013 test of a DOT-111 tank car that did not meet CPC-1232 (Kirkpatrick, S. W., Rakoczy, P., & MacNeill, R. A., 2015), the 2014 test of a DOT-112 tank car (Rakoczy, P., & Carolan, M, 2016), and the 2016 test of a DOT-117 tank car (Rakoczy, P., Carolan, M., Gorhum, T., & Eshraghi, S., 2019). As previously described, the 12-inch by 12-inch impactor was used in all these tests.

The air and water phases of the lading were modeled using two different modeling techniques. The air phase of the tank was modeled using a pneumatic cavity approach, while the water phase was modeled with Lagrangian (brick) elements. This same approach was used for the prior test of a DOT-117 tank car (Rakoczy, P., Carolan, M., Gorhum, T., & Eshraghi, S., 2019). Previously, other modeling techniques have been used to capture the response of the air and water phases. For the DOT-112 test, a smoothed particle hydrodynamics (SPH) modeling approach was used to model the air phase, and a Lagrangian (brick) formulation was used for the water phase (Rakoczy, P., & Carolan, M, 2016). A DOT-105 impact test was modeled using a hydraulic cavity modeling approach for the water phase, and a pneumatic cavity modeling approach for the pressurized air phase (Carolan, M., & Rakoczy, P., 2019). The Lagrangian

approach to modeling water is described in Section 5.3.2, and the pneumatic cavity approach to modeling air is described in Section 5.3.3.

Following the test, several changes were introduced to the pre-test FE model to better capture the actual test conditions. The TC128 steel material behaviors in the post-test model were updated based on the results of tensile tests performed on specimens extracted from the tested car. The post-test FE model was run at the measured test speed of 13.9 mph and with the measured weight of the ram car. Because water leakage from the manway and cover plate occurred during the test, the post-test FE model was updated to bound the upper and lower limits of leakage with a fully closed tank and fully open tank.

5.1 Overview of Models

The pre-test and post-test FE models are made of geometry representing the different components in the test setup, material parameters describing the behavior of the materials making up the car and its lading, and numerous constraints, boundary conditions, and loads describing the conditions of the test. As a part of both the pre-test and post-test FE modeling studies, non-puncture models were developed along with puncture-capable models. Non-puncture models featured simplified material behaviors, where the tank and jacket featured only elastic-plastic material responses, but not ductile failure behaviors. Because the material definitions were not capable of simulating puncture, coarser meshes were used on the non-puncture models in the impact zone in the interest of reducing model runtime. The non-puncture models were useful for investigating several parameters, including fluid behaviors, before implementing any new behavior in the more complex puncture-capable models.

Puncture-capable models featured more complex material definitions, capable of simulating element degradation and removal and refined meshes on the tank and jacket in the areas of contact with the impactor. For the tank, this refined area was meshed using solid elements, while the much thinner jacket used a refined shell mesh. Most FE results presented in this report were obtained using puncture-capable models. Several non-puncture post-test FE models were used to examine bounding cases of outage leakage to aid in interpreting the test results. These non-puncture models are discussed in Section C3.

All FE models (i.e., pre-test, post-test, puncture-capable, and non-puncture) used a half-symmetric condition, with a vertical-longitudinal symmetry plane at the centerline of the tank car to reduce the size of the model. The tank geometry was simplified, and structures such as the body bolster were omitted. These simplifications have a relatively minor effect on the impact response of the tank under the test conditions. Figure 36 shows the pre-test model, and its assembly was similar to the post-test model.
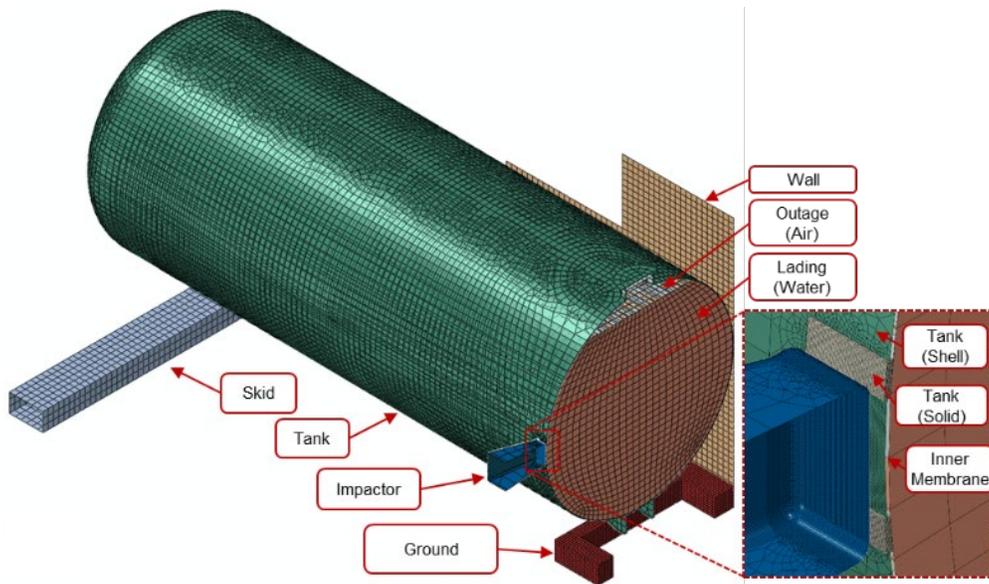
Figure 36. Annotated Pre-test FE Model

5.2 Summary of the Assembly

The parts included in the FE model can generally be divided into three categories: rigid bodies, deformable bodies made of steel, and deformable bodies made of other materials. Because the model was half-symmetric, the part weights in the FE model generally correspond to half of the weight of the actual tested geometry. The exception to this is the skid, as the skid exists entirely to one side of the symmetry plane. Therefore, the model contains the full weight of the skid.

Table 5 summarizes the parts making up the FE model used in the pre-test puncture simulations. This table contains the weight of the part in the model, as well as the weight of the full part (twice the model weight) for applicable parts. Adjustments were made between this model and the post-test models, so the meshes and part weights were slightly different in the post-test models. Appendix D provides a full description of each part in the pre-test and post-test models.

Table 5. Summary of Parts in Pre-Test FE Model

Type of Body	Part Name	Elements No.	Part Weight (Half Sym.) lbf	Part Weight (Full Size) lbf
Rigid	Impactor	7,764	148,000	297,000
Rigid	Rigid Wall	1,341	-	-
Rigid	One Skid	936	11,200	11,200
Rigid	Ground	643	-	-
Deformable, Steel	Tank (Shell Elements)	12,858	19,000	38,000
Deformable, Steel	Tank (Solid Elements)	40,992	7	14
Deformable, Non-steel	Internal Membrane	13,524	330	660
Deformable, Non-steel	Water	77,932	118,000	236,000

From this table, the total weight of the parts in the FE model corresponding to the entire DOT-111 (twice the weight of the half-symmetric model) would be approximately 297,000 lbf. This weight exceeds the 286,000-pound weight limit for a DOT-111 tank car in service. The single heaviest part in both the FE model and the test setup is the water within the tank car. Water was used in the test to account for both the mass and the dynamic effects of a fluid-filled tank car. However, the DOT-111 tank car that meets specification CPC-1232 would typically be used to carry flammable liquids such as ethanol or crude oil. Because it is neither safe not practical to run an impact test using ethanol or crude oil within the tank car, water is used as an analogue. This also simplifies the pre-test and post-test FE modeling, as the mechanical properties of water are well-documented in publicly available sources.

Pure ethanol has a specific gravity of approximately 0.79 (at 70 °F) (DDBST GmbH, n.a). Crude oil is a more complicated substance to compare, as the term refers to a wide variety of substances that can vary greatly in chemical components and physical properties. However, a specific gravity of 0.83 (George, A. K., Singh, R. N., & Arafin, S., 2013) was found for light crude oils at temperatures slightly below the test temperature. Thus, if the tested DOT-111 tank car had been filled with the type of commodity for which the car was originally designed to carry, it would weigh approximately 40,000 to 50,000 lbf less than the water-filled tank car configuration.

5.3   Material Behaviors in FE Models

Two material definitions were used in both the pre-test and post-test FE models without adjustment: an internal membrane and air. The material properties for water were adjusted in the post-test model to match the properties at the temperature of the water in the test. A fourth material, TC128 steel, was modeled using different properties in the pre-test and post-test models. This section summarizes the material properties input to the FE models. Complete descriptions of the development of the TC128 steel characterizations are given in Section F3.

5.3.1   Membrane

An artificial surface was modeled within the tank to define the limits of the pneumatic cavity modeling the outage, which is described in Section D6. Because this surface does not correspond to any physical structure within the tank, modeling techniques were chosen to minimize the increase in either mass or stiffness introduced into the model by the membrane.

38

The membrane part was meshed using surface elements for the portion of the part along the interior of the tank, and with membrane elements for the portion of the part that defined the interface between the water and the outage within the tank. Surface elements do not have a defined thickness or material behavior. Thus, these elements must be constrained to elements with these properties defined to prevent the surface elements from unconstrained distortion. The surface elements were attached to the mid-plane surface of the tank using a tied constraint (see Section E6).

Additionally, a membrane material was defined for the internal surface that divided the gas phase of the lading from the liquid phase. This membrane was modeled as having the same mass density as steel to avoid the minimum time increment becoming dominated by the artificial material in the membrane. Table 6 summarizes the material properties of the membrane.

Table 6. Material Properties Defined for Membrane Material

Parameter	Value
Mass Density ($lbf \cdot s^2/in.^4$)	7.35×10^{-4}
Modulus of Elasticity (*psi*)	3×10^4

5.3.2 Water

The DOT-111 tank car testing occurred with a small (5 percent) outage and with the outage initially at atmospheric pressure. These conditions are similar to the test conditions used in previous tests of a DOT-117 tank car (Rakoczy, P., Carolan, M., Gorhum, T., & Eshraghi, S., 2019) and a DOT-112 tank car (Rakoczy, P., & Carolan, M, 2016). The previous test results indicated the need to model the lading in such a way that the sloshing and pressure increase of the outage could be properly captured. Thus, the water within the DOT-111 tank was explicitly modeled with a Lagrangian mesh, rather than the hydraulic cavity simplification employed in the simulation of the 2016 DOT-105 impact test (Carolan, M., & Rakoczy, P., 2019). While representing the water with an explicit mesh would lead to an increased simulation runtime, it was expected to better capture the complex fluid behaviors anticipated during the test.

The water filling the tank was modeled using an equation-of-state (EOS) model within Abaqus. The pre-test FEA used physical properties of water at a predicted test day temperature of 57 °F. The post-test FEA used physical properties at the actual water temperature of 47 °F. The differences between pre-test and post-test behaviors are small for the properties used in the model. Additionally, both the pre-test and post-test models made use of a "pressure cutoff" feature within the FE software. This feature limited the maximum tensile stress the water could support to 0 psi, effectively limiting the water from experiencing any tensile stresses. Table 7 shows the physical parameters used to describe the water.

Table 7. Material Behaviors Defined for Water

Parameter	Value Input to Pre-test Model	Value Input to Post-test Model
Mass Density (*lbf·s²/in⁴*)	9.41×10^{-5} (Engineering ToolBox, 2003)	9.36×10^{-5} (Engineering ToolBox, 2003)
Speed of Sound (*in/s*)	5.75×10^{4} (Engineering ToolBox, 2004)	5.67×10^{4} (Engineering ToolBox, 2004)
Dynamic Viscosity (*lbf·s²/in²*)	1.72×10^{-7} (Engineering Toolbox, 2004)	2.00×10^{-7} (Engineering Toolbox, 2004)
Tensile Cutoff Pressure (*psi*)	0	0

Several non-puncture simulations of the previously tested DOT-117 tank car were used to guide the selection of mesh type and element size to capture the liquid response for a 5 percent outage. These results are discussed in the test report for the DOT-117 tank car in Appendix F5 – Water, page 149 of Rakoczy et al. (2019).

5.3.3 Air

The gas phase of the lading was modeled as air at an initial pressure of 1 atmosphere, as this was the desired internal pressure for the tank car during the test. Within Abaqus, the air within the outage was modeled as an ideal gas, using a pneumatic cavity modeling technique. This modeling technique requires a surface to be defined that encloses the cavity, with a reference point defined within this cavity to which initial temperature and pressure can be assigned. The initial pressure and temperature are discussed further in Section E9. The pneumatic cavity approach models the entire cavity with a single average pressure and average temperature value, each of which can vary with time. Thus, by using this technique, the air pressure within the model can change as the volume of the tank changes due to the impact. Table 8 summarizes the modeling inputs defined for the air phase of the model.

Table 8. Material Behaviors Defined for Air

Property	Value	Reference
Universal Gas Constant (*R*) *in-lbf/(mol·K)*	73.583	(Engineering ToolBox, 2004)
Molecular Weight (*MW*) *(lbf·s²/in)/mol*	1.654×10^{-4}	(Engineering ToolBox, 2003)

Equation 1 shows the molar specific heat for air calculation.

$$c_{P.m} = c_P \cdot MW$$

Equation 1. Calculation of Molar Specific Heat

Values for the specific heat capacity of air (*C_P*) were obtained from published values (Urieli, 2010). Table 9 shows the calculated values for molar specific heat at different temperatures defined as inputs to the FE models in the unit system used in the FE models.

Table 9. Molar Specific Heat for Air

Temperature (K)	$c_{P.m}$ in-lbf/(mol·K)
250	257.2
300	257.7
350	258.5
400	259.7

5.3.4 AAR TC128 Grade B Steel

One purpose of this test was to subject the tank car to a moderately high-speed impact that was close to the threshold speed between a puncture and a non-puncture outcome. While it was known from the certificate of construction that the 0.5-inch shell in the tank was manufactured from TC128 steel, the actual plastic stress-strain response and elongation at failure would not be known until coupons could be excised from the tank car shell and subjected to tensile testing. Publicly available tensile test data from DOT-111 (National Transportation Safety Board, n/a) (Transportation Safety Board of Canada, 2013) (National Transportation Safety Board, 2012) (National Transportation Safety Board, 2016) and DOT-117 (Rakoczy, P., Carolan, M., Gorhum, T., & Eshraghi, S., 2019) tank cars were compiled and analyzed as a means of developing upper- and lower-bound estimates for pre-test material models. Three rail accidents involving DOT-111 tank cars were identified as having resulted in the publication or public docket release (National Transportation Safety Board, n/a) of tensile test data for TC128 steel. These accidents occurred in Lac-Mégantic, Quebec Canada (Transportation Safety Board of Canada, 2013), Cherry Valley, IL (National Transportation Safety Board, 2012), and Lynchburg, VA (National Transportation Safety Board, 2016). Table 10 summarizes the minimum, maximum, and average properties obtained from surveying the TC128 tensile test data from these accidents.

Table 10. Material Properties for Publicly Available TC128 Steel Samples Excised from DOT-111 and DOT-117 Tank Cars

Property	Minimum	Maximum	Average
YS (*ksi*)	55.3	66.3	62.6
UTS (*ksi*)	77.9	89.4	86.5
EB in 2 inches (*%*)	28.0	42.7	38.2
EB in 8 inches (*%*)	18.0	22.9	21.2

Based on previous material modeling efforts for tank cars performed by Volpe (Rakoczy, P., & Carolan, M, 2016) (Rakoczy, P., Carolan, M., Gorhum, T., & Eshraghi, S., 2019) (Carolan, M., & Rakoczy, P., 2019), pre-test TC128 elastic-plastic material responses were developed that approximated the estimated minimum (lower bound) and maximum (upper bound) properties (see Table 10). The process for developing the plastic stress-strain response is described more fully in Section F3. The material properties for the pre-test and post-test TC128 materials are summarized in Table 11.

**Table 11. Summary of Material Parameters for Pre-test TC128**

Parameter	Value
Mass Density (lbf-s^2/in$^{4)}$)	7.35×10^{-4}
Modulus of Elasticity (psi)	2.79×10^7 psi
Poisson's Ratio	0.3
Plasticity	Piecewise nonlinear (see Section F3)
Damage Initiation	B-W Envelope (see Section F3)
Damage Progression	Linear, 1,200 in.-lbf/in.^{2}
Mesh Implementation	0.083 in. Fully Integrated Brick (C3D8) Elements (6 elements through coupon thickness)

In addition to requiring a plastic stress-strain response, the pre-test FE models required that damage initiation envelope and damage progression behaviors be defined. As described in Section F3, the B-W damage initiation envelopes were iteratively calibrated to result in the desired elongation for a 2-inch gage tensile coupon FE model. Figure 37 shows the nominal stress-strain response obtained from the tensile coupon simulation for the pre-test TC128 steel.
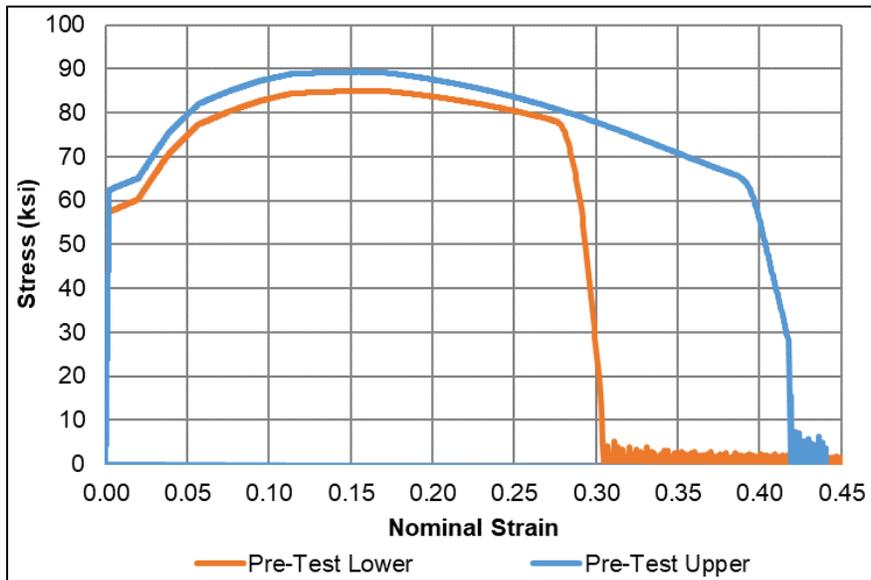
Figure 37. Nominal Stress-strain Response from FEA of a 2-inch Tensile Coupon using Pre-test Lower and Upper Estimates of TC128 Steel Behavior

Figure 38 plots the damage initiation envelopes developed for the pre-test lower estimate and pre-test upper estimate for the DOT-111 tank car test.
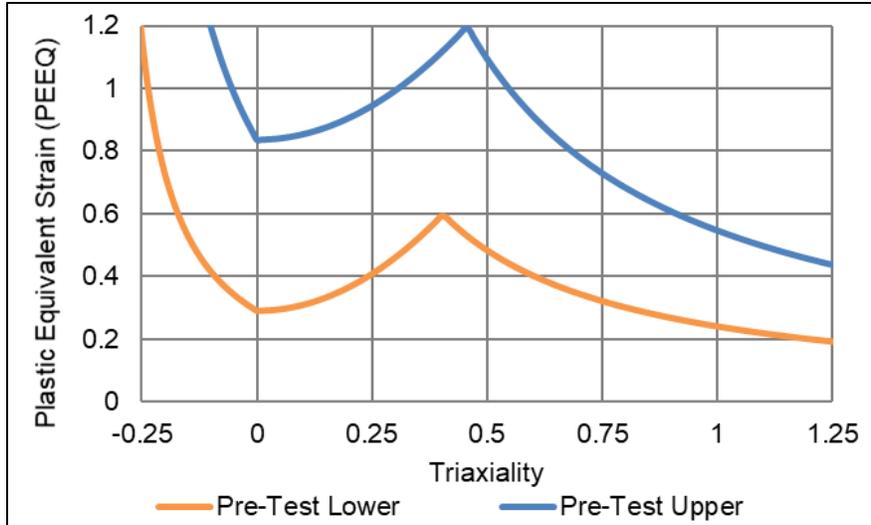
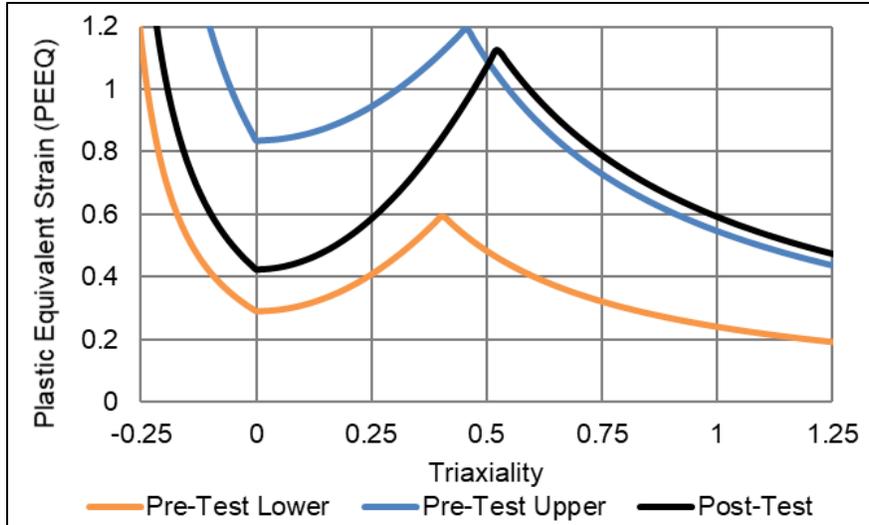**Figure 38. B-W Damage Initiation Envelopes for Pre-test Lower and Upper Estimates of TC128 Steel Behavior**

Post-test TC128 Steel Characterization

After the impact test, material coupons were cut from undamaged areas of the tested DOT-111 tank car and subjected to tensile testing. Smooth round bar tensile coupons were cut from an undamaged portion of the tank car. Subscale dimensions were used for the smooth round bar coupons because the nominal thickness of the shell (0.5-inch) did not permit machining of standard 2-inch gage length, 0.5-inch diameter bars. The subscale dimensions for the smooth round bars were 1.4-inch gage length and 0.35-inch diameter. Figure 39 shows the engineering stress-strain results for the three smooth round bar specimens.
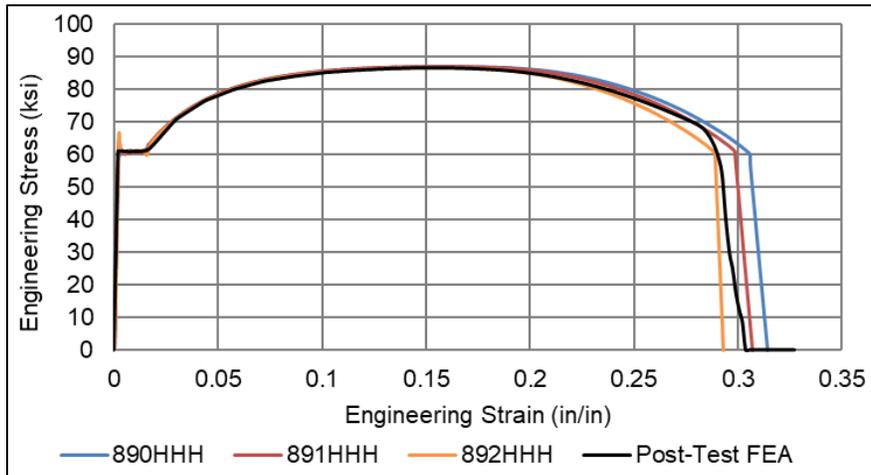
Figure 39. Post-Test Smooth Round Bar (1.4-inch Gage Length) Engineering Stress-Strain Results and Coupon Simulation Results

The Lee-Wierzbicki "quick calibration" procedure (Lee, Y., & Wierzbicki, T., 2004) (Lee, Y.-W., 2005) was used to create a B-W damage initiation envelope from the results of the post-test, subscale coupon testing. Figure 40 shows the post-test damage initiation envelope alongside the envelopes developed for the pre-test models.

43

Figure 40. Post-Test B-W Damage Initiation Envelope with Pre-test Envelopes for Comparison

5.4 Modeling Techniques Adjusted between Pre-Test and Post-Test Models

Several modeling techniques were adjusted in the post-test models, on the basis of either reexamining the model or the outcome of the test. These modeling techniques and their adjustments are described in this section.

5.4.1 Air and Water Leakage

Water leakage through the manway was observed during the test. Two different post-test models were created to bookend the upper limit of air and water leakage (open manway) and the lower limit of air and water leakage (sealed manway). This approach was taken because the leakage of air and water through the manway was an unanticipated result. The flowrate of water was not measured and could not be directly estimated from other measurements made during the test. The test measurements and observations indicate that the actual behavior during the test was somewhere between a tank that was fully open (and thus, unable to develop any pressure above 1 atmosphere) and a tank that was fully sealed (and thus, would have experienced no leakage until PRV activation). Pressure transducer data confirms that the outage did experience some pressure rise, and HS video confirms that the tank experienced leakage through an area other than the PRV.

For the bounding case of an open manway, the pneumatic cavity representing the air at the top of the cavity was removed so that the outage could not increase in pressure as its volume was reduced. This had an effect of softening the global "stiffness" of the tank and reducing the peak impactor's peak force while increasing its displacement. Effectively, this bounding case represented a tank car with a manway that was open to atmospheric pressure, and thus could not increase in pressure in spite of the outage volume reduction caused by the impact.

The sealed manway case was similar to the pre-test models in that the pneumatic cavity was not removed. However, it was observed that the actual PRV in the DOT-111 tank car had a lower flow rate than was initially applied in the pre-test models, so it was lowered to reflect the actual value in the post-test models. This case was thought to represent an upper bound on the test results, as the only path for fluid to escape the tank would be through the PRV once the start-to-

discharge pressure was reached by the fluid cavity. Since the test resulted in fluid leakage through the manway and cover plates prior to the start-to-discharge pressure being reached, this upper bound model was expected to stiffen the global "stiffness" of the modeled tank.

5.4.2 Other Test Conditions

The post-test FE models were updated so that the impactor had an initial speed of 13.9 mph as measured by the speed traps during the test. The impactor was moved approximately 1-inch away from the tank shell to account for the space occupied by the wooden blocks placed under the data acquisition system triggers. The tank was offset from the wall by approximately 1.3 inches to represent the gap measured prior to the test.

The measured temperature at the time of the test was 47 °F, which was 10 °F lower than the pre-test prediction of 57 °F. The material properties of the Lagrangian elements representing the water and the initial temperature of the pneumatic cavity were updated to match the measured temperature.

# 6. Comparison of Test Response to Pre-Test Analysis

One of the intended uses of the pre-test models was to assist in test planning by estimating the range of impact speeds over which puncture would be likely to occur. The models were run using an iterative approach to attempt to determine a speed that would cause puncture without resulting in an excessive amount of residual energy in the impactor at the time of puncture. After using this iterative approach, the model estimated puncture at a speed between 12 and 14 mph, depending on the estimated mechanical properties of TC128 in the shell of the tank. The target speed for the test was chosen to be 13.5 mph based on these results. Thus, a test run at 13.5 mph was in the range of speeds where puncture was a possible outcome, but not the only potential outcome, as Figure 41 shows. The range of expected test speeds was ±0.5 mph around the target speed, or 13 to 14 mph, and the actual test speed was 13.9 mph.
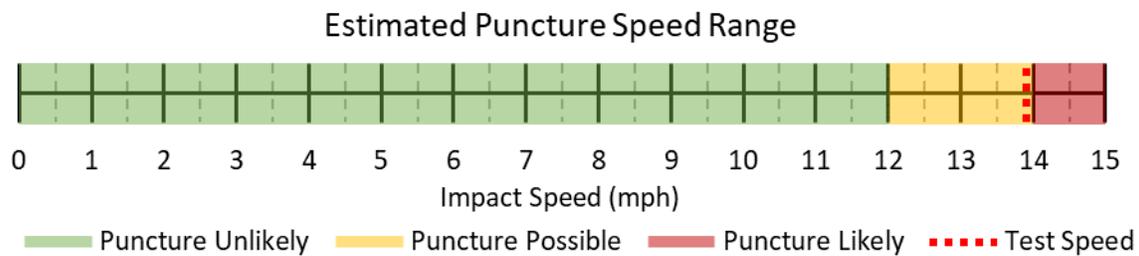
Figure 41. Estimated Puncture Speed Range for the DOT-111 Tank from Pre-test FEA

The pre-test modeling results for the lower and upper bound estimates of TC128 steel at a speed of 14 mph are compared to the test results in this section. This speed was chosen for comparison because it was the closest to the test speed out of the speeds analyzed in the pre-test FEA. In general, there was very good agreement between the 14-mph pre-test FEA results and the measurements made during the test. The complete set of comparisons between pre-test FEA and test results can be found in Appendix C.

The impact force versus impactor travel is compared between each of the pre-test FE models (lower and upper estimates of TC128) and the test measurements in Figure 42. While the FE model used a rigid impactor with a single acceleration-time history, the ram car in the test featured five longitudinal accelerometers. The test force reported is the average of the five longitudinal accelerometer channels. The test data results have been shifted by 0.005 seconds to account for the delay between when the data acquisition system triggered and when the indenter contacted the tank. Additionally, both the test and FE model forces reported in this section have been filtered using a CFC60 filter (SAE International, 2007).
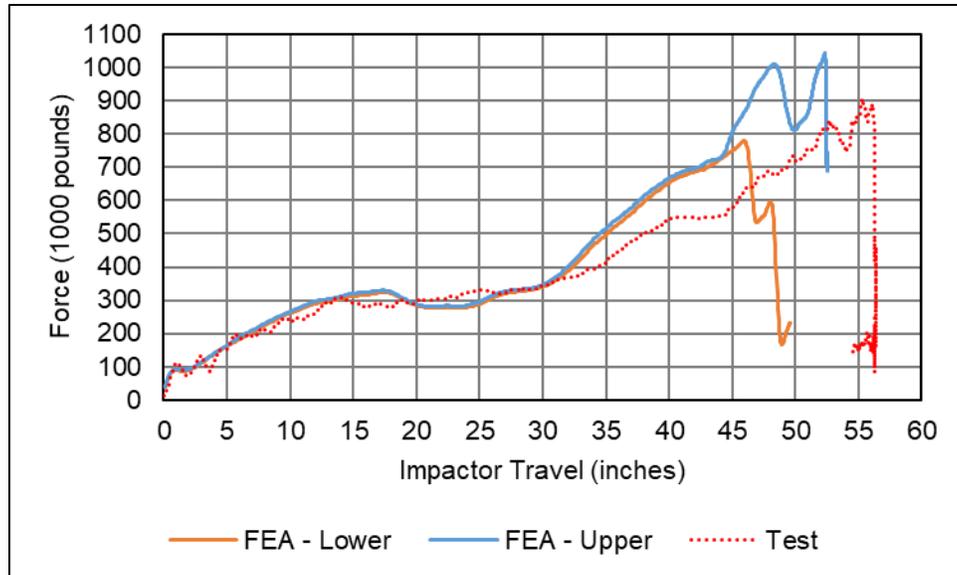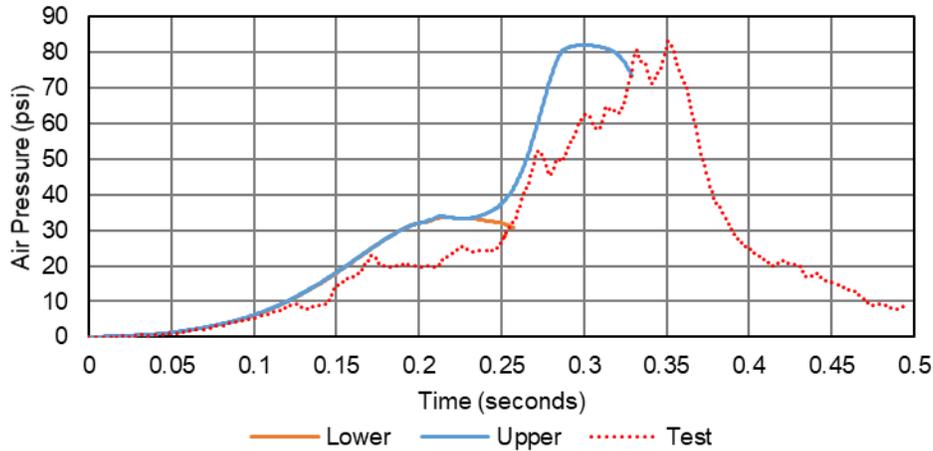
Figure 42. Force-Displacement Responses from Pre-Test FEA with Lower and Upper Estimates of TC128 Steel compared to Test Results

The models effectively captured the overall response of the test, including the changes-in-slope to the response as the impactor deformed the tank car and pushed it back against the wall. Both the lower and upper TC128 steel estimate pre-test FE models showed a qualitatively similar shape to the test measurements over the full range of impactor travel. Quantitatively, both pre-test FE models exhibited very little variation from the test measurements up to 30 inches of impactor travel. After 30 inches of travel, the test force is lower than either pre-test FE model, indicating that the models exhibited a stiffer response than was measured in the test. The apparently softer response of the tested tank car is attributed to the leakage of air and water through the manway and cover plate during the test. The discrepancy in global force-indentation stiffness after 30 inches of travel between the pre-test FE models and the test measurements is explored in detail in Appendix C. Both the pre-test FE models and the test resulted in puncture. It should be noted that the pre-test FE models were run at a speed of 14 mph while actual test speed was 13.9 mph, but it is not expected that this small difference in speed would substantially change the pre-test FEA results.

The test measurements showed a larger maximum indentation than either pre-test model, and the test peak force was approximately halfway between the lower and upper pre-test model estimates. The test resulted in a peak force of approximately 900 kips while the lower and upper estimates resulted in 800 and 1,000 kips, respectively. The test resulted in puncture of the tank after approximately 57 inches of impactor travel, while it punctured after 47 inches of travel in the lower pre-test estimate and 52 inches of travel in the upper pre-test estimate.

Figure 43 shows a comparison plot of air pressure for the lower and upper estimate pre-test FE models and for the test. For each FE model result, the air pressure is plotted as the average air pressure in the outage. For the test data, the average value from three pressure transducers in the outage (i.e., TPMH, TP1000, and TP2000) is plotted. The data results from each channel are shown in Section B2. Note that leakage of water from the manway was first observed after approximately 0.16 seconds of impact time (see Figure 21). Since the pressure relief valve was initially in communication with the air-filled outage, it is likely that air was initially expelled through the gasket

between the manway and its cover plate prior to the water leakage. However, since any air leakage was not visible on the test videos, it is not possible to determine when such leakage began, or the surfaces from which air escaped. Leakage from the manway was not expected prior to the test and likely resulted in the discrepancy between the pre-test FEA and test results.

Figure 43. Average Air Pressure-time Responses from Pre-test FEA with Lower and Upper Estimates of TC128 Steel compared to Test Results

Figure 44 contains plots comparing the internal string potentiometer measurement at the center of the car against the pre-test FE models with lower and upper estimates of TC128 steel. During the test, the string potentiometer at this location reached its measurement limit, resulting in the horizontal line seen after approximately 0.25 seconds. In both pre-test FE models, the model captures the general shape of the test response, including a change-in-slope measured at 0.2 seconds during the test.
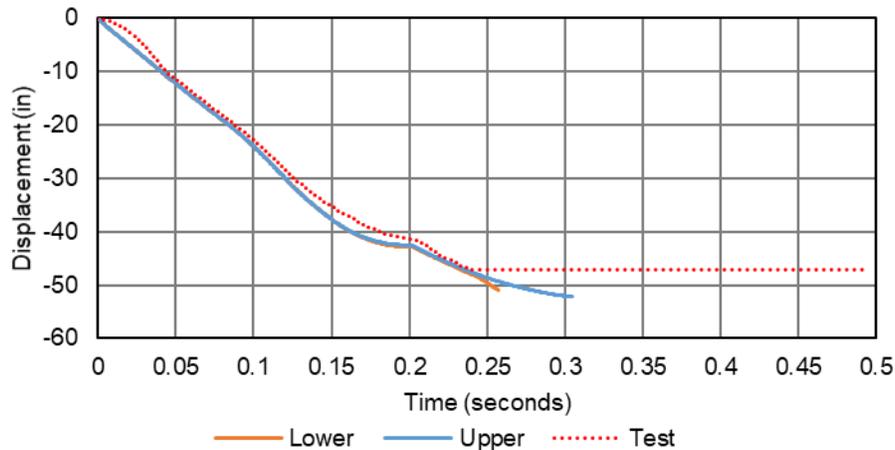
Figure 44. Change in Center String Potentiometer Length for Pre-Test FEA with Lower and Upper Estimates of TC128 Steel compared to Test Results

Figure 45 contains plots comparing the vertically oriented internal string potentiometer measurements at the center of the car against the pre-test FE model results with lower and upper estimates of TC128 steel. Both of the pre-test FE models exhibited good agreement with the test results in terms of the overall shapes of the curves. The pre-test FEA with the upper estimate of

48

TC128 steel was in good agreement with the test results when comparing the maximum change in length (approximately 21 inches). The lack of agreement with the model having the lower estimate of TC128 steel is attributed to premature puncture at approximately 0.25 seconds in the model versus 0.35 seconds in the test.
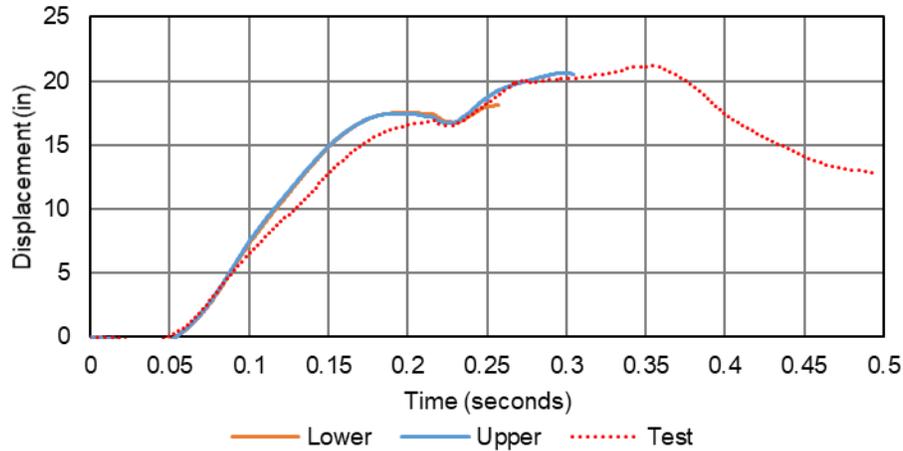
Figure 45. Change in Vertical String Potentiometer Length for Pre-Test FEA with Lower and Upper Estimates of TC128 Steel compared to Test Results

Table 12 presents a summary of the level of agreement between the peak measurements from the pre-test FEA with lower and upper estimates of TC128 steel and the test results. The pre-test FE results with the upper estimate of TC128 steel were in better qualitative (shape) and quantitative (magnitude) agreement for the values compared with the test data than the pre-test FE results with the lower estimate of TC128 steel. For many of the displacement results, the pre-test FEA estimated a value below the test measurements. This outcome is consistent with the post-test observation that the manway was not fully sealed during the test.

Table 12. Comparison of Peak Results from Pre-Test FEA with Lower and Upper Estimates of TC128 Steel and Test Results

Peak Measurement	Test	Lower FEA	Lower FEA	Upper FEA	Upper FEA
	Value	Value	%	Value	%
Longitudinal Acceleration (*g*)	-3.1	-2.6	-14.1%	-3.5	15.1%
Impact Force (*kip*)	906.6	778.6	-14.1%	1043.2	15.1%
Displacement at Peak Force (*in.*)	55.3	45.9	-16.9%	52.3	-5.3%
48″ Offset String Potentiometer (*in.*) †	-36.6	-35.0	-4.5%	-38.2	4.3%
48″ Offset String Potentiometer (*in.*)	-40.9	-35.0	-14.5%	-38.2	-6.6%
24″ Offset String Potentiometer (*in.*) †	-45.5	-41.8	-8.0%	-45.7	0.6%
24″ Offset String Potentiometer (*in.*) †	-35.3	-41.8	18.6%	-45.7	29.7%
Center String Potentiometer (*in.*) †	-47.0	-51.0	8.4%	-52.2	11.0%
Vertical String Potentiometer (*in.*)	21.2	18.1	-14.7%	20.6	-2.9%
Skid String Potentiometer (*in.*)	-14.3	-7.4	-48.4%	-14.6	2.0%
Skid String Potentiometer (*in.*)	-14.2	-7.4	-48.1%	-14.6	2.7%
Head String Potentiometer (*in.*)	-14.7	-7.6	-48.5%	-14.1	-4.2%
Head String Potentiometer (*in.*)	-14.9	-7.6	-48.9%	-14.1	-4.9%
Average Air Pressure (*psi*)	83.2	33.6	-59.6%	82.1	-1.3%

†Denotes longitudinal string potentiometers that reached their limit during the test (as seen in Figure 32)

# 7.   Comparison of Test Response to Post-Test Analysis

Following the test, the updates to the pre-test FE model included the actual material properties of the TC128 steel from the tested tank car and impacting at the measured test speed of 13.9 mph. Two post-test FE models were created to represent the upper and lower limits of leakage through the manway. The first model fully sealed the manway and only allowed air flow through the PRV. The expectation of this model was to represent the lower-bound of leakage, which would represent an upper-bound for tank car stiffness. The second post-test FE model removed the pneumatic cavity representation of the outage, resulting in an outage unable to increase in pressure during the impact. This second model was expected to represent the upper-bound of leakage, which would represent a lower-bound for tank car stiffness. The post-test modeling results for these two cases are compared to the test results in this section. In general, the post-test FE results from the two cases could bound the peak measurements made during the test. These models were intended as simplified tools to examine whether the discrepancies in the pre-test FE model can be attributed to the imperfectly sealed tank car during the test. As simplified tools, the post-test FE models did not attempt to quantify the rate of water or air leakage from the tank. The post-test FE models did not have the ability to leak water, but they used the ability of the air phase to pressurize as a stand-in for the effects of venting liquid and gas as occurred in the test.

The post-test FE model with the sealed and open tanks terminated shortly after puncture at 0.27 and 0.31 seconds, respectively. At that point, elements which were involved in shell-to-solid coupling near the impact zone became highly distorted, and the simulation terminated. More information on shell-to-solid coupling is available in Section E8. Since the distortion occurred after puncture and had already initiated in the solid patch of elements, the models were not re-run to attempt to simulate a longer post-puncture event. Figure 46 is a plot of the impactor force versus time for both post-test FE models and the test measurement results. Both post-test models experienced early puncture and subsequent termination before the time of puncture in the test at approximately 0.35 seconds. The post-test models were in good agreement with the measured peak force from the test of approximately 900 kips. All the forces reported in this section have been filtered using a CFC60 filter (SAE International, 2007).
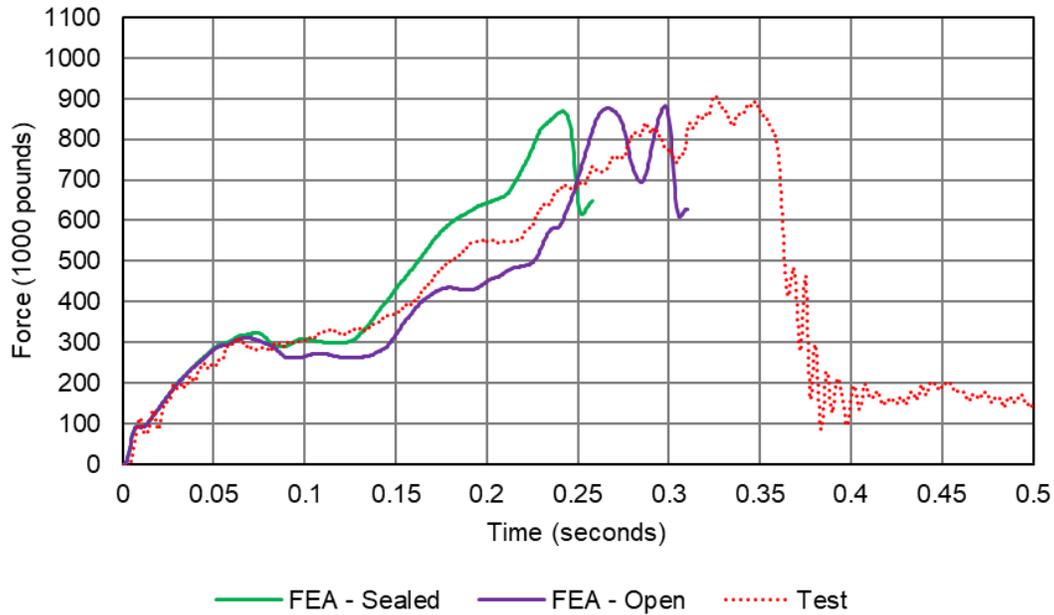
Figure 46. Impact Force vs. Time, Post-Test FEA with Sealed and Open Tank and Test Measurement Data

Figure 47 contains a plot of the impactor force versus displacement for both the sealed and open post-test FE models compared with the test results. Starting at a displacement of 0 inch until a displacement of 30 inches, both the sealed and open post-test FE models are in good agreement with the test results. As the tank stiffens and the force level increases above 350 kips, the sealed tank overestimates the impactor force and the open tank underestimates the impactor force, successfully bounding the test results. The DOT-111 tank car punctured at an approximate impactor displacement of 57 inches in the test, while the sealed tank FE model punctured at 48 inches and the open tank FE model punctured at 56 inches. The open tank FE model only slightly under predicted the impactor displacement at the time of puncture. These results also show that the initial response of the tank car over the first 15 inches of indentation in the test and both post-test FE models are independent of the outage behavior.
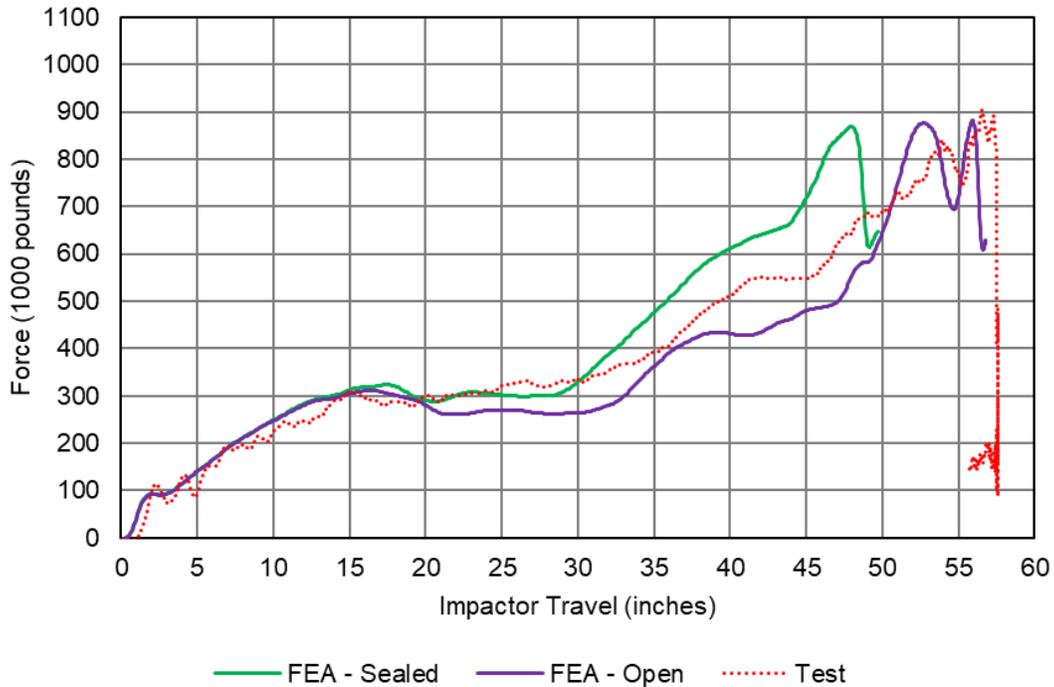
Figure 47. Impact Force vs. Impactor Travel, Post-Test FEA with Sealed and Open Tank and Test Measurement Data

The ram car had a kinetic energy of 1.92 million foot-pounds at the time it impacted the DOT-111 tank car in the test. In the test, the ram car had a residual speed of approximately 0.5 mph while the impactor had a residual speed of approximately 6 mph in the sealed tank model and 4.5 mph in the open tank model. In the test, approximately 96 percent of the ram car's initial kinetic energy was dissipated by the time the peak force was reached while the sealed tank model car dissipated 78 percent and the open tank dissipated 87 percent of the initial energy.

Figure 48 shows three side cut frames from the impact progression spaced 0.125 seconds apart for both post-test FE models. The open tank FE model had a visibly larger amount of deformation, and the water swelled higher due to the lack of a pneumatic cavity. In the sealed tank FE model, the pneumatic cavity pushed back against the water surface resulting in a stiffer overall response. From both FE models, it is apparent that the water has been displaced up into the manway by 0.125 seconds. This response is consistent with the test observations, where water was visibly escaping the cover plate by approximately 0.160 seconds (see Section 4.3.2).

53
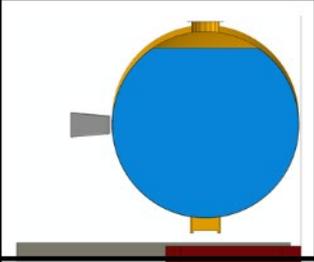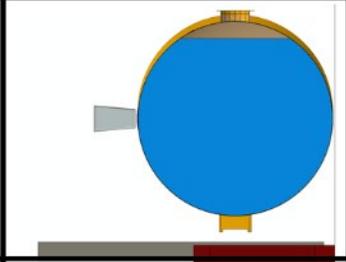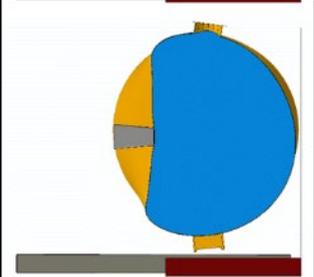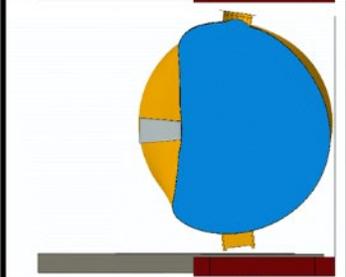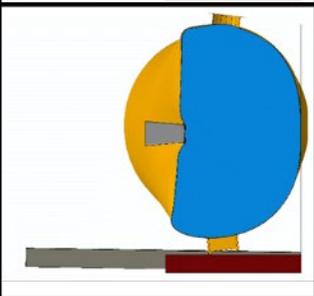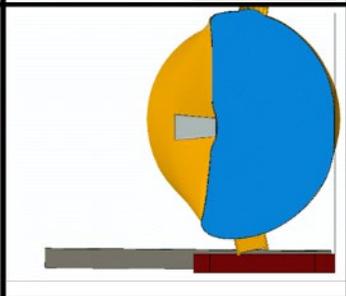
Figure 48. Side View of Impact Progression, Post-Test FE Models with Sealed Tank (left) and Open Tank (right)

Figure 49 is a plot of the average air pressure within the outage of the DOT-111 tank car measured during the test compared with the sealed and open tank post-test FE models. The open tank FE model has a constant pressure of 0 psi because the pneumatic cavity representing the air has been removed. The sealed tank FE model agrees with the test results up to approximately 0.13 seconds of impact time. The discrepancy after 0.13 seconds is attributed to leakage of air and water through the manway seal (see Figure 21). While water leakage was not observed in the HS video until 0.16 seconds, it is reasonable to infer that air was able to leak out of the manway earlier.
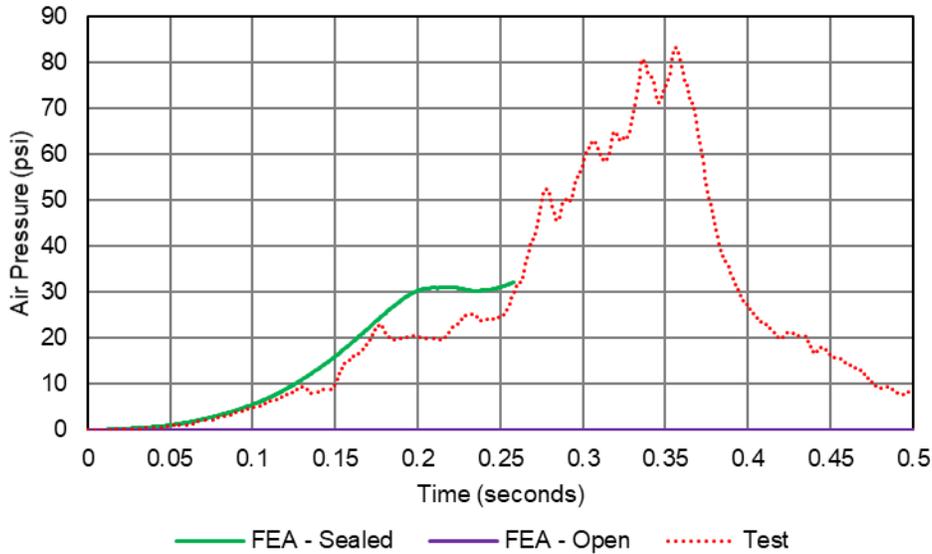
Figure 49. Outage Air Pressure vs. Time, Post-Test FEA with Sealed and Open Tank and Test Measurement Data

Figure 50 is a plot of the center string potentiometer (TD3Y) internal displacement versus time measured during the test and calculated from the post-test FE models. The overall shape of the curves is similar, and the sealed tank FE model captures the change in slope in the test result approximately 0.2 seconds into the impact. The open tank FE model also has a similar change in slope, but it occurs later in the impact and after the tank shell has displaced further. The flat response in the test measurement after 0.25 seconds of impact time is due to the string potentiometer reaching the limit of its displacement.
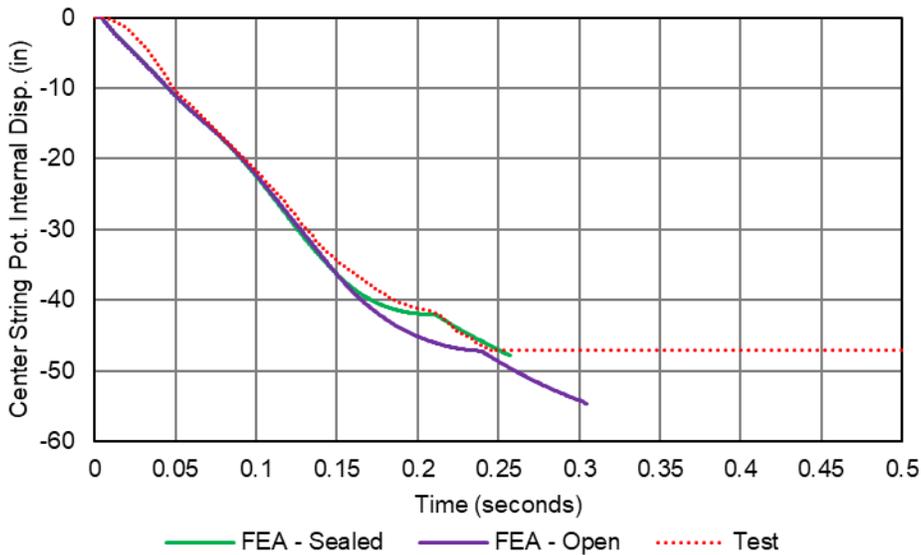
Figure 50. Center String Potentiometer Internal Displacement vs. Time, Post-Test FEA with Sealed and Open Tank and Test Measurement Data

Figure 51 is a plot of the vertical string potentiometer (TD3Z) internal displacement versus time measured during the test and calculated from the post-test FE models. The vertical displacement

55

characterizes the ovalization of the tank as it is pushed back against the rigid wall. The overall shape of the curves is similar, and the sealed tank FE model captures the change in slope in the test result approximately 0.2 seconds into the impact. The open tank FE model has a similar change in slope, but it occurs later in the impact and after the tank shell has displaced further.
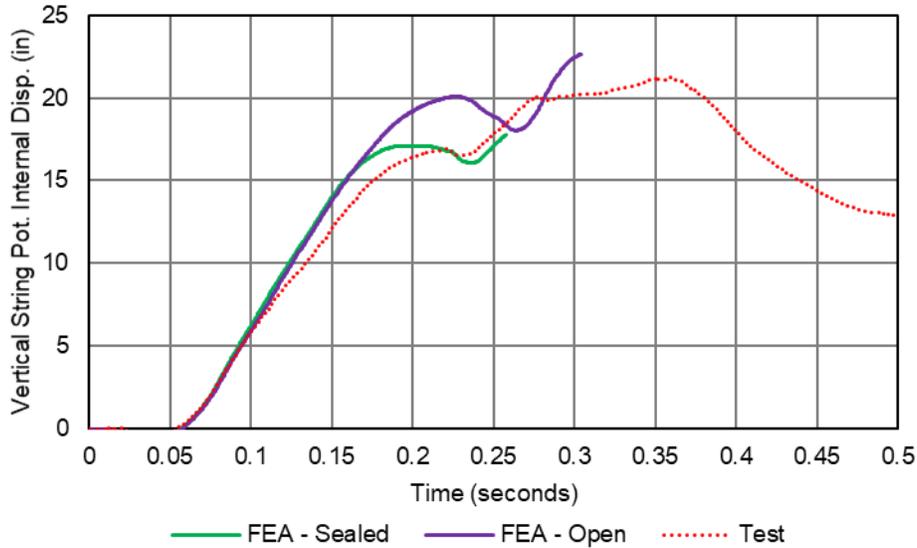
Figure 51. Vertical String Potentiometer Internal Displacement vs. Time, Post-Test FEA with Sealed and Open Tank and Test Measurement Data

Figure 52 compares the A-end (TDASKID) and B-end (TDBSKID) skid displacements measured during the test and the skid displacement calculated in the post-test FE model. The overall shape of the three responses is similar; however, the puncture of the FE models limited the length of impact time that was simulated. Thus, the FE results do not include the skid behavior measured after the tank rebounded off the rigid wall, while the test measurements do capture this rebound behavior.

56
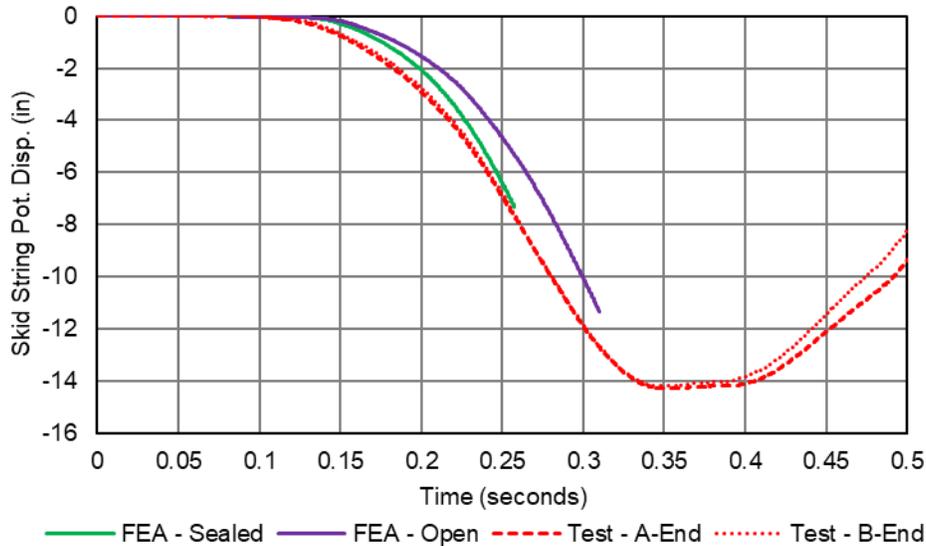
**Figure 52. Skid Displacement in Post-Test FEA with
Sealed and Open Tank and Test Measurement Data**

Figure 53 compares the A-end (TDAEND) and B-end (TDBEND) head displacements measured during the test and the head displacement calculated in the post-test FE model. The overall shape of the responses is similar.
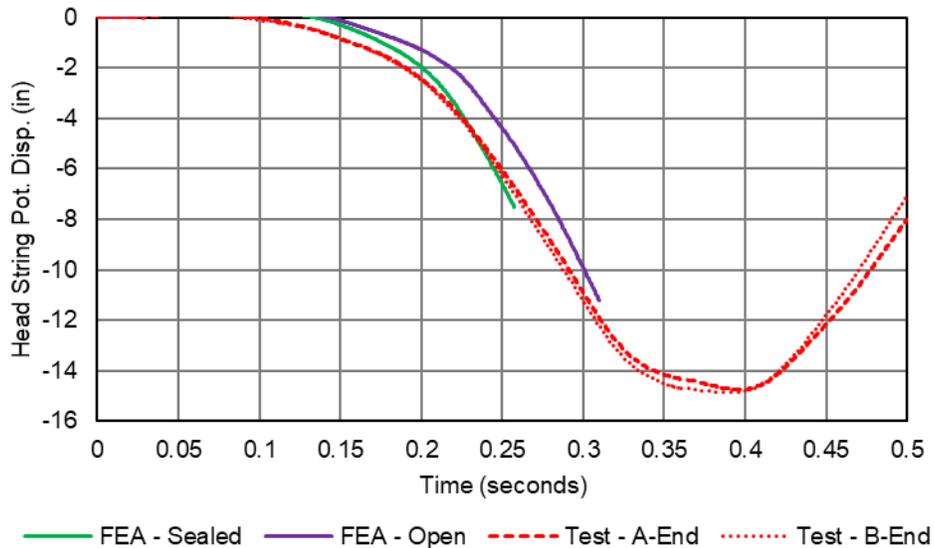
**Figure 53. Head Displacement in Post-Test FEA with
Sealed and Open Tank and Test Measurement Data**

The complete set of test measurement and post-test FEA results are compared in Appendix C. Table 13 compares the peak measurements from the test and the corresponding peak value calculated for each output in the post-test FE model with each outage condition. This table also includes a column indicating the difference between the test measurement and FE calculations. The post-test FE models agreed with the test measurements.

57

**Table 13. Comparison of Peak Results from Post-Test FE Models with
either Sealed or Open Tank and Test Measurement Results**

Peak Measurements	Test	Post-Test FEA Sealed Tank	Post-Test FEA Sealed Tank	Post-Test FEA Open Tank	Post-Test FEA Open Tank
	Value	Value	%	Value	%
Longitudinal Acceleration (*g*)	-3.1	-2.9	-4.2%	-3.0	-2.8%
Impact Force (*kip*)	906.6	868.8	-4.2%	881.4	-2.8%
Displacement at Peak Force (*in.*)	55.3	48.0	-13.2%	55.9	1.1%
48″ Offset String Potentiometer (*in.*) [†]	-36.6	-34.9	-4.7%	-41.6	13.5%
48″ Offset String Potentiometer (*in.*)	-40.9	-34.9	-14.7%	-41.6	1.6%
24″ Offset String Potentiometer (*in.*) [†]	-45.5	-41.9	-7.7%	-48.3	6.2%
24″ Offset String Potentiometer (*in.*) [†]	-35.3	-41.9	18.9%	-48.3	36.8%
Center String Potentiometer (*in.*) [†]	-47.0	-48.7	3.6%	-55.1	17.1%
Vertical String Potentiometer (*in.*)	21.2	18.2	-14.1%	22.6	6.7%
Skid String Potentiometer (*in.*)	-14.3	-8.4	-41.2%	-11.3	-20.8%
Skid String Potentiometer (*in.*)	-14.2	-8.4	-40.8%	-11.3	-20.3%
Head String Potentiometer (*in.*)	-14.7	-8.6	-41.6%	-11.2	-24.0%
Head String Potentiometer (*in.*)	-14.9	-8.6	-42.0%	-11.2	-24.6%
Average Air Pressure (*psi*)	83.2	34.1	-59.0%	0.0	-

[†]Denotes longitudinal string potentiometers that reached their limit during the test (as seen in Figure 32)

Overall, the post-test FE results with the open tank model were in better agreement with the peak test measurements than the closed tank FE model. Neither FE model captured the air pressure response from the test (see Figure 49) because the observed leakage of air and water out of the tank's manway was not modeled. It should be noted that all the longitudinal string potentiometers, except for one 48-inch offset string potentiometer (TD5Y), reached their measurement limits, and thus they did not capture the actual peak displacements in the tank.

FE simulations of tank car puncture performed alongside previous tests have been conservative in predicting puncture (Rakoczy, P., & Carolan, M, 2016) (Rakoczy, P., Carolan, M., Gorhum, T., & Eshraghi, S., 2019) (Carolan, M., & Rakoczy, P., 2019). Since both the sealed and open tank post-test FE models in this study punctured with less energy dissipated by the tank than in the test, the model of the DOT-111 tank car that meets voluntary industry standard CPC-1232 remains slightly conservative.

8. Conclusion

This report documents the combined efforts of TTCI and Volpe to test and analyze the side impact puncture performance of a DOT type 111A100W1 tank car that meets voluntary industry standard CPC-1232 on October 30, 2018. This testing and analysis supports FRA's tank car research program to provide the technical basis for rulemaking on enhanced and alternative performance standards for tank cars.

The tank car was filled with water to approximately 95 percent of its volume. It was then sealed, but not pressurized above atmospheric pressure. The test was intended to strike the tank car at a speed high enough to result in significant damage to the tank and possibly puncture the tank's shell. The tank car was impacted by a 297,150-pound ram car traveling at 13.9 mph. A 12-inch by 12-inch indenter fitted to the ram car impacted the tank center. The impact deformed and tore the tank resulting in loss of lading. A video of the point of impact taken from onboard the ram car successfully captured the initiation of puncture and its propagation for the first time in this testing series. This video confirmed that while the impact occurred on a circumferential weld seam, the tank initially tore not at the weld but in the base material beneath the corner of the impactor. This initial tear propagated into the weld zone, and it proceeded to continue around the circumference of the tank car along the weld.

The test delivered a successful impact at a measured speed that was close to the desired impact speed, as estimated by the pre-test FE models. The pre-test models allowed for a successful estimation of the speed range that would cause puncture of the tank without imparting an excess amount of kinetic energy. Water leakage through the manway and cover plates during the test was an unexpected outcome apparently caused by imperfect seals at the manway and cover plate. This leakage was sufficient to affect the deceleration of the ram car, which occurred at a more gradual rate than if the tank car were completely sealed. As a result, the force-indentation response of the tested tank car was softer than that predicted by pre-test FE models, which assumed the car was airtight until the PRV activated. In spite of this unexpected leakage, the impact speed of 13.9 mph was close enough to the speed necessary to just cause puncture that the ram car was brought to a stop shortly after the onset of puncture and rebounded from the tank car.

Pre-test FE modeling was used to estimate the overall response of the tank to the impact, including the force-displacement response. Because of uncertain parameters (e.g., material properties, actual test speed), the pre-test models were intended to bound the range of likely puncture speeds. The model estimated that the tank could puncture after an impact of between 12 mph and 14 mph, depending on the specific properties of the TC128 steel in the car's shell. The pre-test models showed qualitatively good agreement with the measured force-displacement result from the test.

The FE modeling performed in this effort used an explicit Lagrangian mesh and a simplified pneumatic cavity modeling technique to simulate the water and air responses, respectively. Researchers chose a detailed representation of the water based on the pre-test assumption that the combination of a small and unpressurized outage would lead to complex fluid sloshing within the tank, requiring a detailed representation in the model. The test measurements confirmed that this modeling approach provided a good representation of the fluid behavior in the tank car.

Several changes were made to the FE model after the test. Material coupons were cut from undamaged regions of the tested tank car and subjected to tensile testing. These coupons were used

to generate a new material response, which was implemented in the post-test FE model. Additionally, the post-test FE model was run at the actual 13.9 mph impact speed measured during the test. Due to the water leakage observed from the manway and cover plate during the test, two versions of the post-test FE model were run with the manway either fully sealed or open. These post-test FE models confirmed the hypothesis that disagreement in the overall stiffness of the tank car exhibited by the pre-test FE models was caused by the imperfect seal in the test tank car. This imperfect seal effectively prevented the tested tank car from developing the magnitude of pressure that would have resulted from a perfectly sealed tank. This result underscores the significance of the effects of both the water and the air inside the tank during the test.

9. References

Association of American Railroads. (1978). AAR Specifications for Tank Cars, Section C. M-1002. In *Manual of Standards and Recommended Practices (MSRP).* Washington, DC: AAR.

Bao, Y., & Wierzbicki, T. (2004). On fracture locus in the equivalent strain and stress triaxiality space. *International Journal of Mechanical Sciences, 46*(1), 81-98.

Carolan, M., & Rakoczy, P. (2019, May). Side Impact Test and Analyses of a DOT-105 Tank Car. Technical Report No. DOT/FRA/ORD-19/12. Washington DC: U.S. Department of Transportation, Federal Railroad Administration.

Dassault Systemes Simulia Corp. (2014). *Abaqua 6.14-2.* Providence: Dassault Systemes Simulia Corp.

DDBST GmbH. (n.a). *Saturated Liquid Density.* DDBST GmbH.

Dorsey, K. B. (2011). *AAR Manual of Standards and Recommended Practices Specifications for Tank Cars.* CPC-1232. Washington, DC: Association of American Railroads.

Elkins, A. (2017). *Field Guide to Tank Cars.* Third Edition. Wasington, DC: Association of American Railroads/Bureau of Explosives.

Engineering ToolBox. (2003). *Air Altitude, Density, and Specific Volume.* Engineering ToolBox.

Engineering ToolBox. (2003). *Water - Density, Specific Weight and Thermal Expansion Coefficient.* Engineering ToolBox.

Engineering ToolBox. (2004). *Air - Molecular Weight and Composition.* Engineering ToolBox.

Engineering ToolBox. (2004). *The Individual and Universal Gas Constant.* from Engineering ToolBox.

Engineering ToolBox. (2004). *Velocity of Sound in Water.* Engineering ToolBox.

Engineering Toolbox. (2004). *Water -- Dynamic and Kinematic Viscosity.* Engineering ToolBox.

George, A. K., Singh, R. N., & Arafin, S. (2013). Equation of State of Crude Oil Samples. *Journal of Petroleum & Environmental Biotechnology, 4*(6). doi:doi: 10.4172/2157-7463.1000162.

Kirkpatrick, S. W. (2010, January). *Detailed Puncture Analyses of Various Tank Car Designs - Final Report - Revision 1.* Washington, DC: U.S. Department of Transportation, Federal Railroad Administration.

Kirkpatrick, S. W., Rakoczy, P., & MacNeill, R. A. (2015, October). Side Impact Test and Analyses of a DOT-111 Tank Car. Technical Report No. DOT/FRA/ORD/15-30. Washington DC: U.S. Department of Transportation, Federal Railroad Administration.

Lee, Y., & Wierzbicki, T. (2004, August). Quick Fracture Calibration for Industrial Use. *Impact & Crashworthiness Laboratory Report No. 115*.

Lee, Y.-W. (2005). *Fracture Prediction in Metal Sheets.* Department of Ocean Engineering. Boston, MA: Massachusetts Institute of Technology.

National Transportation Safety Board. (2012, February 14). *Derailment of CN Freight Train U70691-18 with Subsequent Hazardous Materials Release and Fire.* Accident Report NTSB/RAR-12/01 PB2012-916301. Cherry Valley, IL.

National Transportation Safety Board. (2016). *National Transportation Safety Board Railroad Accident Brief, Derailement of WMATA Metrorail Train in Interlocking Falls Church, VA.* NTSB/RAB-16/01. Washington, DC: National Transportation Safety Board.

National Transportation Safety Board. (n/a). *NTSB: Docket Management System.*

Ohio Medical Corporation. (2017). ACFM vs. SCFM vs. ICFM Series of Technical White Papers from Ohio Medical Corporation. Retrieved from www.ohiomedical.com.

Pipeline and Hazardous Materials Safety Administration, DOT. (2015). *Authenticated U.S. Government Information GPO.* Retrieved from Title 49 Code of Federal Regulations Section 179.16, Tank-head puncture-resistance systems.

Rakoczy, P., & Carolan, M. (2016, December). Side Impact Test and Analysis of a DOT-112 Tank Car. Technical Report No. DOT/FRA/ORD-16/38. Washington, DC: U.S. Department of Transportation.

Rakoczy, P., Carolan, M., Gorhum, T., & Eshraghi, S. (2019, May). Side Impact Test and Analyses of a DOT-117 Tank Car. Technical Report No. DOT/FRA/ORD-19/13. Washington, DC: U.S. Department of Transportation, Federal Railroad Administration.

SAE International. (2007). *SAE J211-1 (1995): Instrumentation for Impact Test, Part 1, Electronic Instrumentation.* Rev. Mar95. Warrendale, PA: The Executive Director Office of the Federal Register.

Transportation Safety Board of Canada. (2013, July 06). *Railway Investigation Report R13D0054.* Retrieved from Government of Canada.

Transportation Technology Center, Inc. (2016). *Test Implementation Plan for FRA Tank Car Side Impact, Revision 1.* Pueblo, CO: Association of American Railroads.

U.S. Climate Data version 3.0. (2019). *Climate Pueblo - Colorado and Weather Averages Pueblo.* Retrieved from www.usclimatedata.com.

U.S. Geologic Survey. (2019). *Pueblo Memorial Airport.* Retrieved from USGS Geographic Names Information System.

Urieli, I. (2010). *Specific Heat Capacities of AIr. Engineering Thermodynamics - A Graphical Approach.* Retrieved from Engineering Thermodynamics.

Appendix A.
Camera and Target Positions
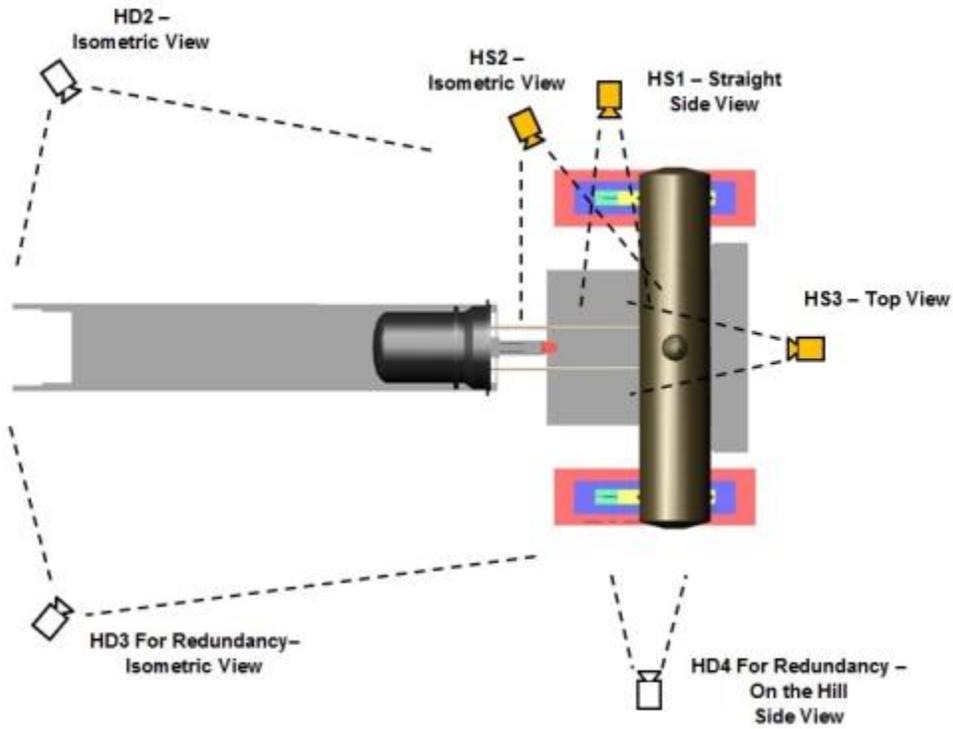
Figure A1. Camera Positions (top) — High Speed (HS), High Definition (HD)
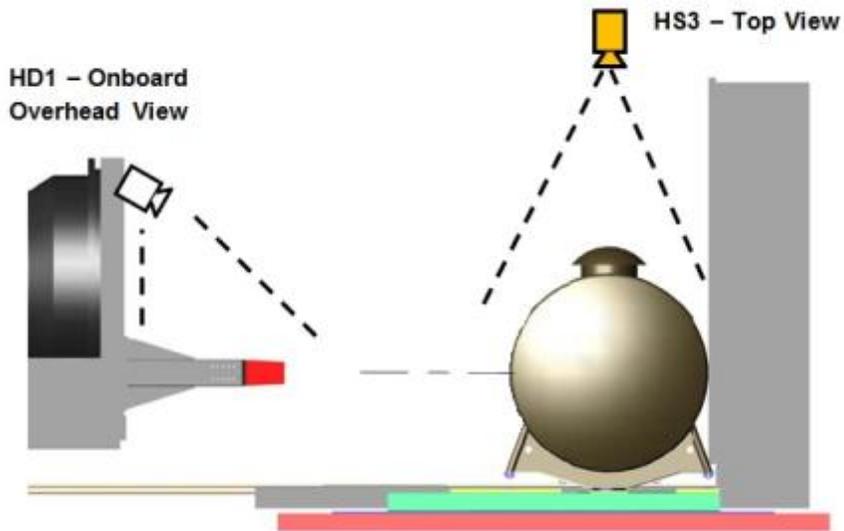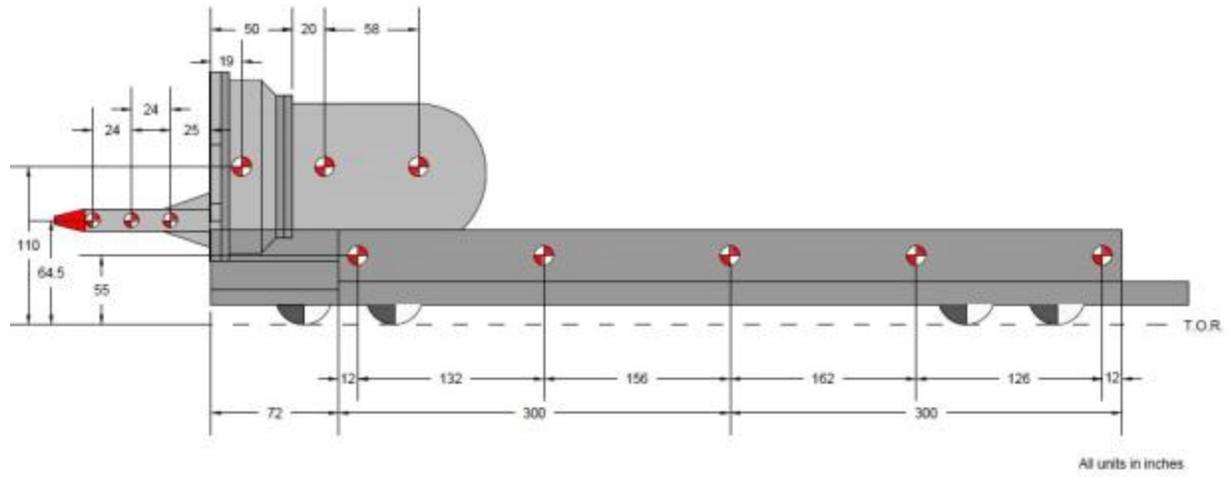

**Figure A2. Camera Positions (side) — High Speed (HS), High Definition (HD)**

**Figure A3. Ram Car Target Positions**

Appendix B.
Test Data

This appendix contains raw and filtered test data. The raw accelerations and internal pressures measured on different locations on the impact cart were processed as follows. The test data from -1 to -0.1 seconds on each channel were averaged, and this value was subtracted from the test measurements to remove any initial offsets in the data. Each channel was then filtered to channel frequency class (CFC) 60, using the procedures given in SAE J211 (SAE International, 2007). Displacement data did not require any filtration.

B1 – Accelerations
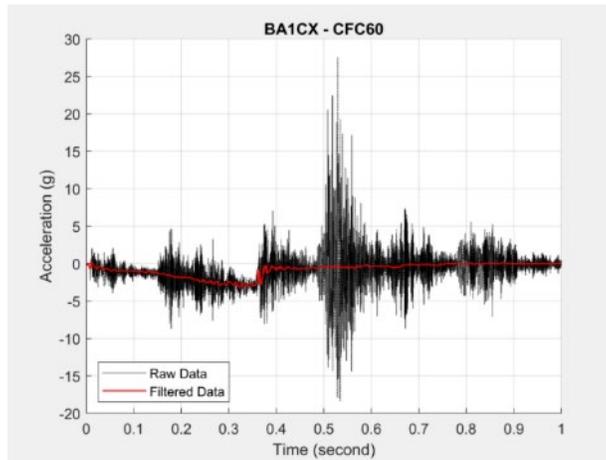
Figure B1. Raw and CFC60 Filtered Acceleration-Time Data from BA1CX
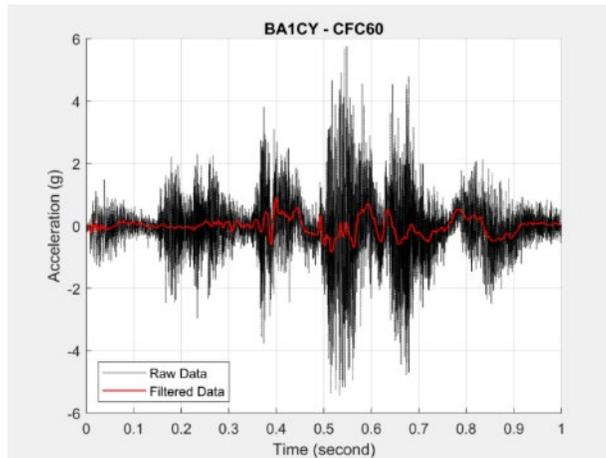
Figure B2. Raw and CFC60 Filtered Acceleration-Time Data from BA1CY
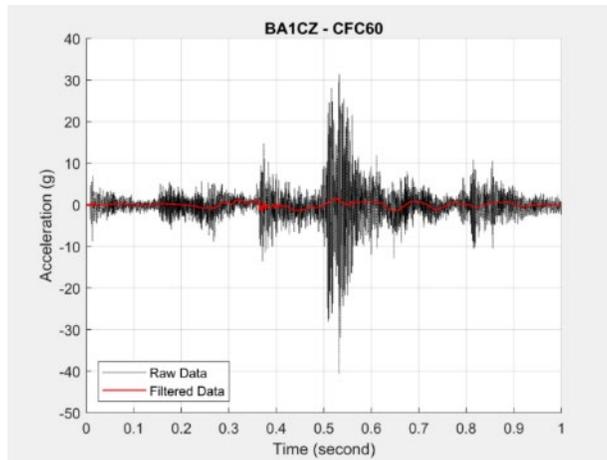
Figure B3. Raw and CFC60 Filtered Acceleration-Time Data from BA1CZ
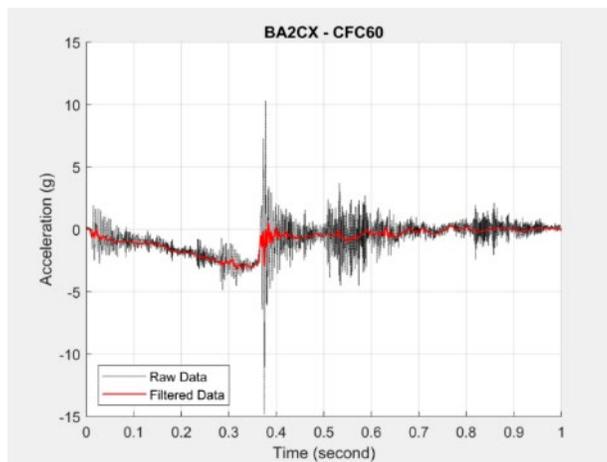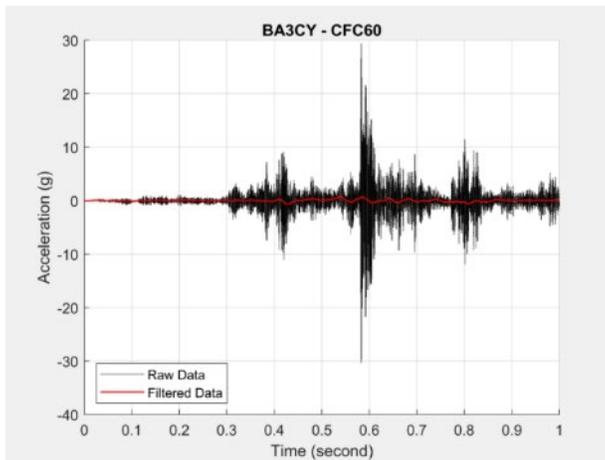

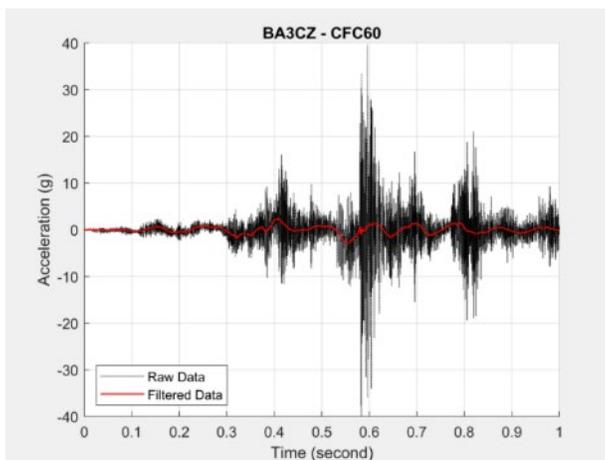**Figure B4. Raw and CFC60 Filtered Acceleration-Time Data from BA2CX**
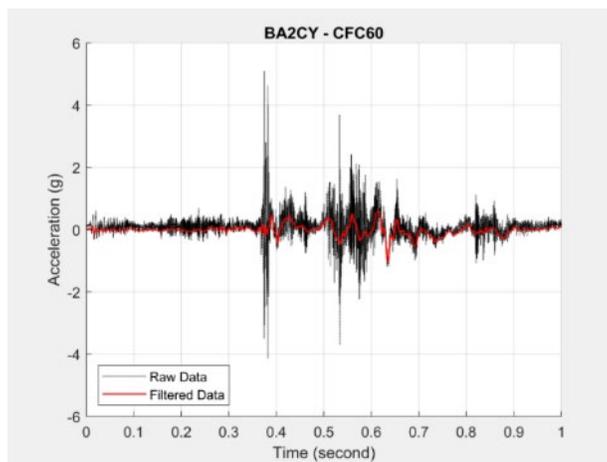
Figure B5. Raw and CFC60 Filtered Acceleration-Time Data from BA2CY
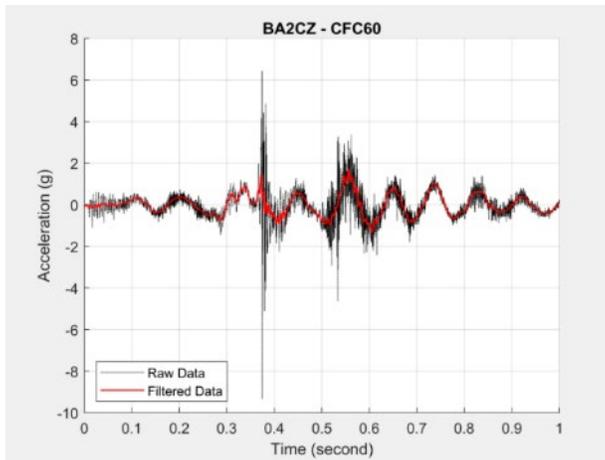
Figure B6. Raw and CFC60 Filtered Acceleration-Time Data from BA2CZ
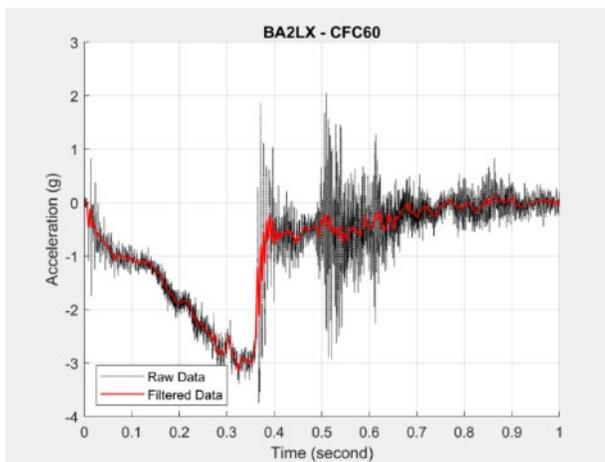
Figure B7. Raw and CFC60 Filtered Acceleration-Time Data from BA2LX
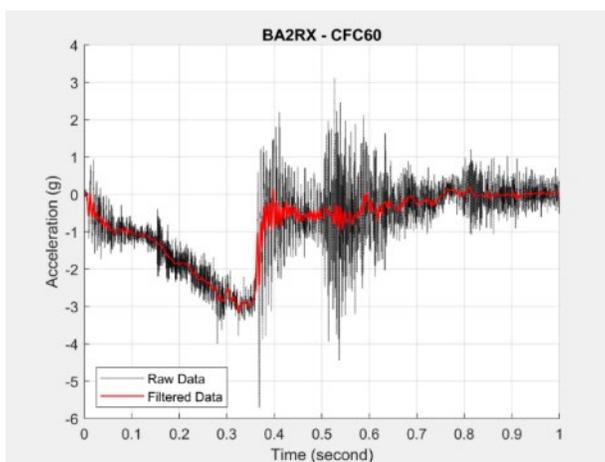
Figure B8. Raw and CFC60 Filtered Acceleration-Time Data from BA2RX
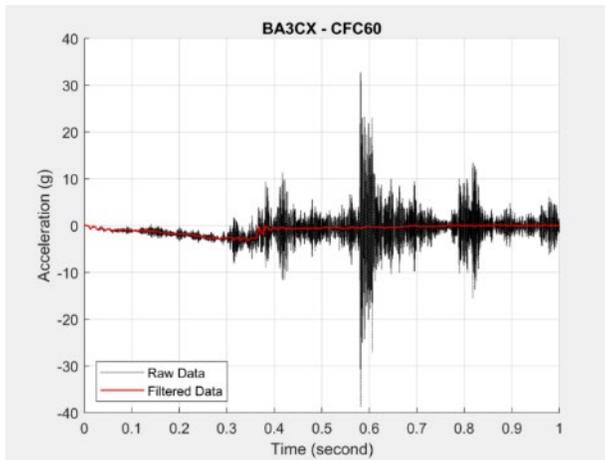
Figure B9. Raw and CFC60 Filtered Acceleration-Time Data from BA3CX

Figure B10. Raw and CFC60 Filtered Acceleration-Time Data from BA3CY

Figure B11. Raw and CFC60 Filtered Acceleration-Time Data from BA3CZ

B2 – Pressures
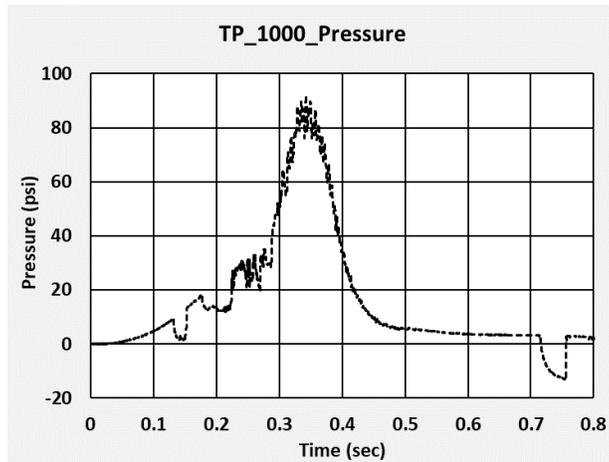
Figure B12. Raw Pressure-Time Data from TP1000
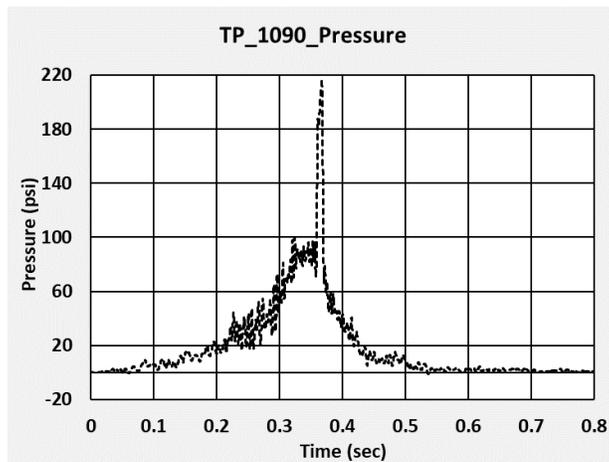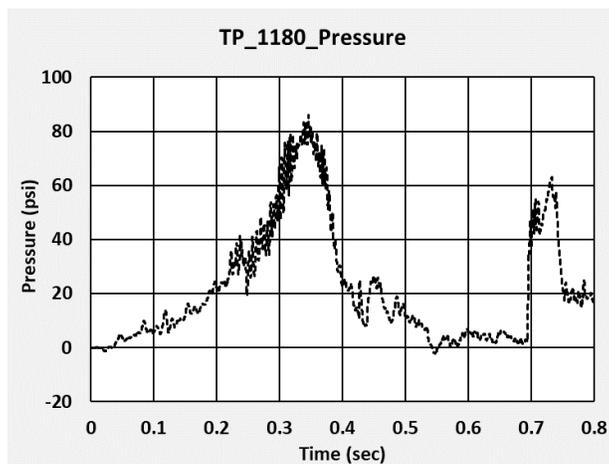

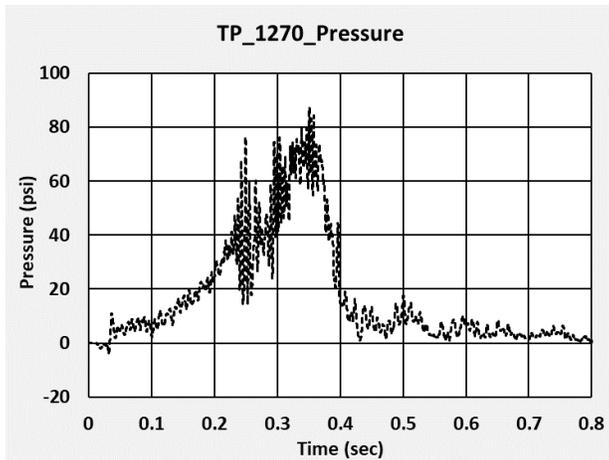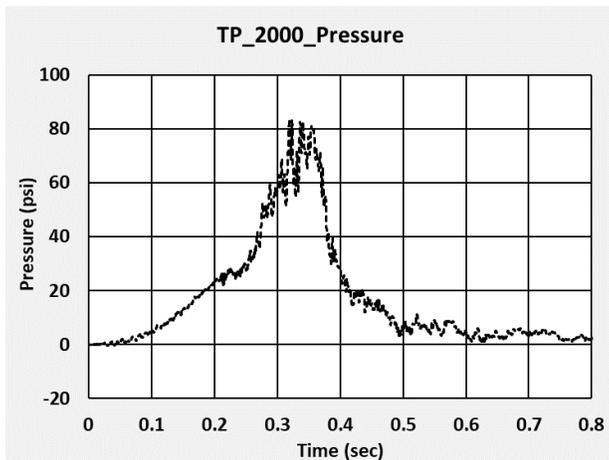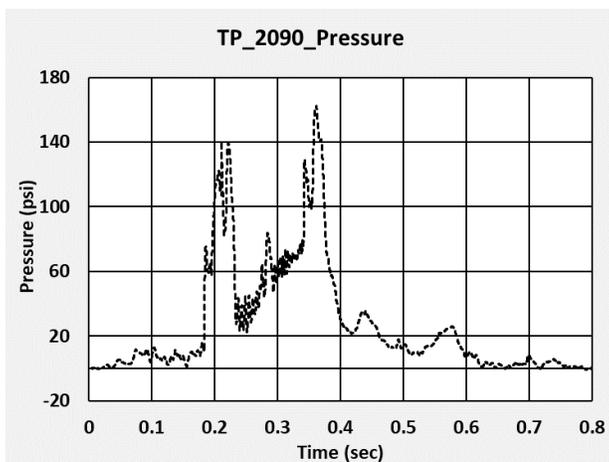**Figure B13. Raw Pressure-Time Data from TP1090**

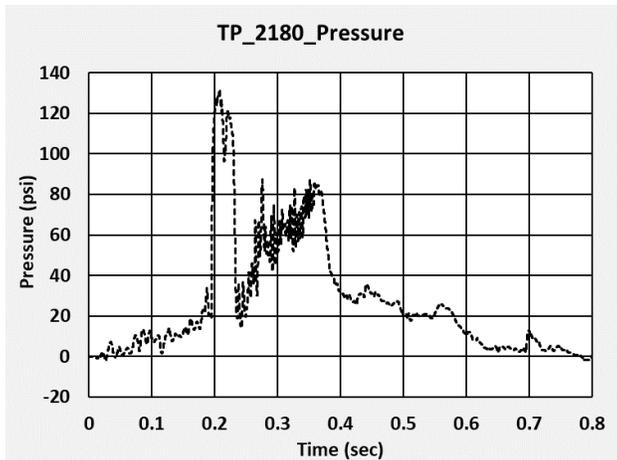**Figure B14. Raw Pressure-Time Data from TP1180**

69

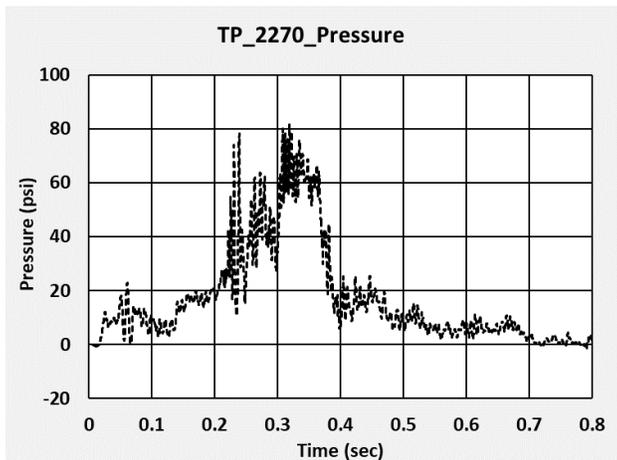**Figure B15. Raw Pressure-Time Data from TP1270**

Figure B16. Raw Pressure-Time Data from TP2000
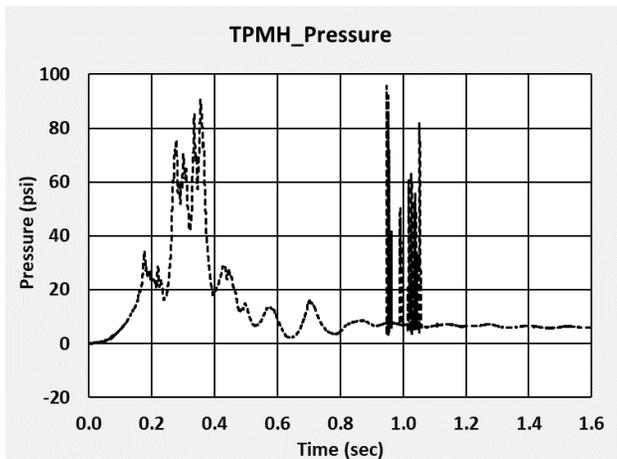

Figure B17. Raw Pressure-Time Data from TP2090

Figure B18. Raw Pressure-Time Data from TP2180

Figure B19. Raw Pressure-Time Data from TP2270

Figure B20. Raw Pressure-Time Data from TPMH

71

Figure B21. Raw Pressure-Time Data from TP3090
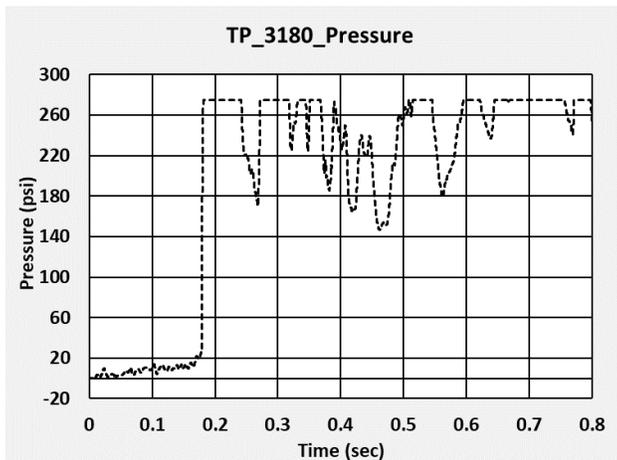
Figure B22. Raw Pressure-Time Data from TP3180
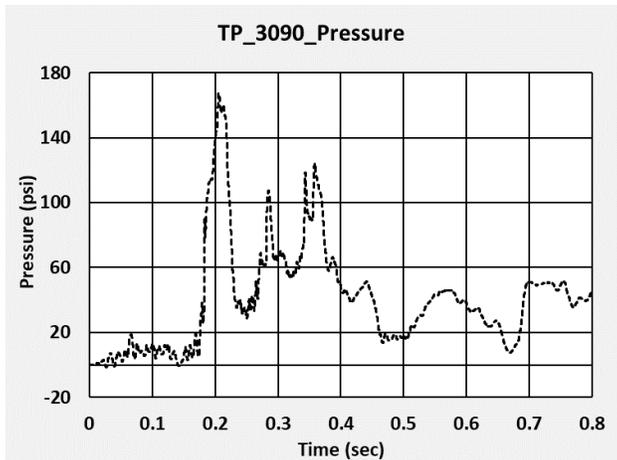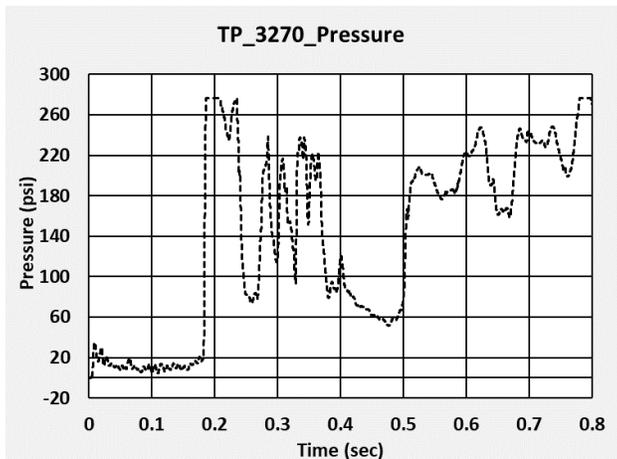

Figure B23. Raw Pressure-Time Data from TP3270

B3 – Displacements

Figure B24. Raw Displacement-Time Data from TD1Y

Figure B25. Raw Displacement-Time Data from TD2Y

Figure B26. Raw Displacement-Time Data from TD3Y

Figure B27. Raw Displacement-Time Data from TD3Z
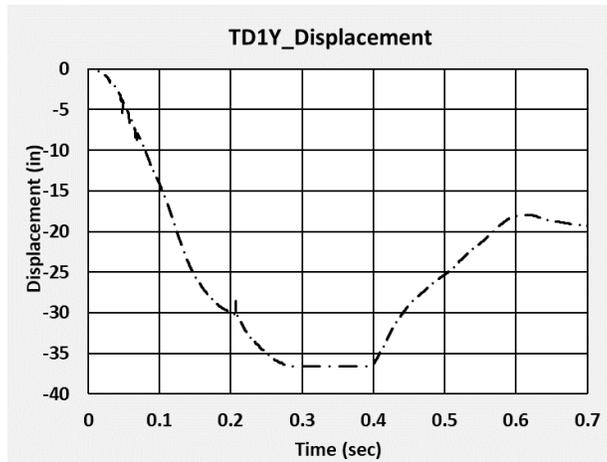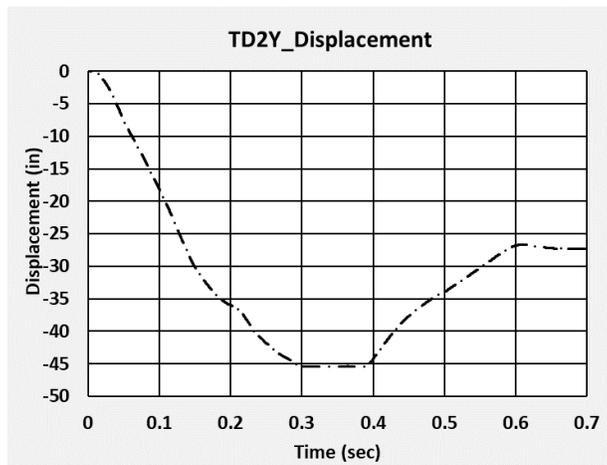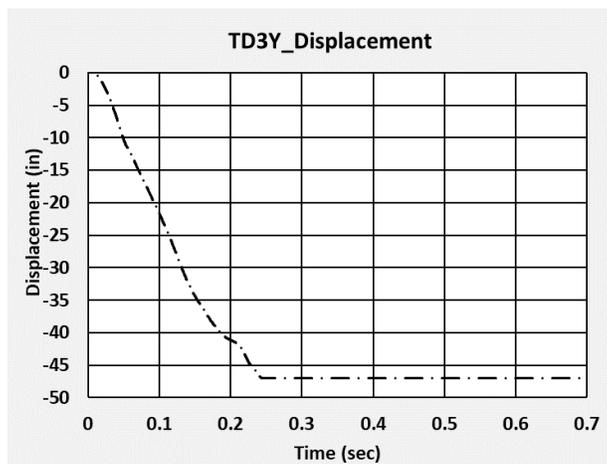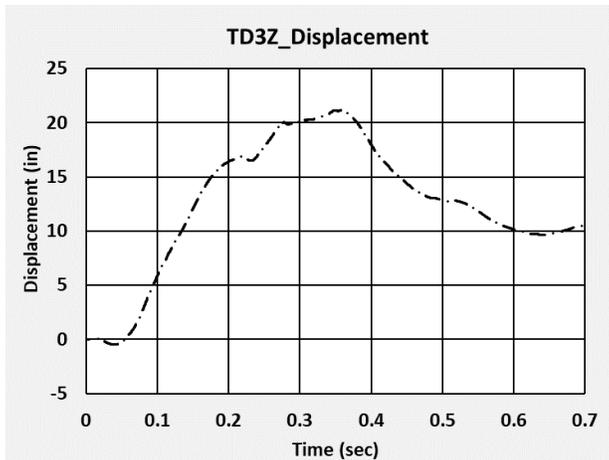

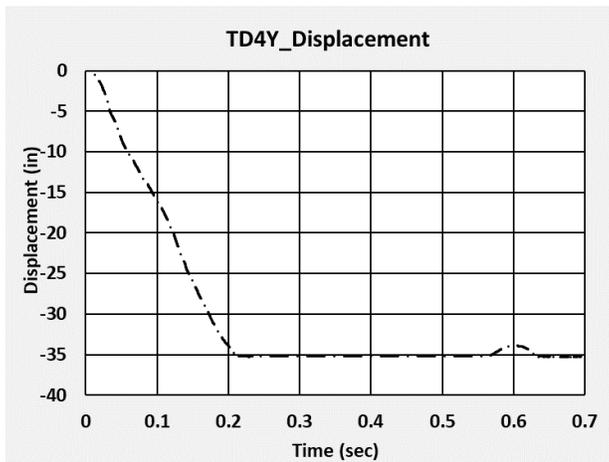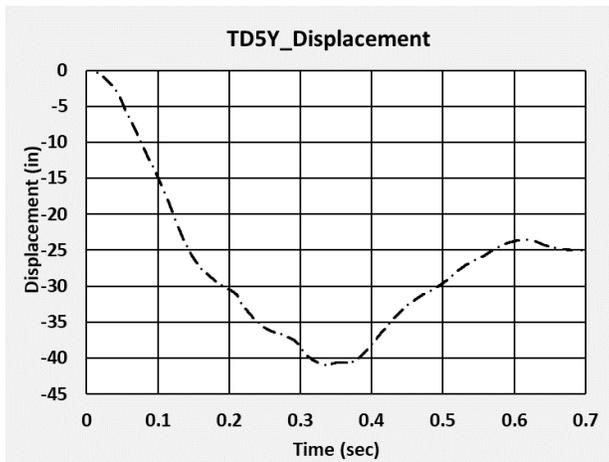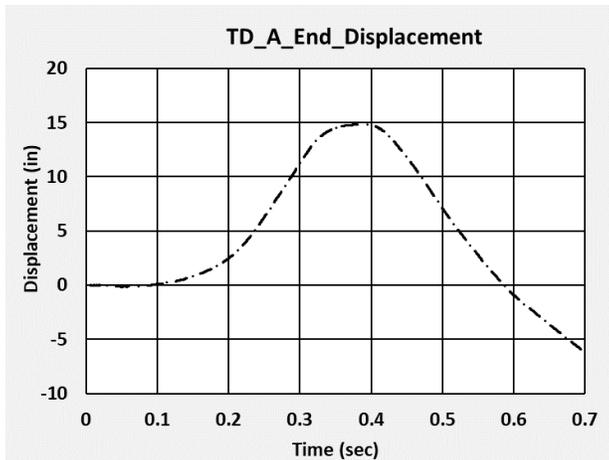**Figure B28. Raw Displacement-Time Data from TD4Y**

Figure B29. Raw Displacement-Time Data from TD5Y

Figure B30. Raw Displacement-Time Data from Displacement Transducer on A-End Head
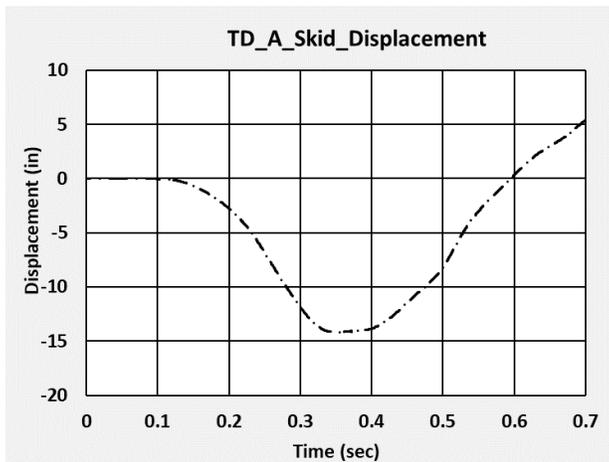
Figure B31. Raw Displacement-Time Data from Displacement Transducer on A-End Skid
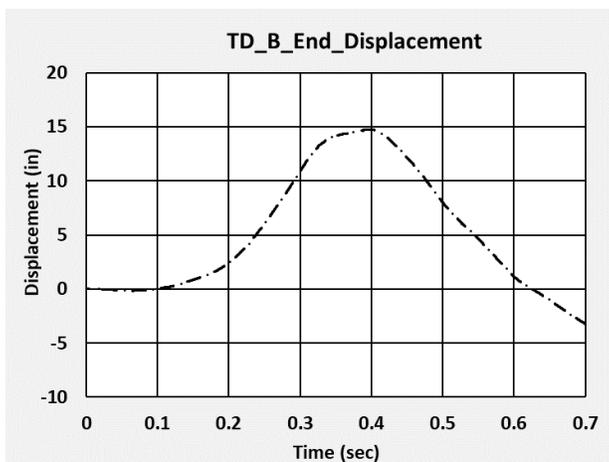
Figure B32. Raw Displacement-Time Data from Displacement Transducer on B-End Head

75
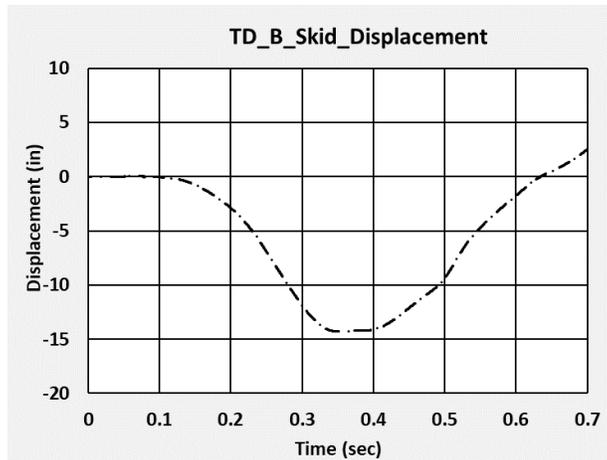
Figure B33. Raw Displacement-Time Data from Displacement Transducer on B-End Skid

B4 – Material Characterization Results

TENSILE RESULTS: ASTM E8-16a
SPEED OF TESTING: 0.005 in./in./min., Extensometer travel exceeded - Test continued at last stroke rate
MATERIAL: TC 128 Gr. B   DISPOSITION: Report

SID	TestLog Number	Temp.	UTS ksi	0.2% YS ksi	Elong %	RA %	Modulus Msi	Ult. Load lbf	0.2% YLD. lbf	Orig. Dia. (in.)	Final Dia. (in.)	4D Orig GL (in.)	4D Final GL (in.)	Orig. Area (sq. in.)	Machine Number	A\U\R
Tank Car 9-1	890HHH	Room	87.0	61.1	31	68	33.4	8499	5974	0.3527	0.1992	1.40	1.84	0.09770140	M10	R
Tank Car 9-2	891HHH	Room	86.9	61.4	31	68	40.5	8495	5995	0.3527	0.2004	1.40	1.83	0.09770140	M10	R
Tank Car 9-3	892HHH	Room	86.7	60.9	29	67	34.6	8461	5944	0.3524	0.2010	1.40	1.81	0.09753527	M10	R

A\U\R: A=ACCEPTABLE, U=UNACCEPTABLE, R=REPORT

Figure B34. Summary of Tensile Testing Results for Actual TC128 Steel
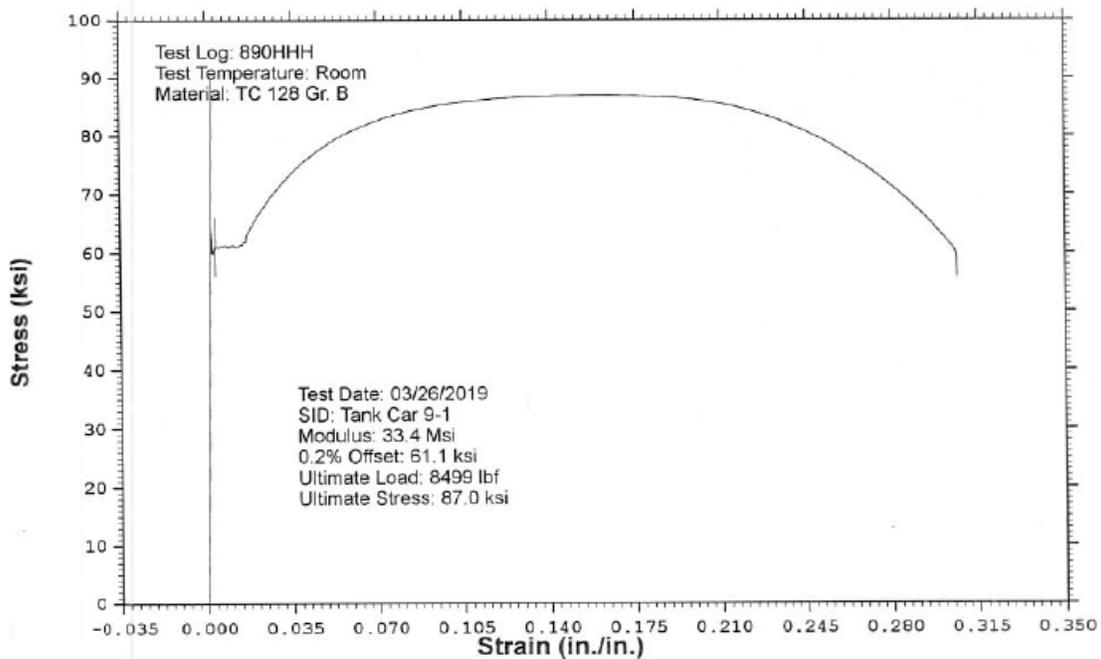
Figure B35. Engineering Stress-Strain Response for TC128 Sample 890HHH

76
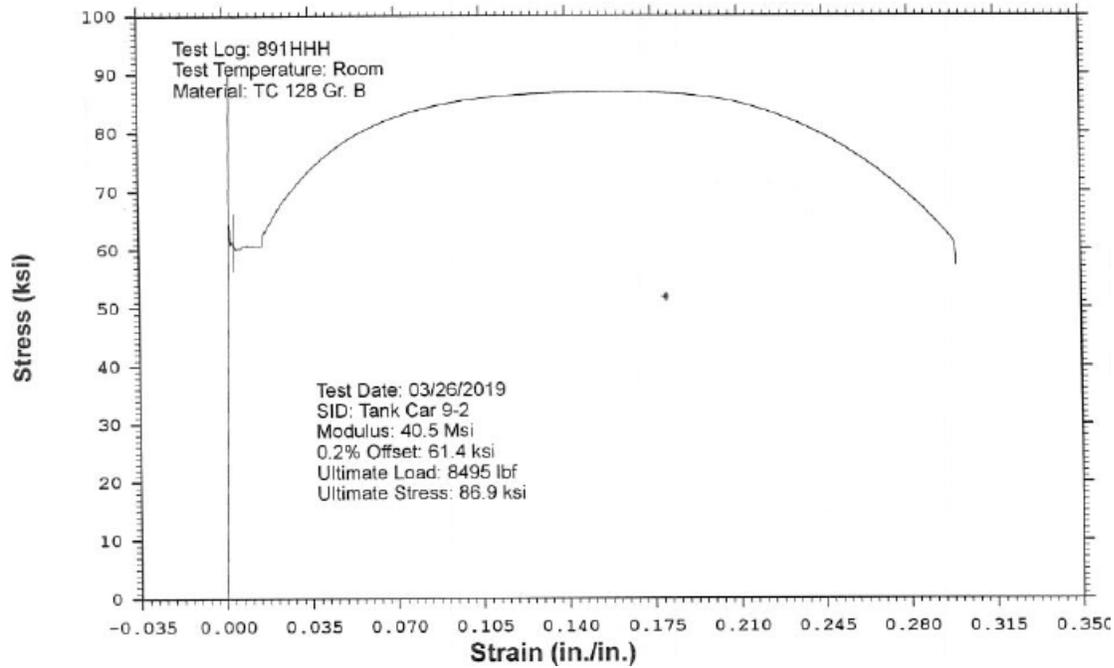
Figure B36. Engineering Stress-Strain Response for TC128 Sample 891HHH
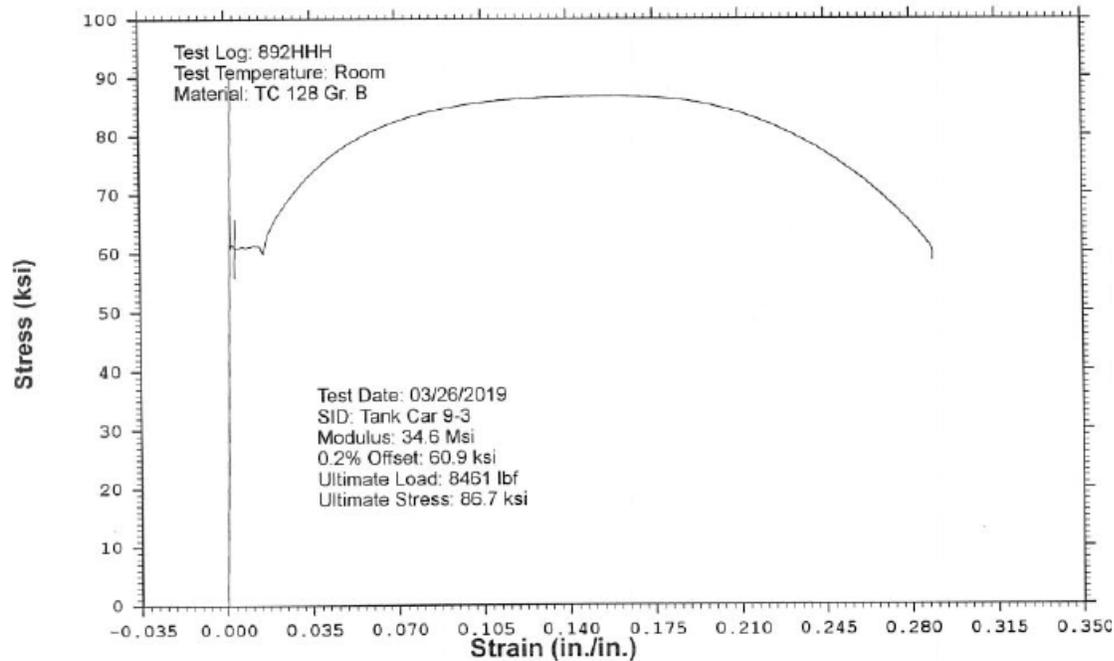
Figure B37. Engineering Stress-Strain Response for TC128 Sample 892HHH

Appendix C.
Finite Element Analysis and Test Results

For all test results presented in this appendix, the time has been offset by 0.005 seconds to account for the test instrumentation triggering when the ram surface was still approximately 1 inch away from contacting with the tank.

C1 – Pre-Test Puncture FEA and Test Results

The pre-test FE models with lower and upper estimates of TC128 steel run at 14 mph experienced puncture, and the test which ran at 13.9 mph also experienced puncture. The pre-test FE model results presented in the following series of plots end at approximately 0.26 and 0.33 seconds of simulation time for the lower and upper estimates, respectively, as that is when each model terminated. The test results are presented from 0 to 0.5 seconds with a 0.005-second offset to account for the time lag or approximate 1-inch gap between the trigger mechanism and the point where the impactor contacted the tank.
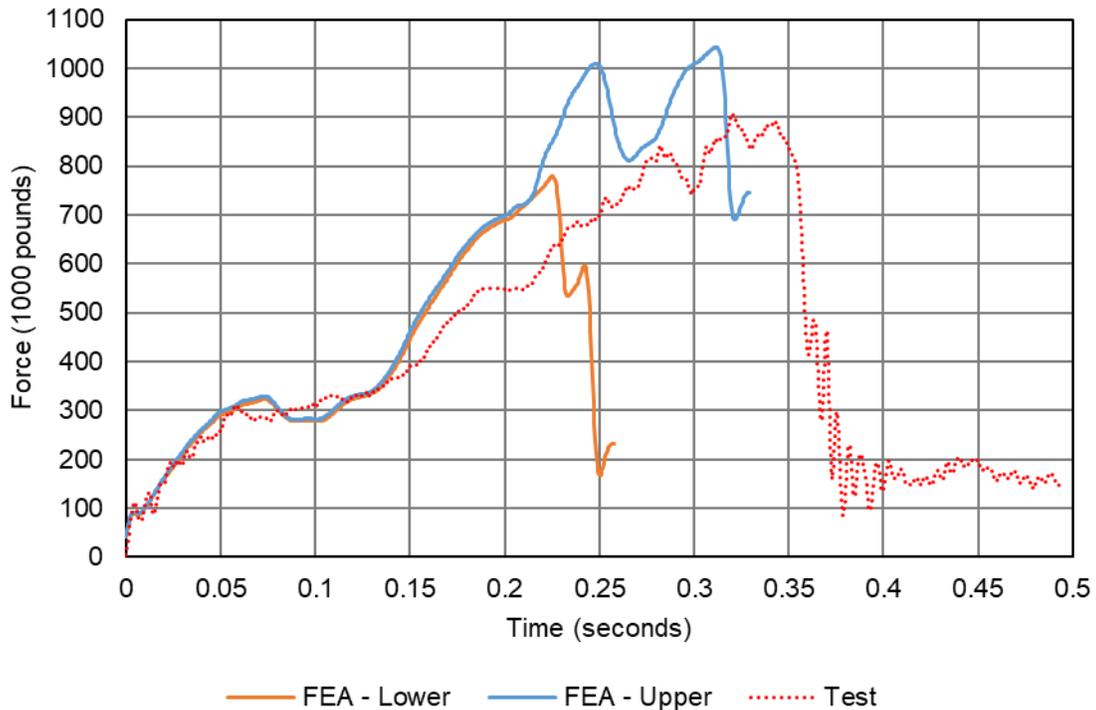
Figure C1. Impact Force vs. Time, Pre-Test FEA with Lower and Upper Estimates of TC128 Steel and Test Measurement Data
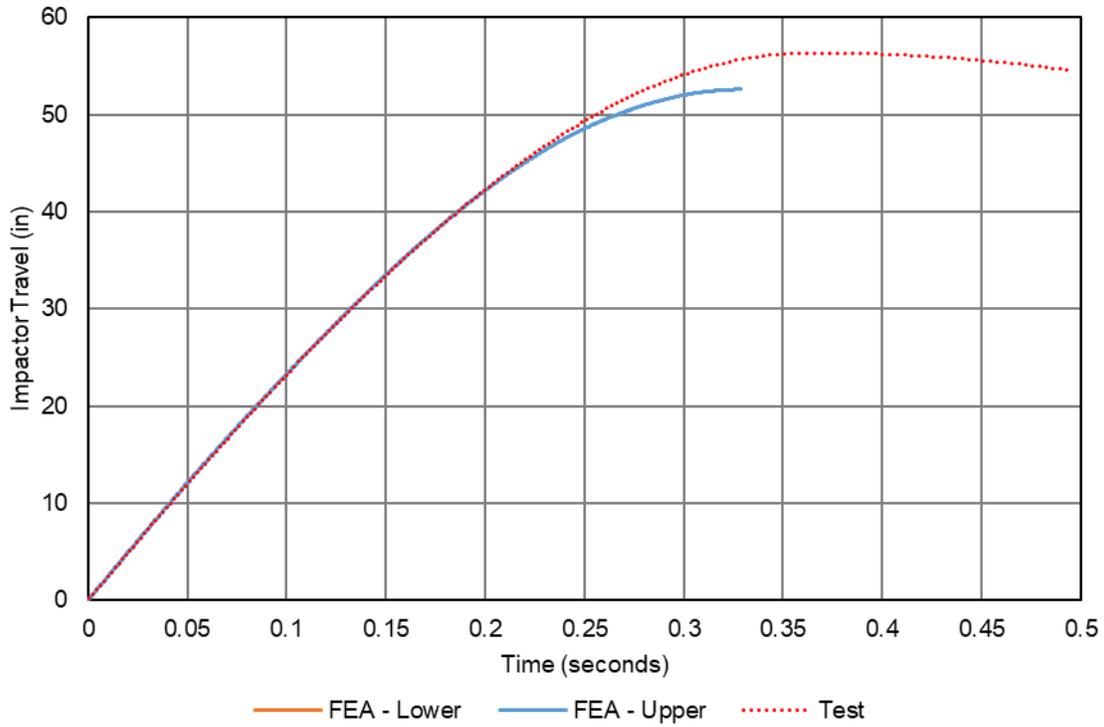
Figure C2. Impactor Travel vs. Time, Pre-Test FEA with Lower and Upper Estimates of TC128 Steel and Test Measurement Data
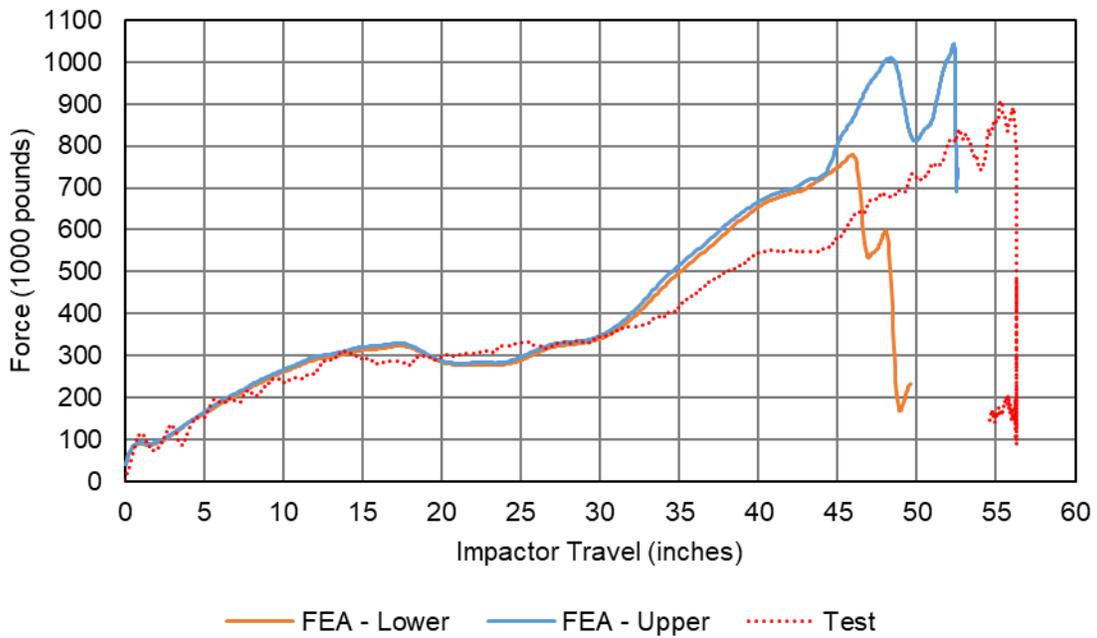
Figure C3. Impact Force vs. Impactor Travel, Pre-Test FEA with Lower and Upper Estimates of TC128 Steel and Test Measurement Data
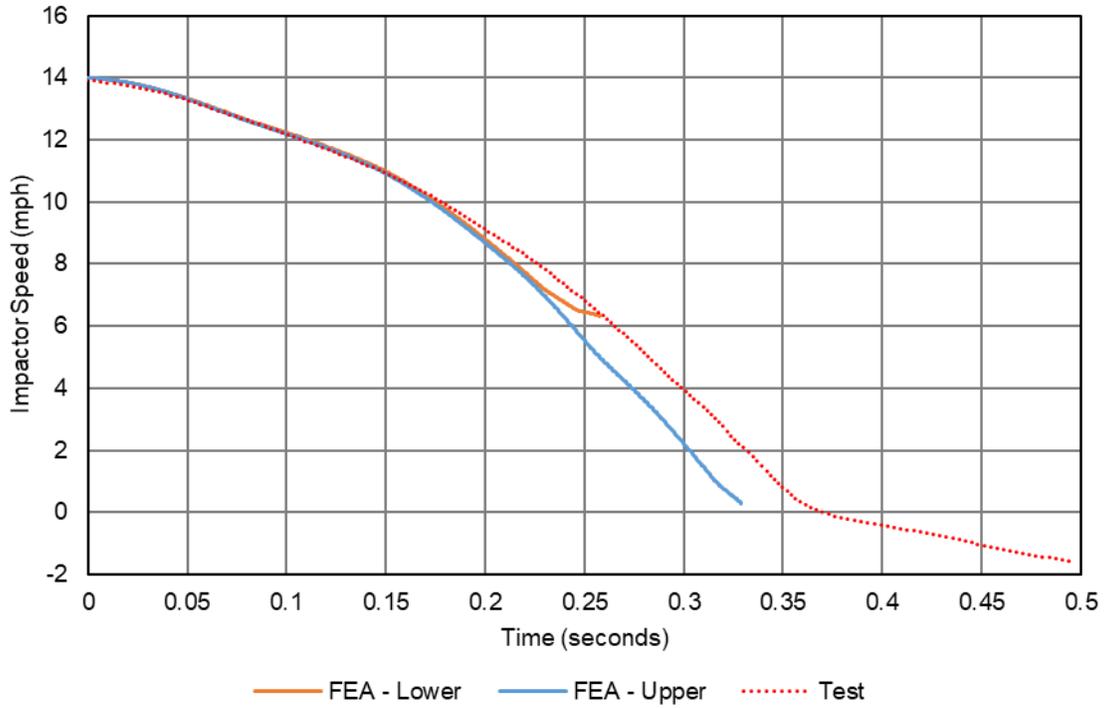
Figure C4. Impact Speed vs. Time, Pre-Test FEA with Lower and Upper Estimates of TC128 Steel and Test Measurement Data
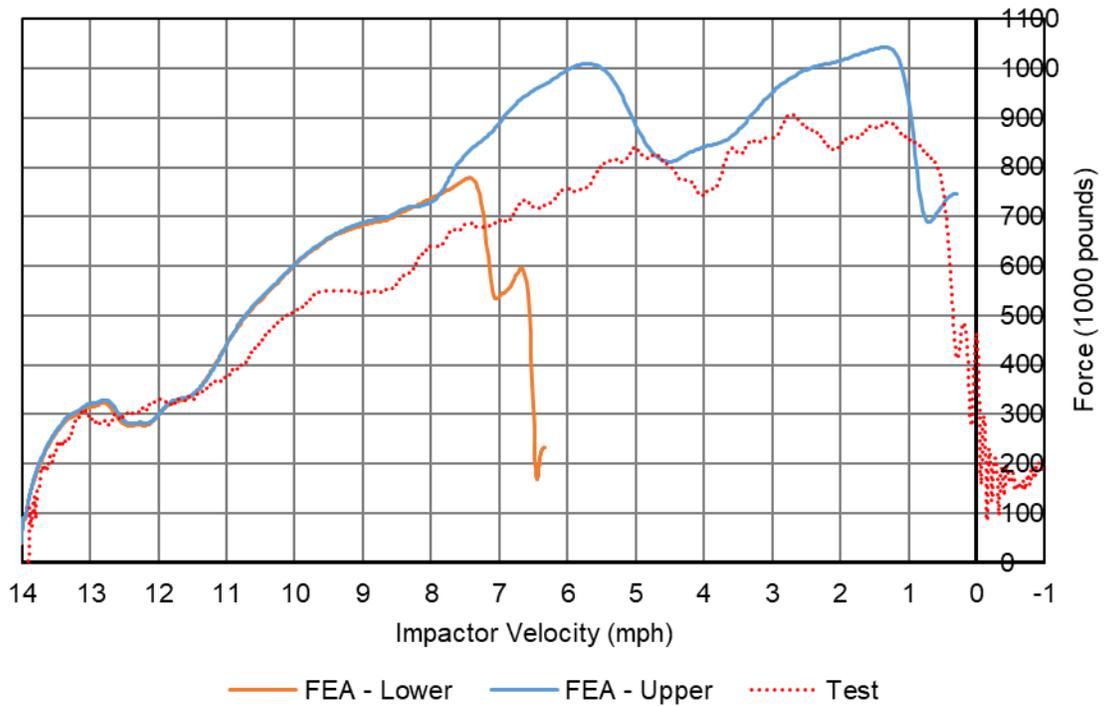
Figure C5. Impact Force vs. Velocity, Pre-Test FEA with Lower and Upper Estimates of TC128 Steel and Test Measurement Data

Figure C6. Average Air Pressure vs. time, Pre-Test FEA with Lower and Upper Estimates of TC128 Steel and Test Measurement Data
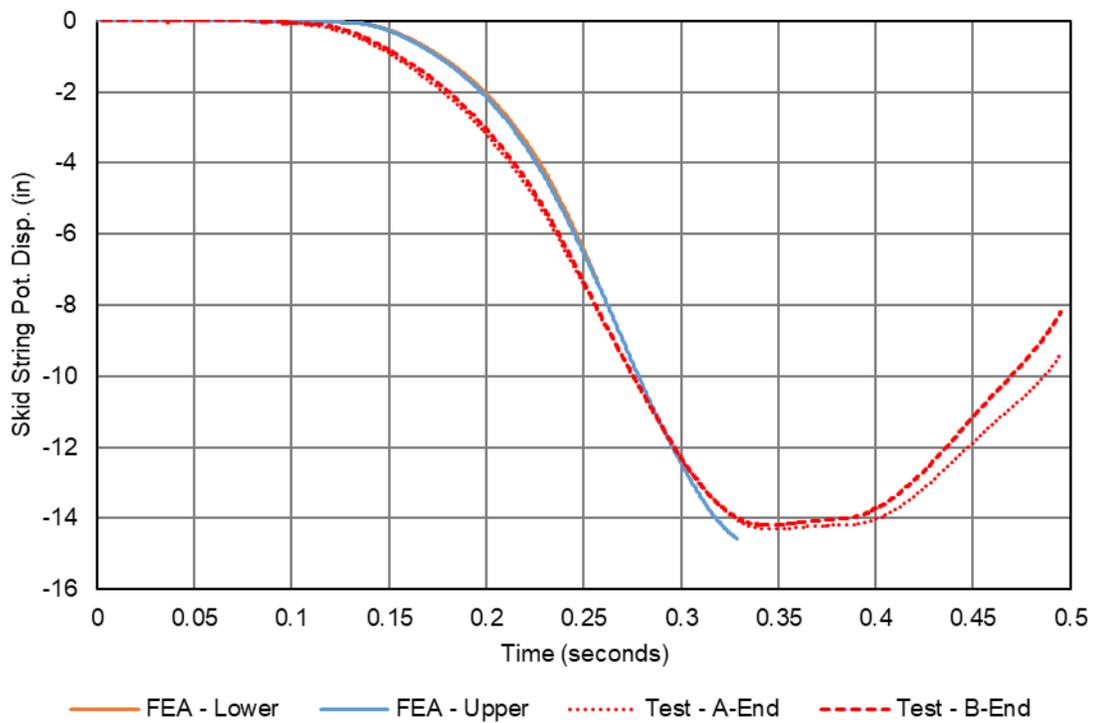
Figure C7. String Potentiometers at Skids, Pre-Test FEA with Lower and Upper Estimates of TC128 Steel and Test Measurement Data
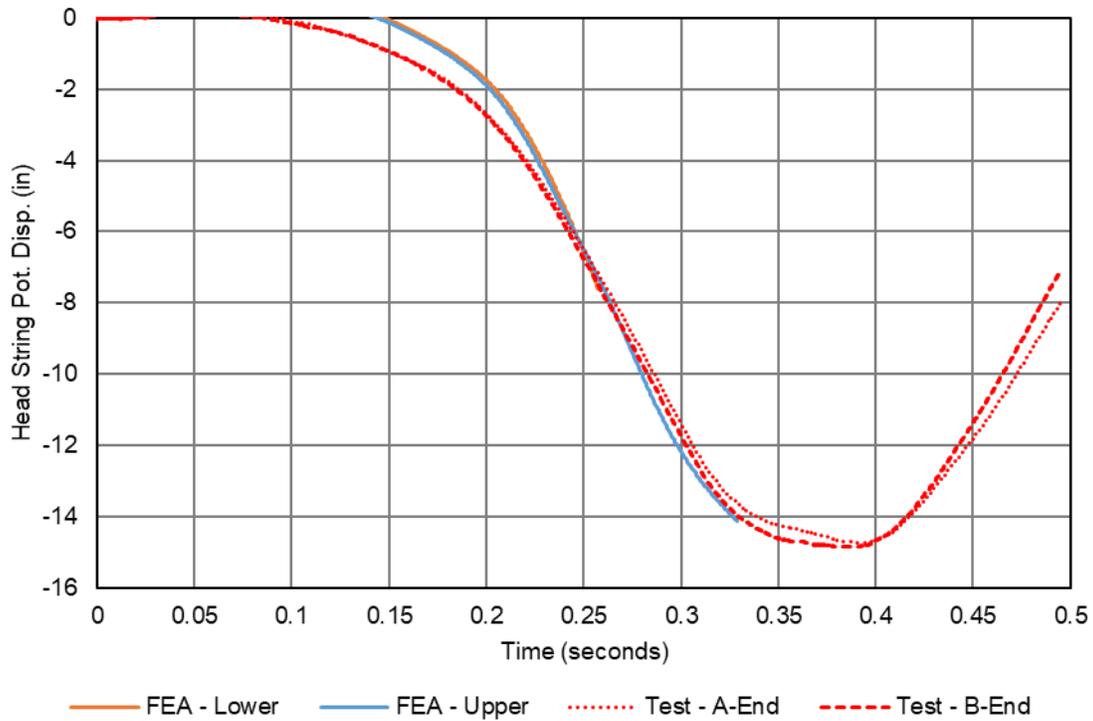
Figure C8. String Potentiometers at Heads, Pre-Test FEA with Lower and Upper Estimates of TC128 Steel and Test Measurement Data
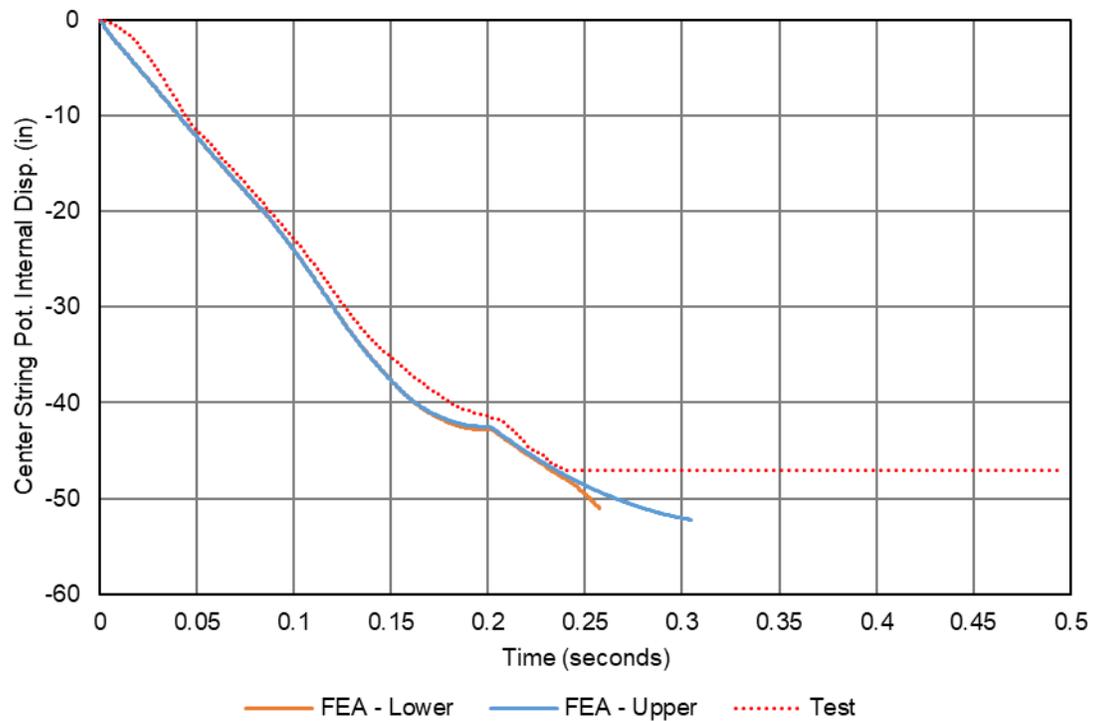
Figure C9. Internal String Potentiometer at Center of Tank, Pre-Test FEA with Lower and Upper Estimates of TC128 Steel and Test Measurement Data
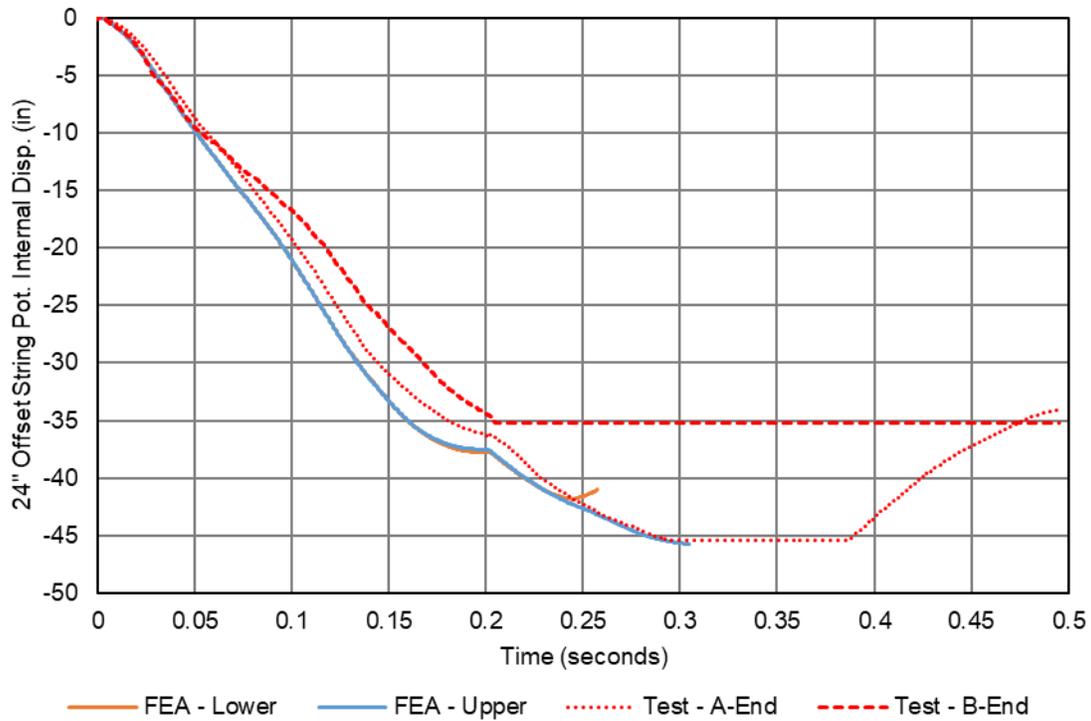
Figure C10. Internal String Potentiometers 24 inches from Impact, Pre-Test FEA with Lower and Upper Estimates of TC128 Steel and Test Measurement Data
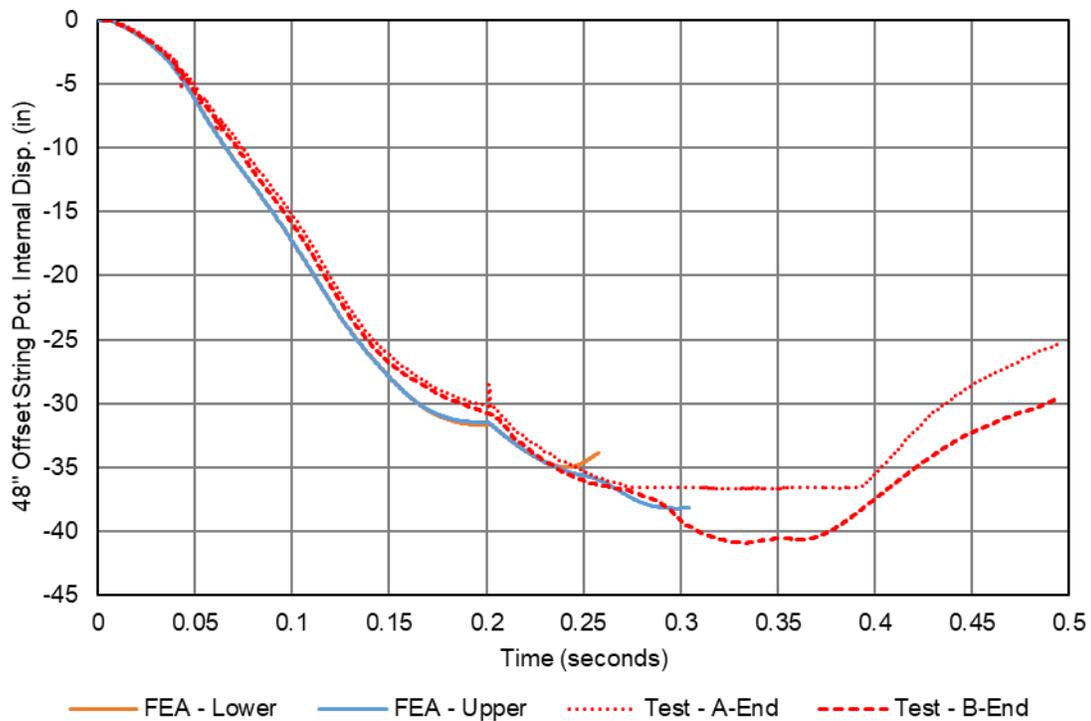
Figure C11. Internal String Potentiometers 48 inches from Impact, Pre-Test FEA with Lower and Upper Estimates of TC128 Steel and Test Measurement Data
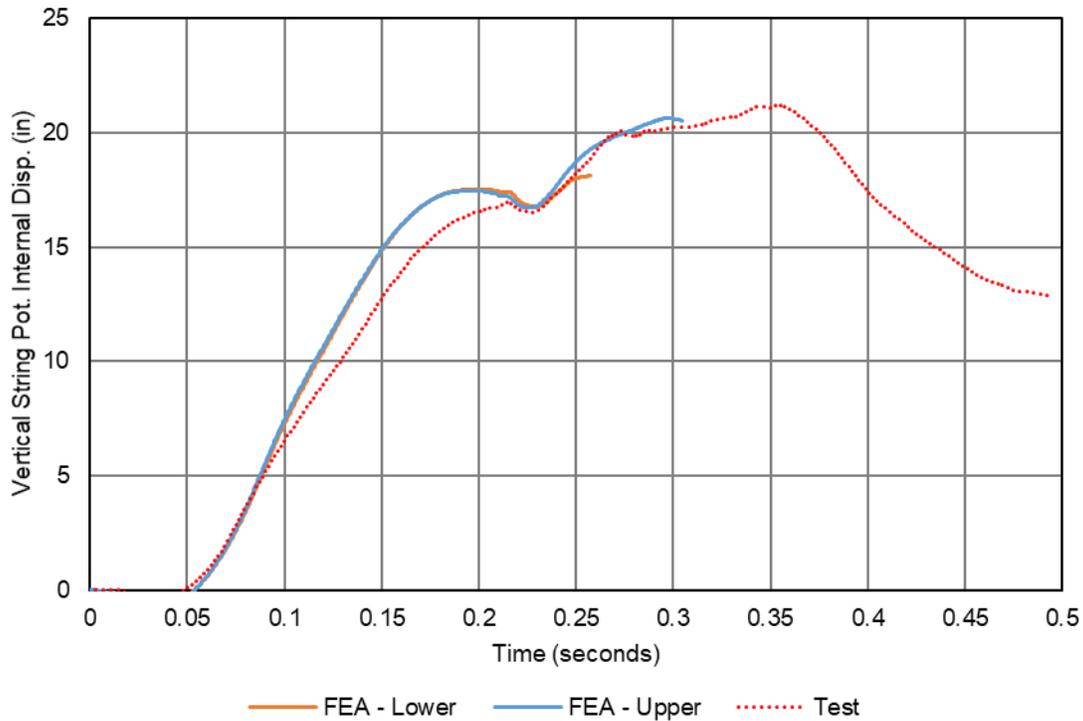
Figure C12. Internal Vertical String Potentiometer, Pre-Test FEA with Lower and Upper Estimates of TC128 Steel and Test Measurement Data

C2 – Post-Test Puncture FEA and Test Results—13.9 mph

Post-test FEA was run at the test speed determined from the speed traps, 13.9 mph. The post-test FE models were also run using updated material behaviors for the tank. Two bounding cases were considered for the post-test model: 1) a "sealed" tank where air could only pass through the pressure relief valve (PRV) if the start-to-discharge pressure was reached; and 2) an "open" tank that maintained atmospheric pressure within the outage (i.e., no pneumatic cavity). The changes implemented in the post-test model are discussed further in Section 5.4 of this report. The post-test simulations with the sealed tank terminated after 0.27 seconds and with the open tank terminated after 0.31 second due to solid element distortion in a few elements which were involved in shell-to-solid coupling; however, in both cases termination occurred after puncture occurred.

Results derived from accelerometers or pressure transducers have been filtered using a CFC60 filter. While the test results were time-shifted by 0.005 seconds for comparison with the pre-test FEA results, the impactor in the post-test models was moved approximately 1-inch away from the tank to account for the gap in the triggering mechanism, and the test data was not time-shifted.
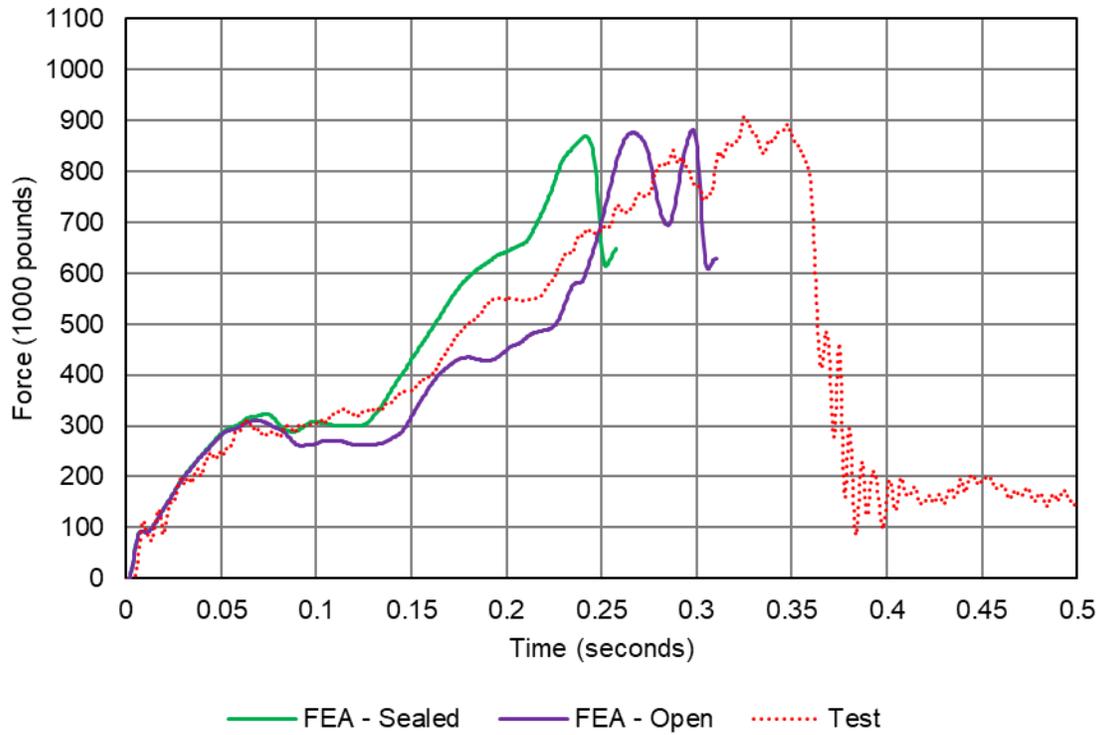
Figure C13. Impact Force vs. Time, Post-Test FEA with Sealed and Open Tank and Test Measurement Data
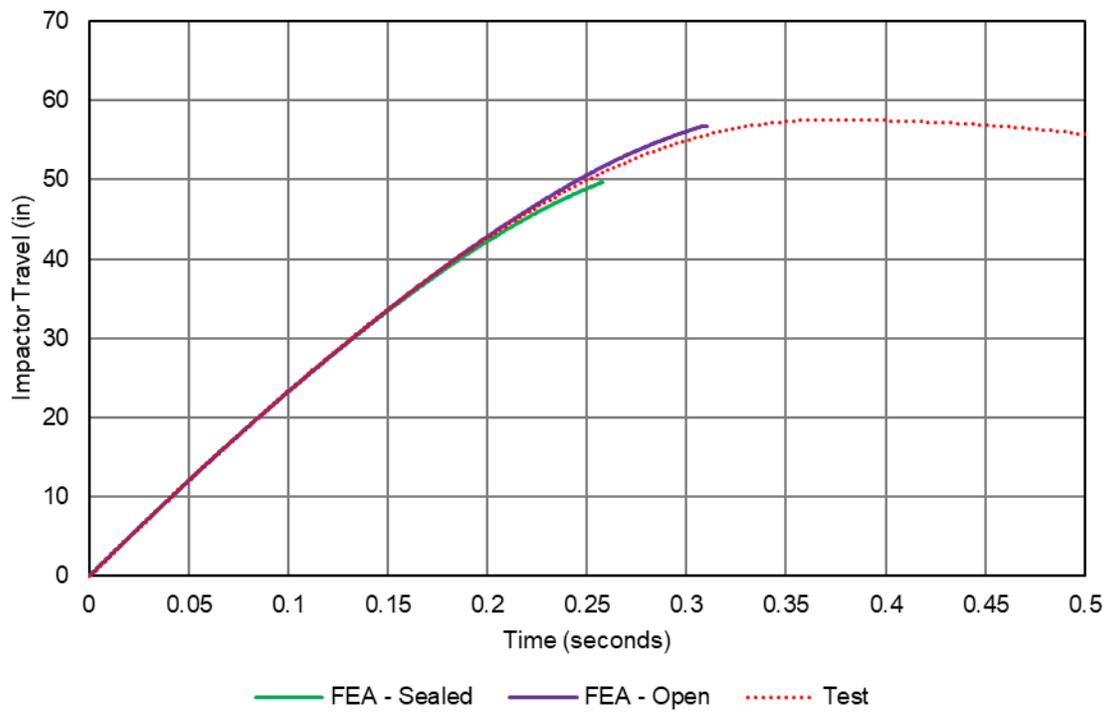
Figure C14. Impactor Travel vs. Time, Post-Test FEA with Sealed and Open Tank and Test Measurement Data

85
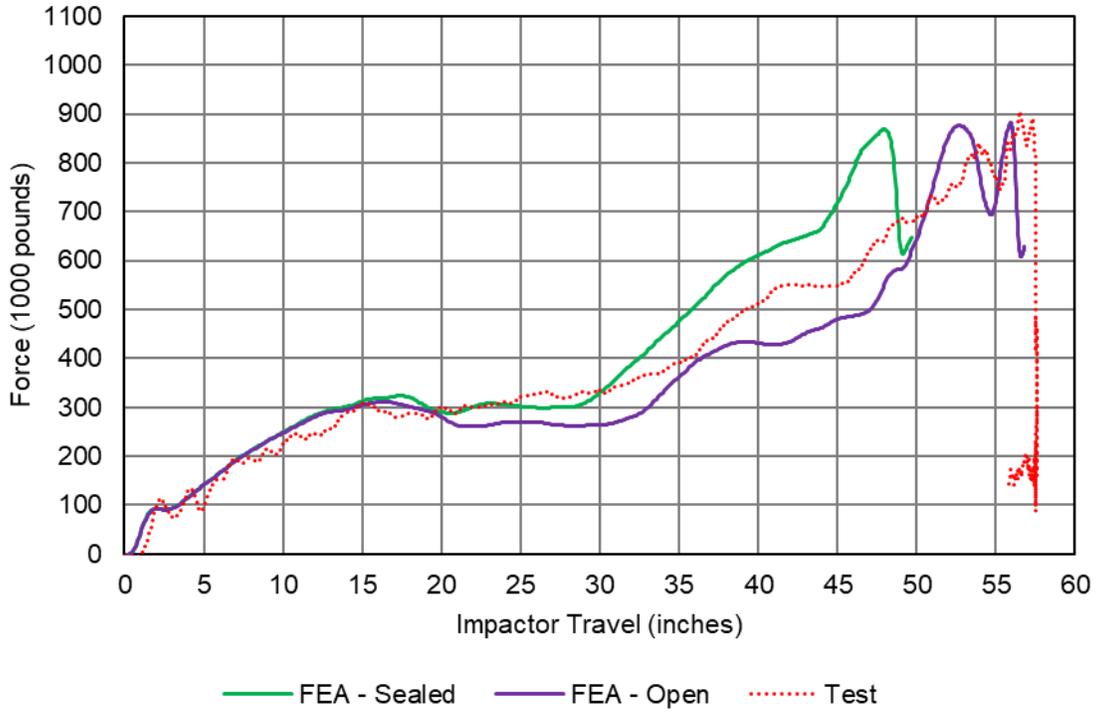
Figure C15. Impact Force vs. Impactor Travel, Post-Test FEA with Sealed and Open Tank and Test Measurement Data
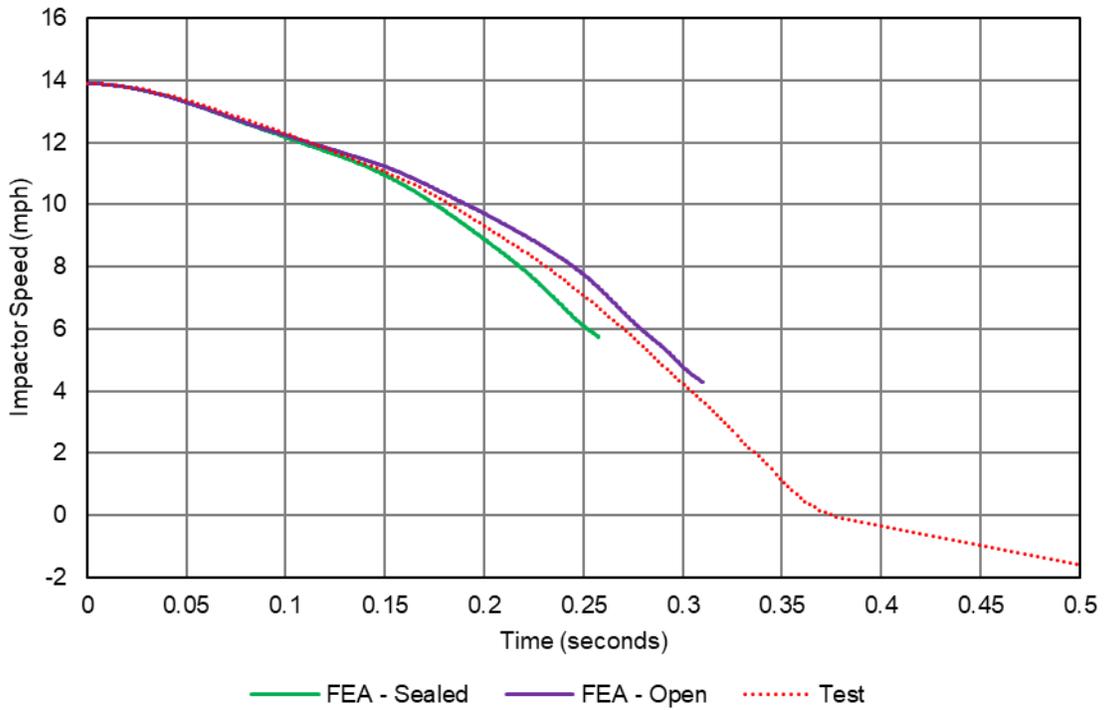
Figure C16. Impactor Speed vs. Time, Post-Test FEA with Sealed and Open Tank and Test Measurement Data
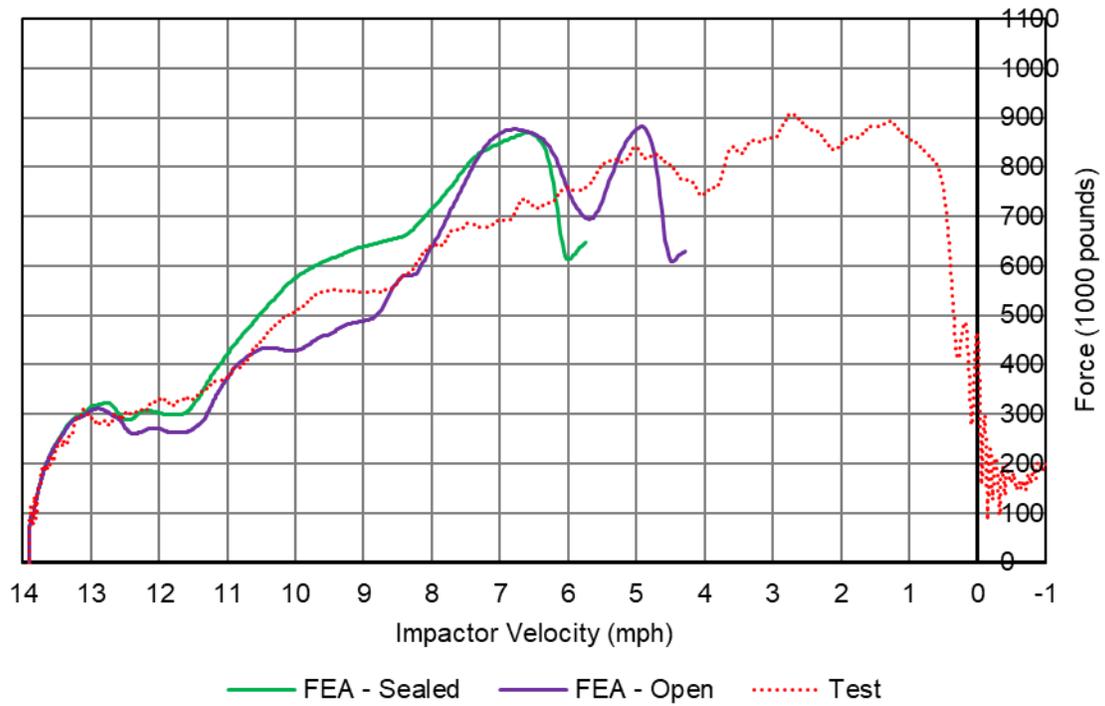
Figure C17. Impact Force vs. Velocity, Post-Test FEA with Lower and Upper Estimates of TC128 Steel and Test Measurement Data
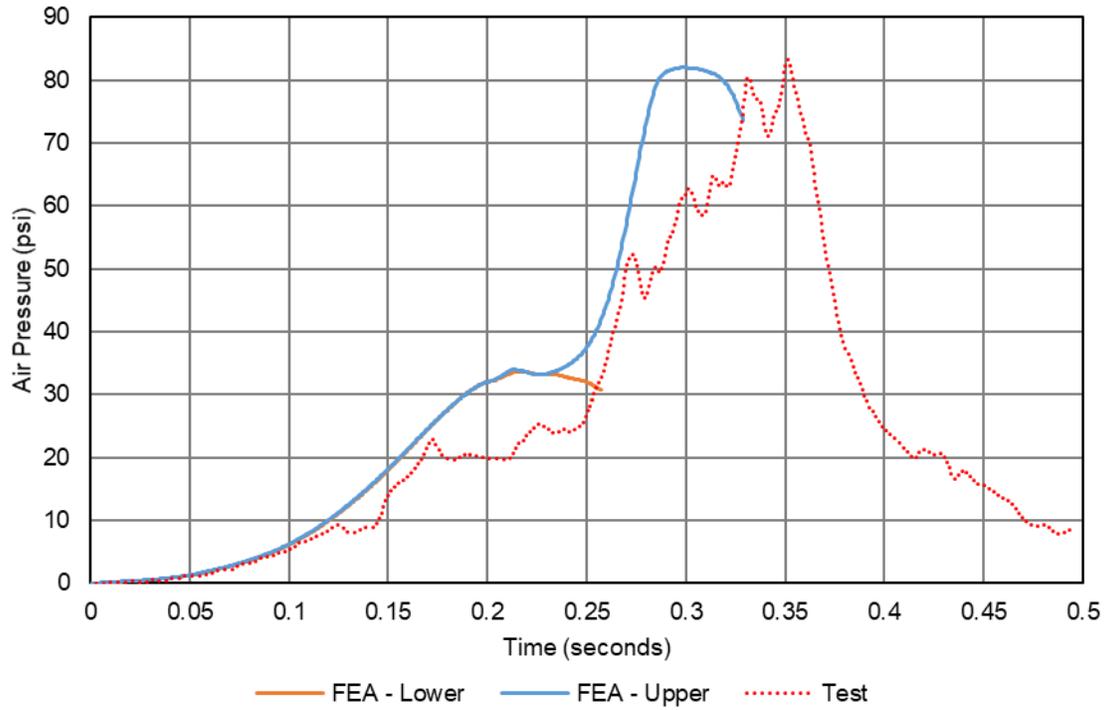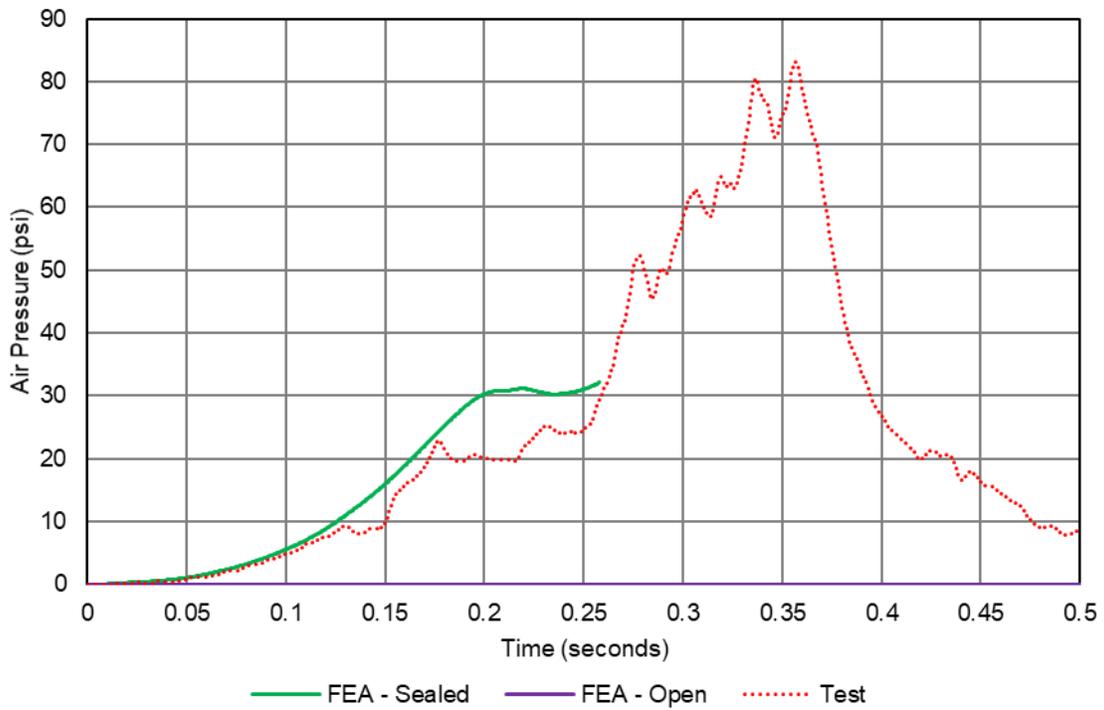

Figure C18. Average Air Pressure vs. time, Post-Test FEA with Sealed and Open Tank and Test Measurement Data
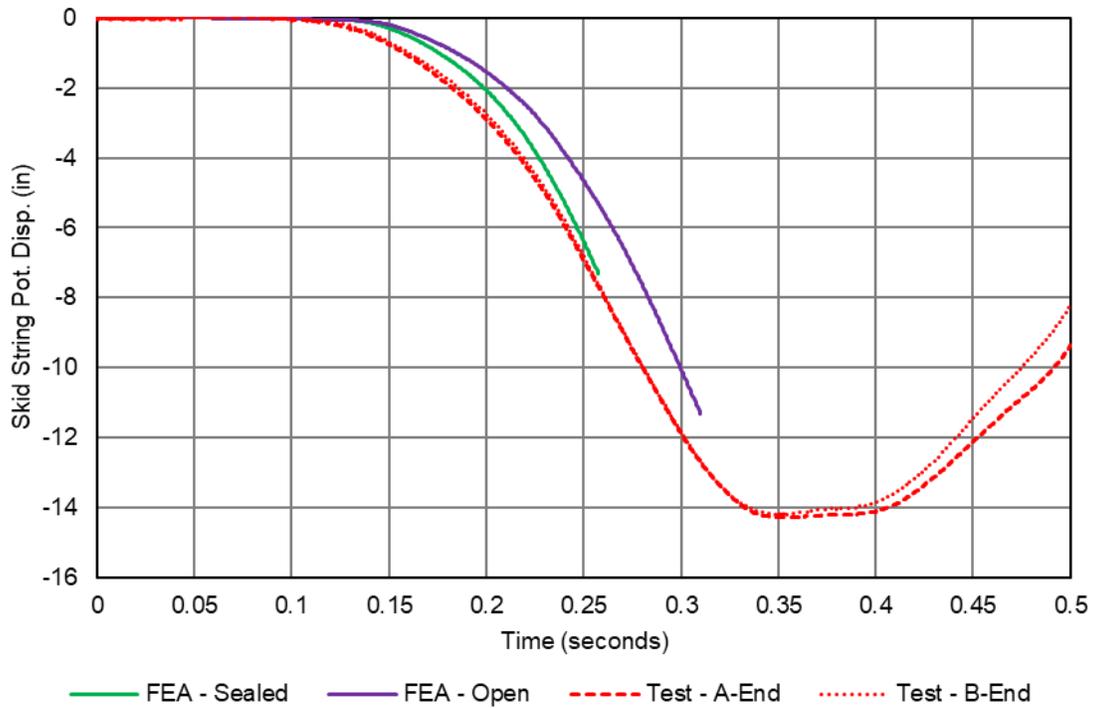
Figure C19. String Potentiometers at Skids, Post-Test FEA with Sealed and Open Tank and Test Measurement Data
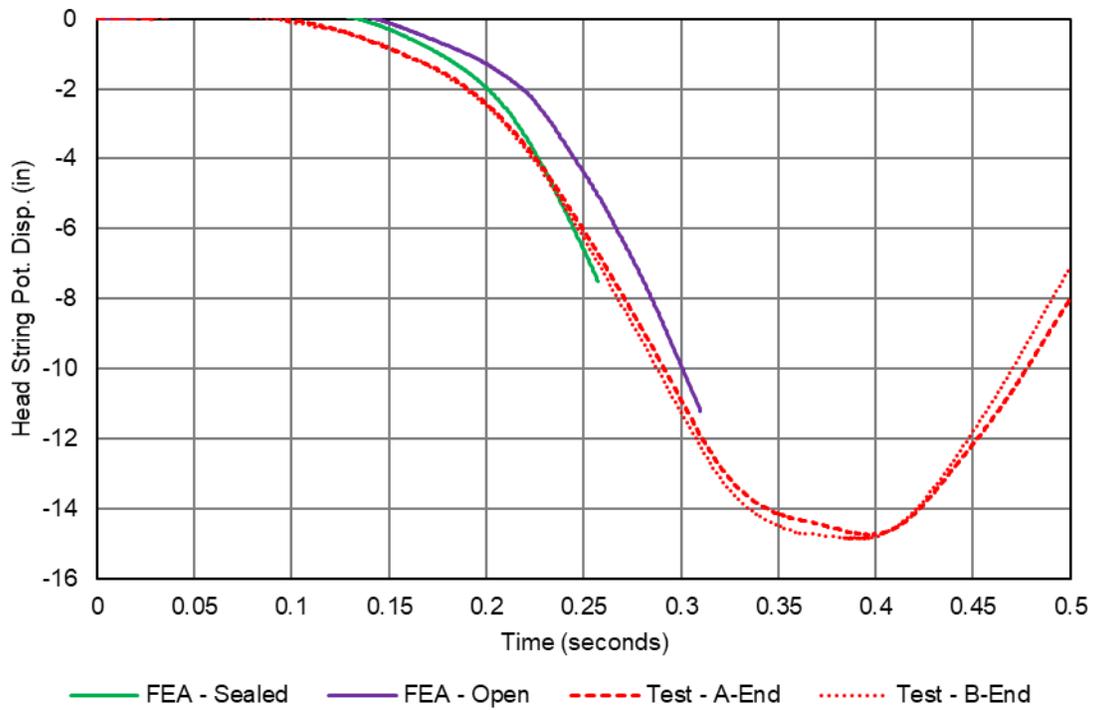
Figure C20. String Potentiometers at Heads, Post-Test FEA with Sealed and Open Tank and Test Measurement Data
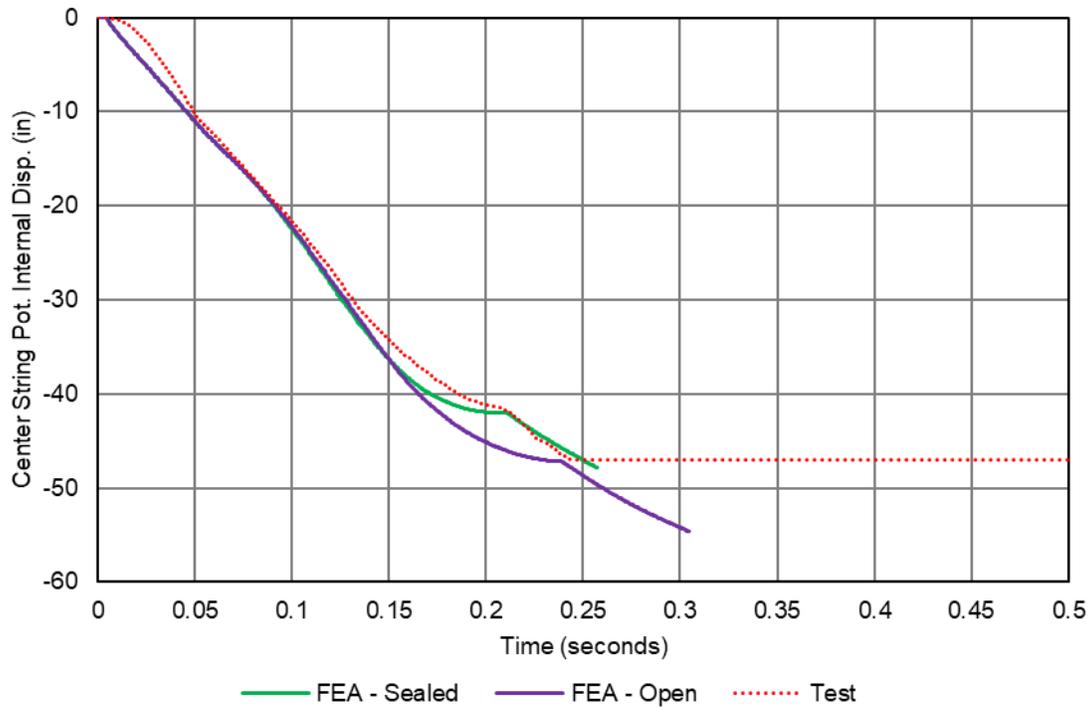
Figure C21. Internal String Potentiometer at Center of Tank, Post-Test FEA with Sealed and Open Tank and Test Measurement Data
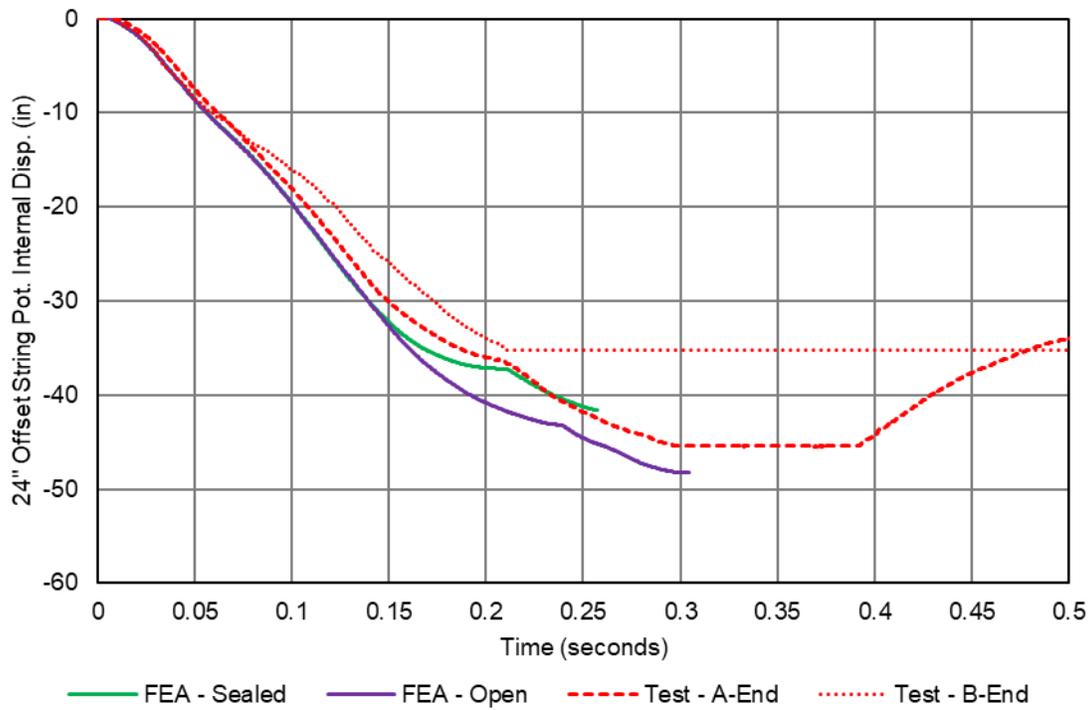
Figure C22. Internal String Potentiometers 24 inches from Impact, Post-Test FEA with Sealed and Open Tank and Test Measurement Data

89
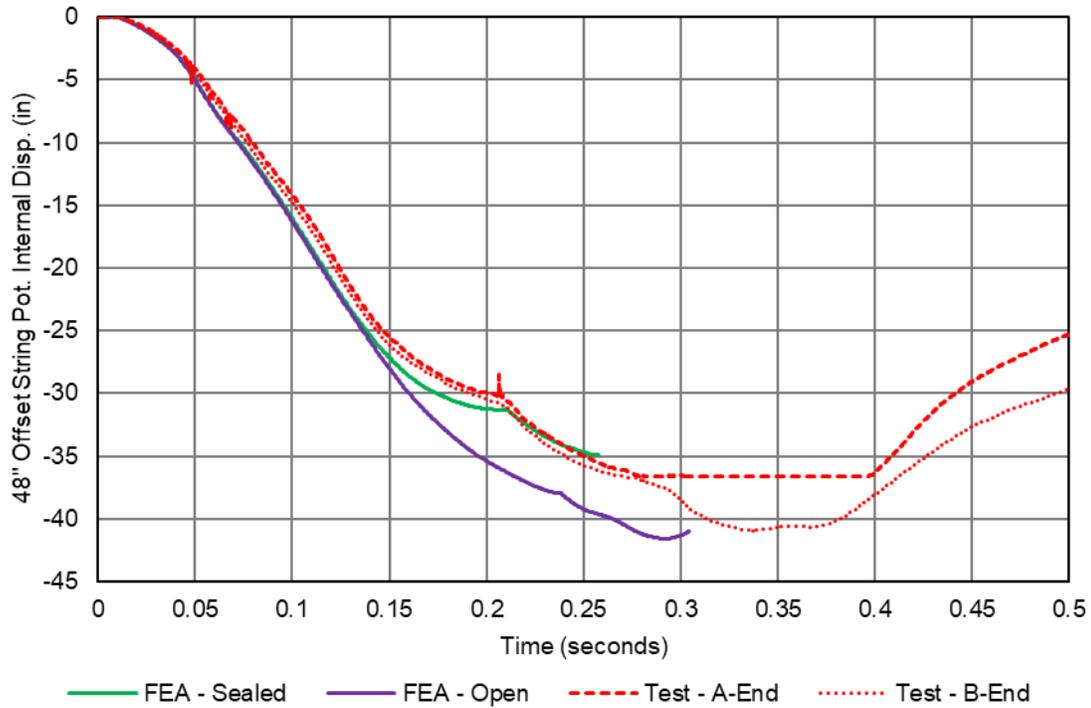
Figure C23. Internal String Potentiometers 48 inches from Impact, Post-Test FEA with Sealed and Open Tank and Test Measurement Data
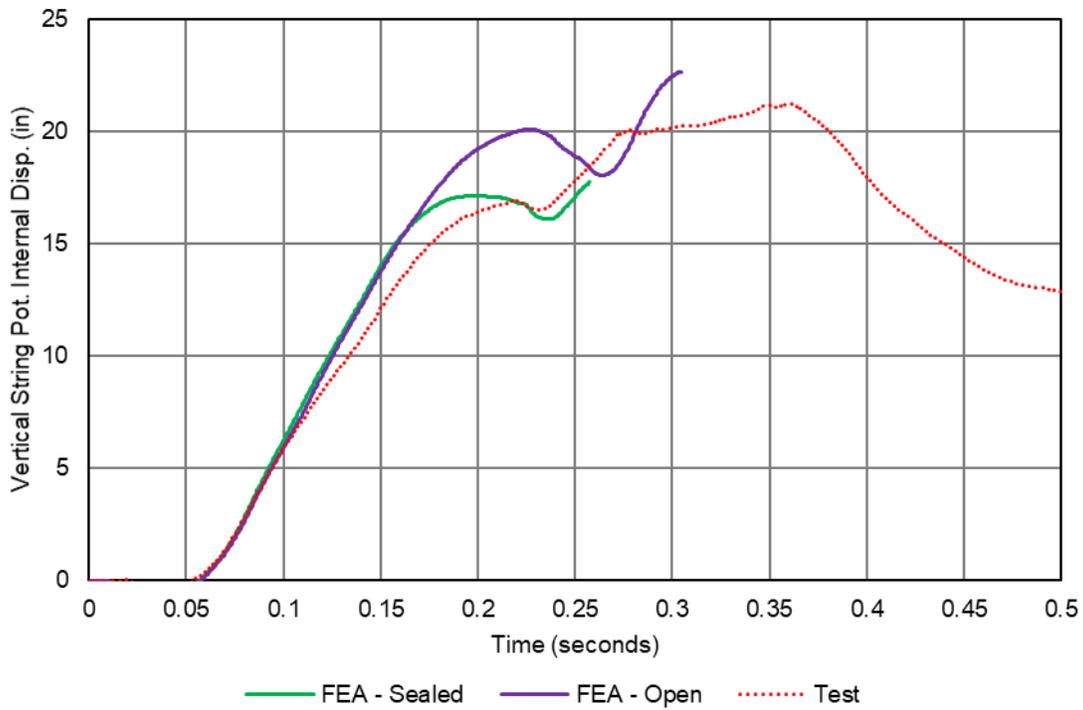
Figure C24. Internal Vertical String Potentiometer, Post-Test FEA with Sealed and Open Tank and Test Measurement Data

C3 – Post-Test Non-Puncture FEA and Test Measurement Results – 13.9 mph

As discussed in Section 7, neither the fully sealed nor the open post-test puncture FEA models could fully capture the response of the tank car during the test, since the tank car experienced expulsion of air and water out of the manway and cover plate during impact. To better understand the effect of air leakage out of the manway during the test, a non-puncture post-test FEA was run with the measured outage pressure from the test defined as an input into the model.

In this model, the pneumatic cavity was removed and the surface of the outage was assigned a pressure load that varied with time corresponding to the pressure-time history measured in the outage during the test. A non-puncture FE model was used for this portion of the post-test investigation into the effects of leakage, as that type of model typically runs much more quickly than a puncture-capable model. Since the test resulted in the impactor nearly being brought to a stop at the point of puncture of the tank, a non-puncture model should be expected to exhibit good agreement with the overall test response up to a point fairly late in the impact event.

For all the non-puncture FEA results, the same post-test elastic-plastic material behavior for TC128 steel was assigned to the tank, except ductile damage and fracture were disallowed. Results derived from accelerometers or pressure transducers have been filtered using a CFC60 filter. The impactor in the post-test puncture and non-puncture models was moved approximately 1-inch away from the tank to account for the gap in the triggering mechanism and the test data was not time-shifted.

The post-test non-puncture FEA results using the assigned test pressure (FEA NP Test Press.) are denoted as solid black lines in the plots below. For the sake of comparison, the post-test non-puncture FEA was also run with the same sealed (FEA NP Sealed) and open (FEA NP Open) pressure conditions that were used in the post-test puncture FEA to bound the test response.

In comparing the non-puncture FEA results, the sealed case overestimates the apparent stiffness of the tank and the open case underestimates the stiffness up to 0.25 seconds of impact time. However, the non-puncture FEA with the assigned test pressure is in near perfect agreement with the test data up to 0.25 seconds. From 0.25 to 0.35 seconds of impact time, a large amount of water expulsion through the manway was observed in the test (see Figure 22) which cannot be directly estimated by reviewing the test data and videos. The FEA using the test pressure captures the global force-displacement response up to just before 0.25 seconds. These results show that the loss of water from the manway and cover plate is also responsible for some of the apparent softened test response, which none of the models have been designed to capture.

The results of the FE model using the measured air pressure as an input to provide strong evidence that the FE model can reproduce the global dynamics of the impact, up to a point. As larger quantities of water leak from the manway and cover plate, the FE models are all limited by an inability for water to leave the tank. As water is effectively incompressible, further impactor travel in the model is met with higher resistance from the water, where in the test the water was simply "squeezed" out of the top fittings. As the point of the non-puncture models was to confirm or refute the leakage as the source of the global stiffness disagreement between test and FEA, no further efforts were made to adjust the model to account for the water leakage through the top fittings.
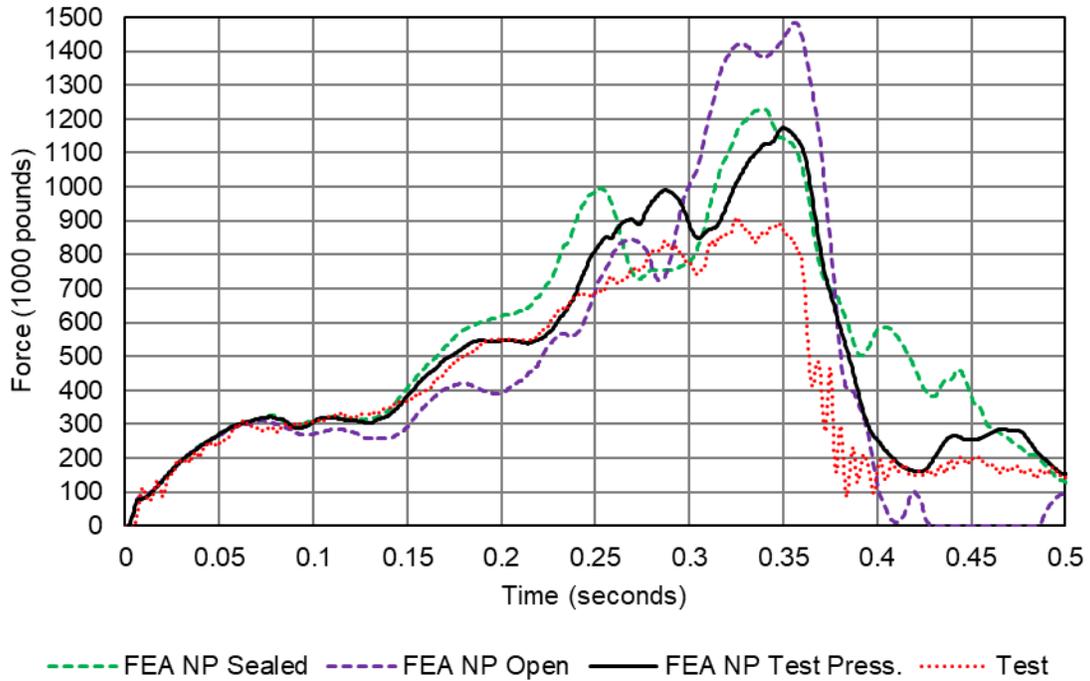
Figure C25. Impact Force vs. Time, Post-Test Non-Puncture Sealed, Open, and Test Pressure FEA and Test Measurement Data
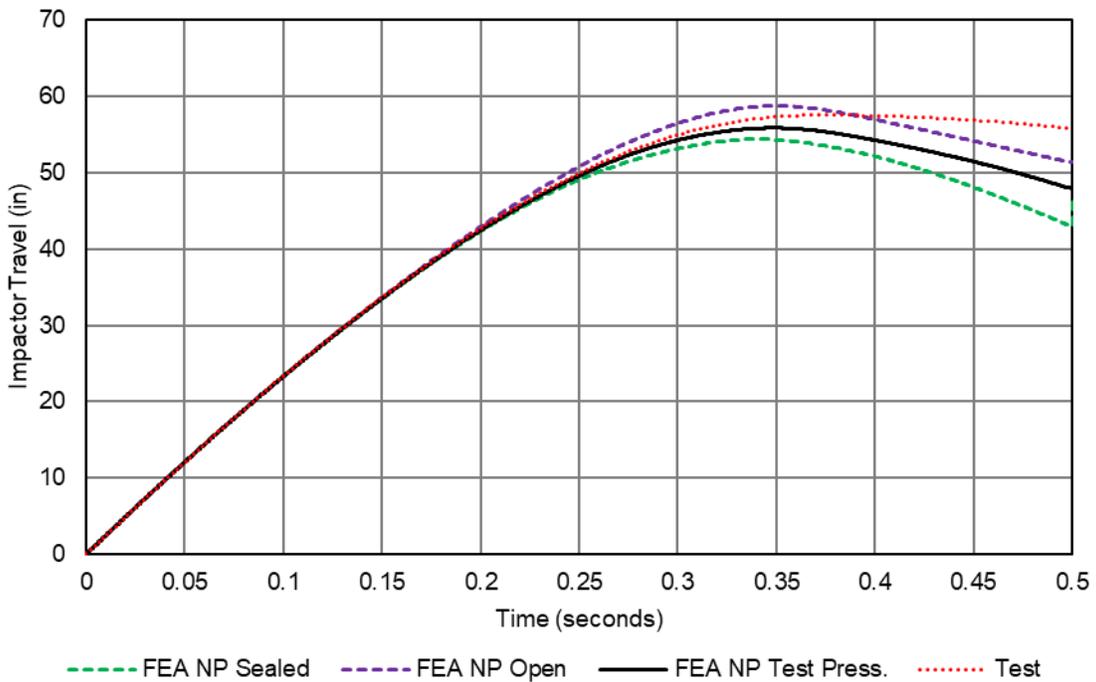
Figure C26. Impactor Travel vs. Time, Post-Test Non-Puncture Sealed, Open, and Test Pressure FEA and Test Measurement Data
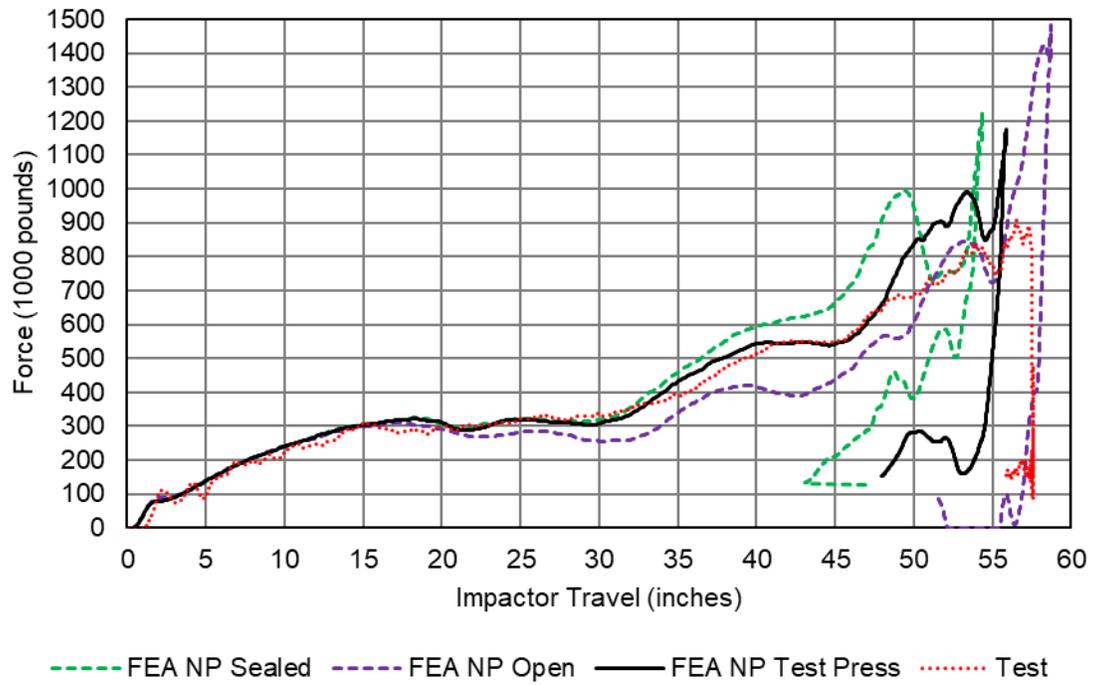
Figure C27. Impact Force vs. Impactor Travel, Post-Test Non-Puncture Sealed, Open, and Test Pressure FEA and Test Measurement Data

Appendix D.
Geometry in Pre-Test and Post-Test Finite Element Models

The following discusses each of the parts making up the model. Note that for parts that are bisected by the symmetry plane, the values reported in the following tables for mass and number of elements correspond to what was included in the FE model (i.e., half the mass of the physical body during the test).

Rigid parts were used when it was important to include a part for its inertia or for its interaction through contact, but where the deformation of the part could be neglected in the calculations. Four parts were modeled as rigid bodies. The remaining bodies were modeled as deformable bodies.

A summary of the element types used to mesh the model assembly is provided in Table D1.

Table D1. Summary of Element Types from (Dassault Systemes Simulia Corp, 2014)

Element Designation	Description
C3D8	8-node linear brick element for stress and displacement modeling
CONN3D2	Connector element between two nodes or ground and a node
DCOUP3D	Three-dimensional distributing coupling element
M3D3	3-node triangular membrane element
M3D4R	4-node quadrilateral membrane element (reduced integration)
MASS	Point mass
R3D3	3-dimensional, 3-node triangular facet rigid element
R3D4	3-dimensional, 4-node bilinear quadrilateral rigid element
RNODE3D	3-dimensional reference node
S3R	3-node triangular general-purpose shell, finite membrane strains (identical to element S3)
S4	4-node general-purpose shell, finite membrane strains
S4R	4-node general-purpose shell, reduced integration with hourglass control, finite membrane strains
SFM3D3	3-node triangular surface element
SFM3D4R	4-node quadrilateral surface element
SPRINGA	Axial spring between two nodes, whose line of action is the line joining the two nodes. This line of action may rotate in large-displacement analysis.

D1 – Rigid Impactor

The impactor was modeled as a rigid body in the DOT-111 FE models. The simulations used a 12-inch by 12-inch square impactor with 1-inch radii edges around the impact face. The geometry included the impact face and the tapered cone back to the portion of the impactor where the impactor attached to the ram car. Because only the impactor itself was modeled and this model used one-half symmetry, half of the mass of the entire ram car was assigned to the reference node on the impactor. The impactor, both with and without mesh, is shown in Figure D1. Table D2 shows the properties of the impactor in the pre-test and post-test FE models.
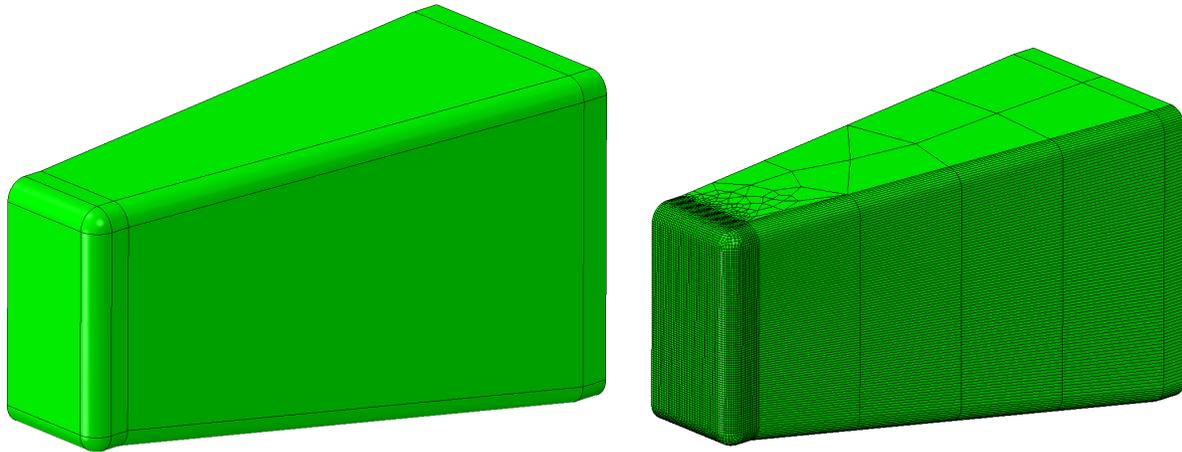
Figure D1. Impactor Geometry (left) and Mesh (right)

Table D2. Properties of Impactor in Pre-test and Post-test FE Models

Type of Part	Rigid
Number of Elements	R3D4: 7,706 R3D3: 58 RNODE3D: 5 MASS: 1
Approximate Mesh Size	0.125 inch to 6 inches
Approximate Part Weight	148,500 lbf

D2 – Rigid Wall

The rigid wall was modeled as a rigid body in the DOT-111 FE model. Because the wall was constrained against motion in any direction, no mass needed to be defined for this part. The wall's geometry and mesh are shown in Figure D2. Table D3 shows the properties of the rigid wall in the pre-test and post-test FE models.
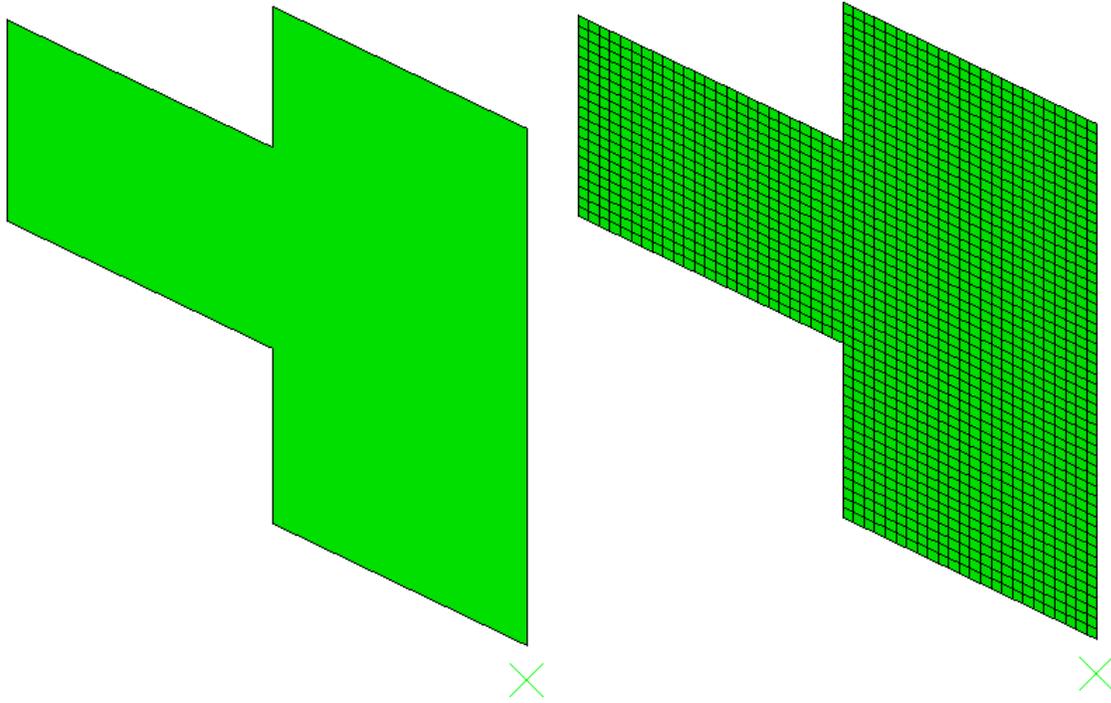
Figure D2. Rigid Wall Geometry (left) and Mesh (right)

Table D3. Properties of Rigid Wall in Pre-test and Post-test FE Models

Type of Part	Rigid
Number of Elements	R3D4: 1,341 RNODE3D: 4
Approximate Mesh Size	3.5 inches

D3 – Rigid Skid

The trucks of the tank car were removed prior to the test. The body bolster of the car rested directly upon a set of skids, which themselves rested upon steel plates (see Figure 6). The skids were designed to inhibit rigid body roll of the tank car following rebound from the rigid wall during a test. The skid geometry and mesh are shown in Figure D3. Note that since this part exists entirely to one side of the symmetry plane, the mass and geometric properties correspond to the actual mass and geometry of one full skid. Table D4 shows the properties of the skids in the pre-test and post-test FE models.
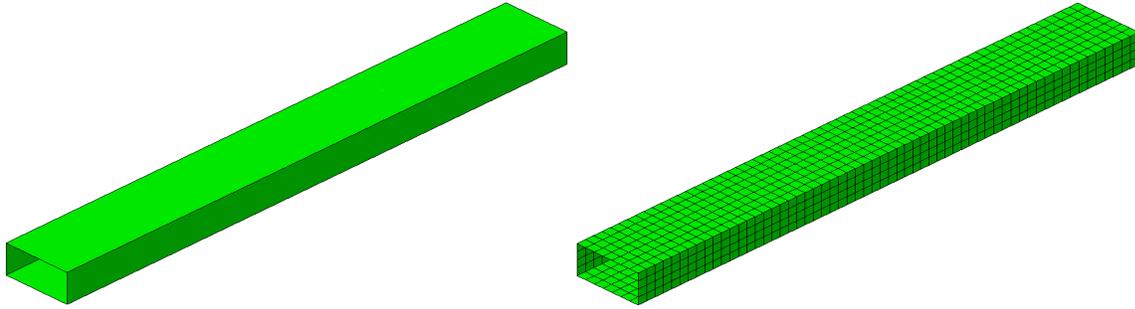
Figure D3. Skid Geometry (left) and Mesh (right)

Table D4. Properties of Skid in Pre-test and Post-test FE Models

Type of Part	Rigid
Number of Elements	R3D4: 936 MASS: 2 RNODE3D: 2
Approximate Mesh Size	3.5 inches

The rigid skids used in the test weigh approximately 3,500 pounds each. This mass was included in the model using a point mass at the rigid body reference node of each skid. Because the FE model is a simplified representation of the tank, the model does not include such geometric details as the body bolsters, draft sills, draft gear, or couplers, as these features are not expected to play a significant role in the puncture response for an impact near the center of the shell. The masses of these components are included as a second point mass on the skid. For this car, the additional structure at each end of the tank car was assumed to have a weight of approximately 7,700 pounds (Table D5). These additional point masses were added to both the pre-test and post-test FE models without adjustment.

Table D5. Point Masses Added to Skid Reference Point in FE Models

Component	Approximate Weight lbf
Skid	3,500
Draft Sill, Draft Gear, Coupler, Body Bolster, etc.	7,700

D4 – Tank – Shell Elements

The commodity tank was modeled using two different techniques. In the impact zone, the tank was modeled using solid "brick" elements. This part is discussed in Section D5. Away from the impact zone, the tank was modeled using shell elements. The shell portion of the tank is described in this section. Because only half the tank is included in the FE model due to symmetry, the mass of the tank in the FE model corresponds to half the mass of the physical tank.

Figure D4 shows the shell portion of the tank. This part was globally meshed using quadrilateral reduced integration (S4R) elements with a 3.5-inch mesh seed. At the edges of the impact zone,

the mesh was seeded such that each shell element edge would span exactly two solid elements on the impacted patch. The mesh in the region of attachment to the solid plate was meshed using quadrilateral fully integrated (S4) elements. A technique referred to as shell-to-solid coupling was used to attach the solid patch to the edges of the shell mesh on the tank. The shell part of the tank represents the midplane surface of the tank. The shell part has a midplane diameter of 123 inches in the model. The models include a small number of S3R elements.
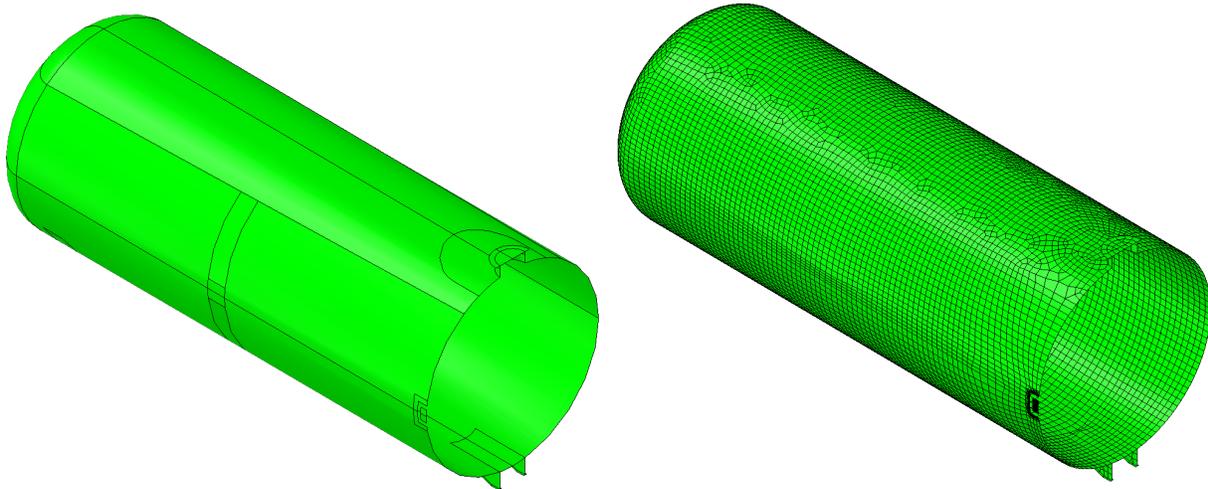
Figure D4. Shell Tank Geometry (left) and Mesh (right)

The pre- and post-test FE models featured similar geometries. In the post-test model, the solid tank patch was modified slightly to ensure that if puncture occurred, it did not initiate in any of the edges involved in the shell-to-solid coupling. The shell mesh was adjusted slightly to ensure a compatible mesh with the solid part. The shell tank parts in the pre-test and post-test models are summarized in Table D6.

Table D6. Properties of Tank Shell Mesh in FE Models

Type of Part	Deformable, Shell
Number of Elements	S4R: 4,878 S4: 516 S3R: 163
Approximate Mesh Size	0.17 to 3.5 inches
Shell Thickness	0.5 inch
Head Thickness	0.5 inch
Approximate Part Weight	19,000 lbf

D5 – Tank – Solid Elements

The commodity tank was modeled using two different techniques. Away from the impact zone, the tank was modeled using shell elements. This part is discussed in Section D4. In the impact zone, the tank was modeled using solid brick elements. The solid portion of the tank is described in this section. Because only half the tank is included in the FE model due to symmetry, the mass

98

of the solid portion of the tank in the FE model corresponds to half the mass of the corresponding portion of the physical tank.

Figure D5 shows the solid portion of the tank and Table D7 lists the properties of tank solid mesh in FE models. The outer height of the part measures approximately 12.25 inches high by 6.125 inches wide in both the pre-test and post-test models. The inner cutout measures approximately 8.5 inches high by approximately 4.5 inches wide in the pre-test model, and 8 inches high by 4 inches wide in the post-test models. The part was meshed using a 0.083-inch mesh seed, resulting in six elements through the thickness of the tank shell. The solid portion of the tank was meshed using 8-noded hexahedral "brick" (C3D8) elements. The solid tank mesh was attached to the shell tank mesh along the outer and inner edges using shell-to-solid coupling. The elements along the inner and outer edges of the solid tank that were involved in the shell-to-solid coupling were given the same elastic and plastic material responses as the rest of the solid patch but did not have damage initiation or failure behaviors defined. This was done to prevent elements involved in the shell-to-solid coupling from being removed from the model, as that could cause the coupling itself to fail.
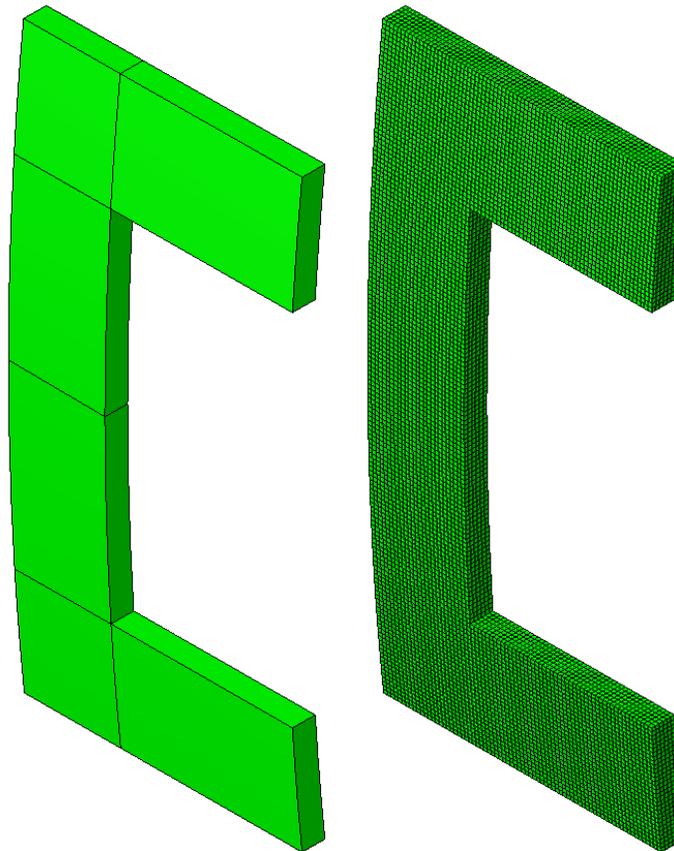
Figure D5. Tank Solid Geometry (left) and Mesh (right)

The properties of the solid tank part are summarized in Table D7 for the pre-test and post-test models.

Table D7. Properties of Tank Solid Mesh in FE Models

Type of Part	Deformable, Solid
Number of Elements	C3D8: 40,992
Approximate Mesh Size	0.083 inch
Thickness	0.5 inch
Approximate Part Weight	7 lbf

D6 – Membrane

The FE model of the DOT-111 tank car included a deformable membrane and surface part that represented the extents of the lading. The gas phase of the contents of the tank was modeled within the tank using a pneumatic cavity. The material properties used to describe the behavior of the air are described in Section 5.3.3, and the material properties used to describe the water are described in Section 5.3.2. In the model, the outage volume was filled with air.

The pneumatic cavity model requires a geometric surface to be defined within the model that defines the boundary of the cavity. Because the tank car model is a half-symmetric model, the cavity is not entirely enclosed within the membrane. In the case of a cavity bisected by a symmetry plane, it is necessary to place the cavity's internal reference point on the symmetry plane.

As discussed in Section D4, the shell geometry of the tank represents the mid-plane geometry of the tank. If this geometry were used to define the outer surfaces of the pneumatic cavity, the cavity volume would be too large, since the volume enclosed was based on the mid-plane surface and not on the inner surface of the tank. The membrane part was defined to correspond to the inner surface of the tank's geometry.

The membrane part was meshed using surface elements for the portion of the part along the interior of the tank, and with membrane elements for the portion of the part that defined the interface between the water and the air within the tank. Surface elements do not have a defined thickness or material behavior. Thus, these elements must be constrained to an element with these properties defined to prevent the surface elements from unconstrained distortion. The surface elements were attached to the mid-plane surface of the tank using a tied constraint. The geometry and mesh of the membrane part are shown in Figure D6.
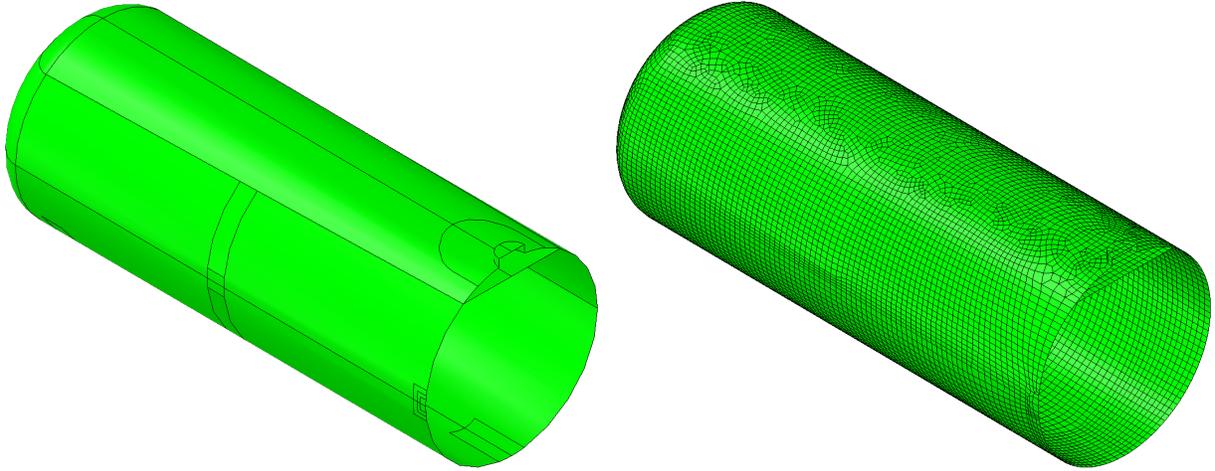
Figure D6. Membrane Geometry (left) and Mesh (right)

Because the portion of the membrane defined to divide the water and air boundary represents geometry that is not physically present within the tank, surface elements would not be suitable for this part. Instead, a membrane element representation was chosen to be as thin and flexible as practical within the model, without causing the model to terminate due to excessively distorted membrane elements. With these constraints, a thickness of 0.05 inch was chosen for the membrane.

The DOT-111 tank car used in this test featured a sloped shell geometry to facilitate bottom unloading of its lading. This means that a liquid lading at rest will have a horizontal free surface, but the height from this free surface to the interior of the tank at 12 o'clock will increase as the position of interest moves further from the center of the tank. The zero-outage condition for this car is defined as the volume of lading that will fill the tank to the point that lading makes contact with the interior of the tank at the 12 o'clock position, dividing the remaining space within the car into two volumes no longer in communication with one another. The height of the horizontal plane (measured from the 12 o'clock position of the membrane at the symmetry plane, as shown in Figure D7) was adjusted to give the desired outage for this tank.
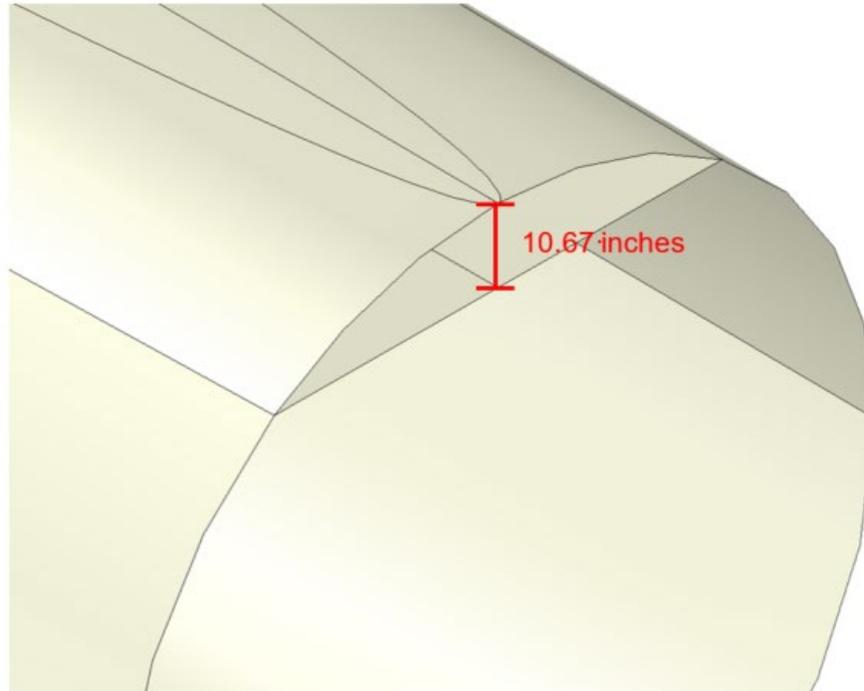
Figure D7. Reference Points for Outage Height within Membrane Part

The relationship between outage height and outage volume for this model is shown in Figure D8. This figure also includes an outage relationship from a tank car builder's public webpage of gage tables[3] as a check on the relationship calculated using the FE model. For the desired outage of 5 percent, the model used an outage height of approximately 10.67 inches below the top of the membrane.

---

[3] A gage table contains tabular data on the relationship between the height of lading (innage) within a tank car, the height of the empty space (outage) within a tank car, and the volume of said innage or outage to assist with loading tank cars. The gage table from a DOT-111A100W car having the same capacity as the test car (see the Gauge Table Information Resource) was used.
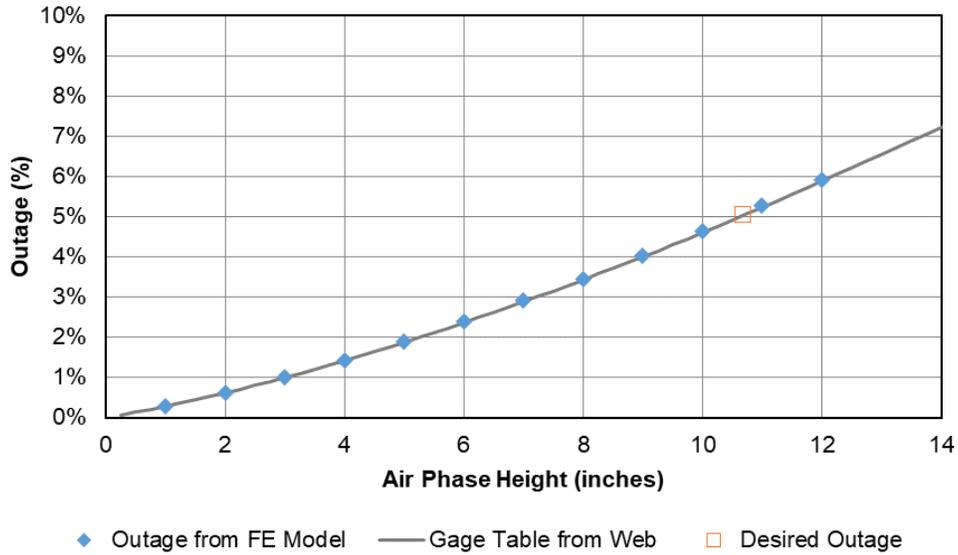
Figure D1. Outage Height vs. Outage Volume for DOT-111 Model

The properties of the membrane part are summarized in Table D8 for the pre-test and post-test FE models.

Table D8. Properties of Membrane Mesh in FE Model

Type of Part	Deformable, Surface and Membrane
Number of Elements	SFM3D4R: 11,272 SFM3D3: 107 M3D4R: 2,107 M3D3: 38
Approximate Mesh Size	3.5 inches
Approximate Part Weight	300 lbf

D7 – Ground

For both the pre-test and post-test FE models, the rigid ground was modeled with all six degrees-of-freedom (DOF) fixed, as Figure D9 shows. Table D9 lists the properties of ground meshes in the FE models.
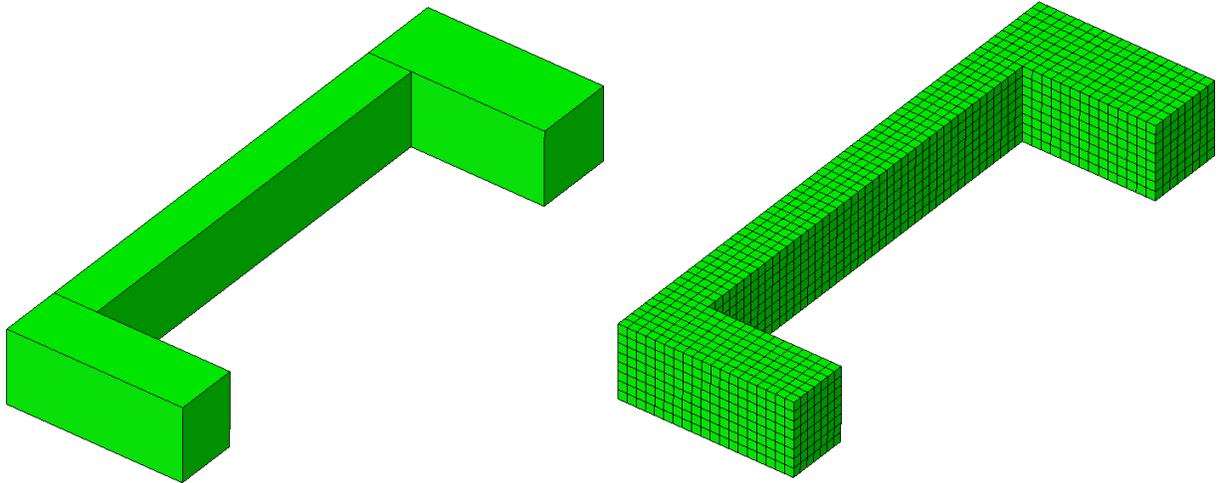
Figure D9. Rigid Ground Geometry (left) and Mesh (right)

Table D9. Properties of Ground Meshes in FE Models

Type of Part	Rigid Body
Number of Elements	R3D4: 2,562 RNODE3D: 3
Approximate Mesh Size	1.5 inches

D8 – Water

The water phase of the lading was modeled as a deformable Lagrangian part in both the pre-test and post-test FE models. The properties of the water material are defined in Section 5.3.2. The geometry of the water part and its mesh are shown in Figure D10, and Table D10 lists the properties of the water mesh in the FE model.
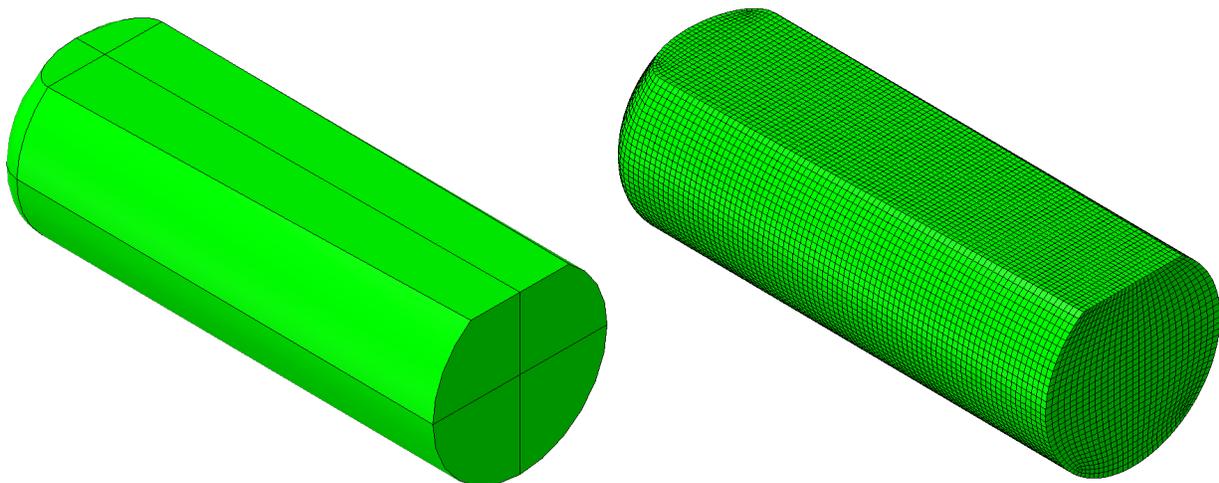
Figure D10. Water Geometry (left) and Mesh (right)

Table D10. Properties of Water Mesh in FE Model

Type of Part	Deformable
Number of Elements	C3D8: 77,932
Approximate Mesh Size	3.5 inches
Approximate Part Weight	118,000 lbf

Appendix E.
Modeling Techniques Common to Pre-test and Post-Test Finite Element Models

E1 – Symmetry Conditions

During the impact test, the test plan called for the impactor to strike the DOT-111 tank car at its longitudinal center. To facilitate computational efficiency, this permitted a half-symmetric model to be used to simulate the test. A symmetry boundary condition was applied to the tank (solid and shell element portions), the jacket, the water, and the internal surface dividing the two phases of the lading.

E2 – Rigid Impactor Boundary Conditions

The rigid impactor was constrained against all motion except for longitudinal displacement. The impactor was given an initial velocity corresponding to the simulated impact speed. The pre-test FE models were run at various speeds, and the post-test FE model was run at the measured test speed of 13.9 mph.

E3 – Rigid Wall Boundary Conditions

The rigid wall was constrained against motion in all degrees-of-freedom (DOF).

E4 – Ground Boundary Conditions

The ground was constrained at all six DOF.

E5 – Tank-to-surface Tie

The portion of the tank modeled using shell elements was tied to the surface representing the interior surface of the tank using a tied constraint. Although the meshes used on both parts were similar, because they were not identical, a position tolerance of 3.5 inches was used.

E6 – Tank-to-skid Coupling

The tank was connected to the rigid skid through a kinematic coupling. This coupling applied to all six DOF. The coupling was defined between the arc of nodes on the tank, which represent the body bolster and the rigid body reference point of the skid, as shown in Figure E1.
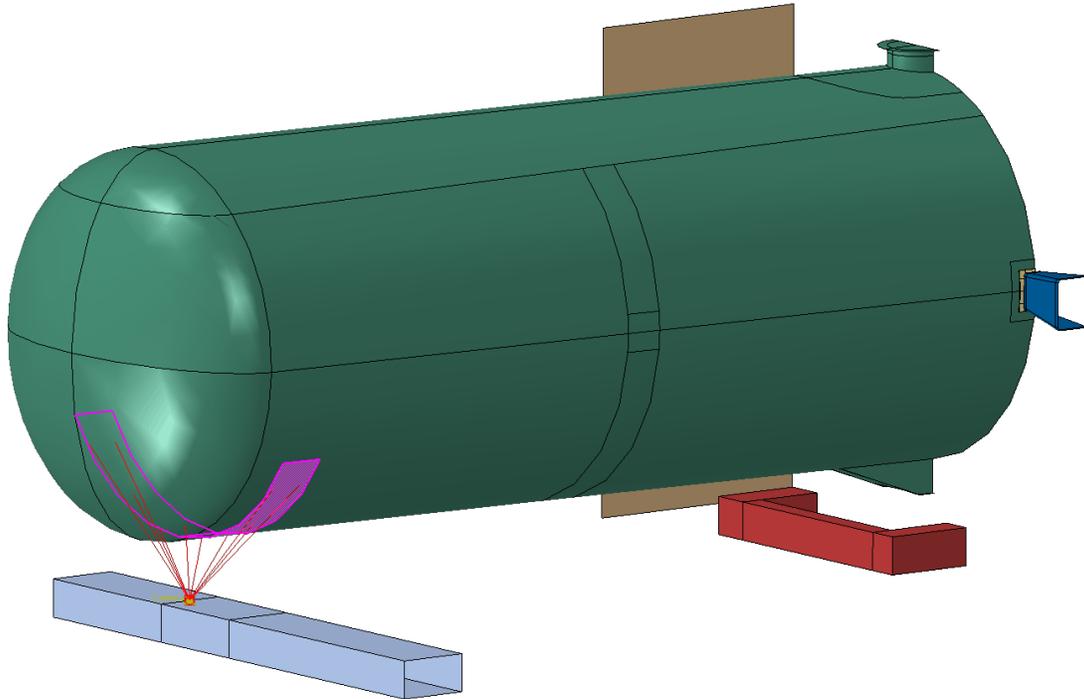
Figure E1. Tank-to-Skid Coupling

Additionally, a "Cartesian" type of connector was used to constrain the motion of the skid in both the vertical and the longitudinal (in the direction of impactor travel) directions. A nonlinear damper was defined between the skid and ground to constrain longitudinal motion. This damper defined the longitudinal resistance force as a function of skid speed, such that the skid had to overcome an initially high force when it was moving slowly. Once this initial peak was overcome, the resistance offered to skid motion diminished as the skid moved more quickly. This simplified model was intended to approximate the effect of static friction being overcome as the skid initially begins its motion, followed by a reduced resistance from kinetic friction. The longitudinal relationship used in the Cartesian connector is shown in Table E1 and plotted in Figure F2.

Table E1. Longitudinal Skid Behavior

Skid Velocity *in/s*	Reaction Force *lbf*
-10	-100
-1	-38,000
0	0
1	38,000
10	100
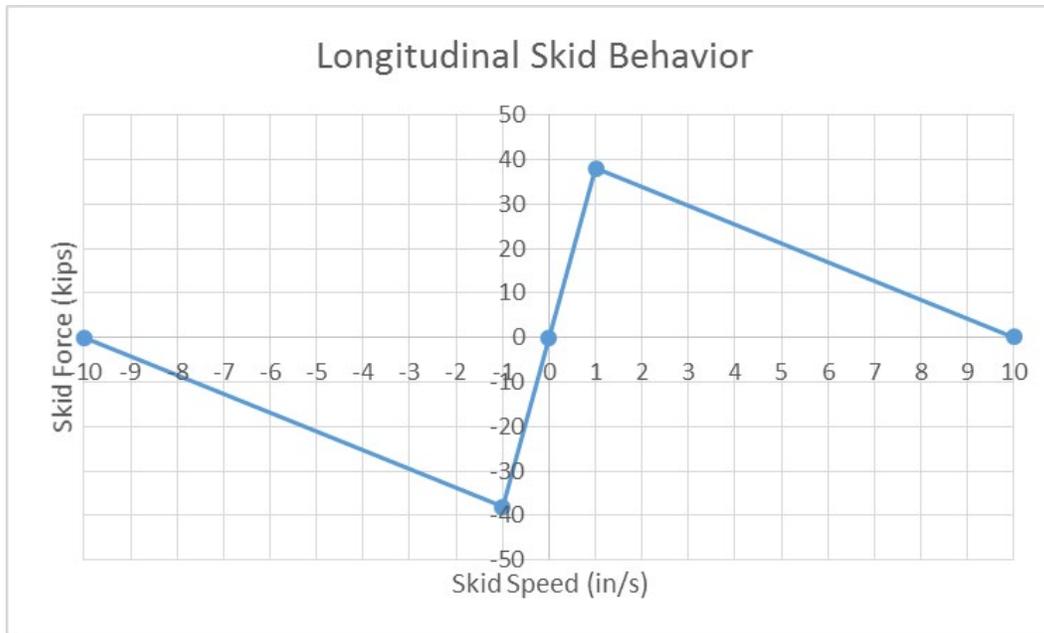
Figure E2. Longitudinal Skid Behavior

In the vertical direction, the skid used a "Stop" behavior assigned to a connector between skid and ground to limit its range of motion. In the vertical downward direction, the reference point of the skid was prevented from having any displacement. In the upward direction, a limit of 100 inches was used. This number is arbitrary, but it was chosen to be larger than any anticipated vertical motion of the skid. These two vertical stops approximated the behavior of the skid on the ground during the physical test, where the skid was prevented from moving downward through contact with the ground but free to lift upward if sufficient lifting forces overcame the weight resting on it.

E7 – Shell-to-Solid Coupling

A shell-to-solid coupling constraint was used to attach the patch of solid elements in the vicinity of the impact zone to the rest of the shell-meshed tank. This type of constraint is necessary to ensure a smooth transition from solid elements, which possess only translational DOF, to shell elements, which possess translational and rotational DOF. The meshes on the solid part and the shell part were controlled such that every element on the shell edges involved in the coupling spanned two solid elements. Since the shell part corresponded to the mid-plane thickness of the tank, the shell part was aligned with the mid-plane of the solid patch. The interface between the solid patch and the shell tank is shown in Figure E3. The solid patch is shown in dark red, while the shell mesh of the tank is tan.
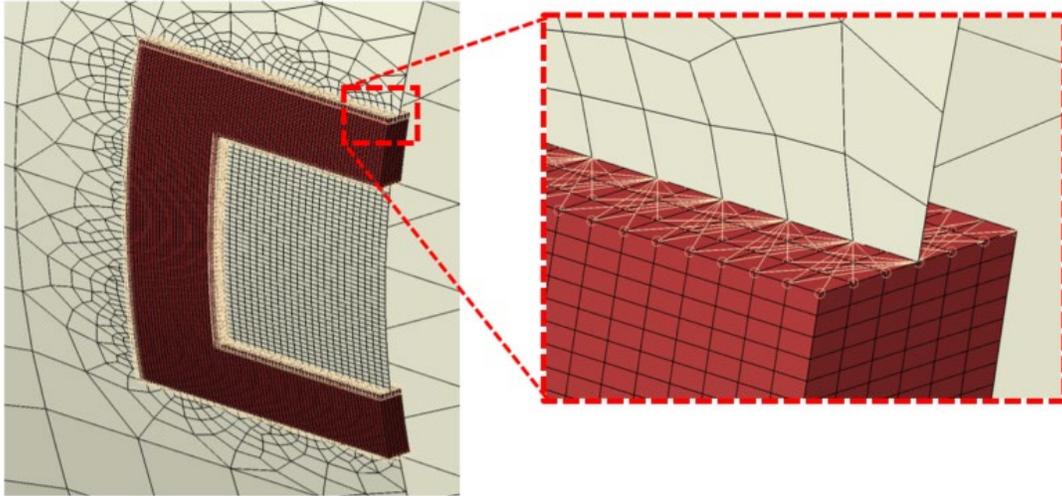
Figure E1. Shell-to-Solid Coupling Region

E8 – Internal Pressures and Temperatures

The lading within the tank was given an initial pressure of 12.3 psi (Engineering ToolBox, 2003), corresponding to atmospheric pressure at Pueblo, CO's, altitude of approximately 4,700 feet (U.S. Geologic Survey, 2019). As the water and gas phases deformed, the pressure was free to change in response.

Using the fluid cavity approach of modeling the air phase required an initial temperature to be defined for the lading. Based on average historical climate data around the planned date of the DOT-111 test, an initial temperature of 57 °F was chosen for the models (U.S. Climate Data version 3.0, 2019). The initial temperature definitions were adjusted between the pre-test and post-test models to match the measured test day temperature of 47 °F.

E9 – Springs

Soft springs (k=1 ×10^{-6} lbf/inch) were placed within the model at locations corresponding to the string potentiometers installed within the tested tank (see Section 3.3). The use of springs allowed a direct comparison between the change-in-length of a string potentiometer during the test and the change-in-length of the corresponding spring in the FE model.

E10 – Pressure Relief Valve Modeling

The PRV was approximated in the model as a fluid exchange between the pneumatic cavity representing the outage (see further description of outage modeling in Section 5.3.3) and ambient air, using a "Volume Rate Leakage" approach. The PRV in the test had a start-to-discharge pressure of approximately 75 psi. Because there is some tolerance for when the PRV can open, the FE model assumed a 78-psi internal pressure before appreciable flow occurred. The model used a prescribed pressure versus volumetric flow rate relationship to approximate the behavior of the PRV during the impact simulation.

The volumetric flow rate relationship used in the pre-test FE model was based on the PRV model developed in a previous DOT-117 tank car FE model (Rakoczy, P., Carolan, M., Gorhum, T., & Eshraghi, S., 2019). The flow rates were first converted from standard cubic feet per minute

(SCFM) to actual cubic feet per minute (Ohio Medical Corporation, 2017) to account for the test being conducted at an elevation of approximately 4,700 feet. The flow rates were further converted into the unit system used by the model, so that the volumetric flow rates in the FE model were defined as actual cubic inches per second. After the test, it was discovered that the actual flow rate of the PRV (1,113 SCFM) was lower than anticipated so the flow rate was lowered in the post-test model. The air pressure versus volumetric flow rate relationship input to the FE models is shown in Table E2.

Table E2. Volumetric Flow Rate Relationship for PRV Modeling

Gage Pressure psi	Pre-Test Model Volumetric Flow Rate in.³/s	Post-Test Model Volumetric Flow Rate in.³/s
0	0	0
	0	0
78	0	0
79	75,013	2,709.2
80	150,027	5,418.4
81	225,040	8,127.5
82	300,053	10,836.7
83	375,066	13,545.9
84	450,080	16,255.1
85	525,093	18,964.3
	525,093	18,964.3

E11 – Mass Scaling

Variable mass scaling was used in both the coupon models and the full-scale puncture models. Because of the need for a refined mesh of solid elements in the impact zone, the puncture models feature many very small (0.083-inch) elements. The models also simulated 0.5 seconds of the impact, which is a long simulation time for an explicit model. These two factors combine to create simulations with significant CPU runtimes, even when executed with parallelization across multiple CPUs. Variable mass scaling was employed in the FE models to decrease the runtime without decreasing either the span or the resolution of the refined meshes. Variable mass scaling is a technique in which the user sets a target time increment for a set of elements within the model (up to and including all elements within the model) and the Abaqus solver increases the mass of each element to attempt to bring the minimum timestep up to the user-defined minimum. "Variable" refers to the software's ability to increase the mass of each element by a different amount, based on the material and geometry of each element. While mass scaling is an efficient way of reducing runtime without remeshing a model, care must be exercised when using this technique with highly dynamic simulations. If an overly aggressive mass scaling is applied, the amount of artificial mass added to the model in the refined mesh area can significantly affect both the overall dynamic response and the local puncture behavior of the model.

The material coupon models used a mass scaling of 1 x 10^{-6} seconds. Mass scaling was observed to have relatively little influence over the results of the coupon simulation, as the loading was chosen to be quasi-static.

The pre-test and post-test puncture FE models used a variable mass scaling of 5 x 10^{-7} seconds over the entire model. The mass scaling factors were recalculated at 20 intervals during the simulation. This mass scaling factor is considered moderate, and it was chosen based on the need to perform the pre-test simulations in a timely manner in accordance with the planned test schedule.

E12 – Contact

A general contact definition was used in this FE model. The global contact used frictionless contact, except for metal-on-metal contact. A coefficient of friction of 0.3 was defined between the impactor and jacket, between the jacket and tank, and between the rigid wall and jacket. A coefficient of 0.5 was used for contact involving the ground slab. Contact exclusions were defined between the shell tank and the solid tank patch.

Appendix F.
Material Behaviors in Finite Element Models

F1 – Introduction

Pre-test finite element (FE) models used TC128 steel material responses for the tank that were based on publicly available TC128 tensile data as described in Section 5.3.4.

Following the test, subscale smooth round bar tensile coupons were cut from the tested DOT-111 tank car and subjected to testing. The results of these material coupon tests were used to create a new TC128 material for post-test modeling. The processes used to create the pre-test and post-test material models are described in this appendix.

F2 – Simulation of Coupon Tests

FE simulations of TC128 tensile coupon tests were used to calibrate the material definitions in Abaqus. First, the plastic true stress-plastic equivalent strain (PEEQ) characteristic was specified. Then, the damage initiation envelope was calculated. Finally, a reasonable damage progression was empirically determined.

As the material responses developed using a coupon model were planned for implementation in the full-scale DOT-111 tank car model, modeling techniques for performing the coupon simulations were chosen deliberately to be similar to the modeling techniques planned for side impact analysis of the DOT-111 tank car. The same solver (Abaqus/Explicit), element types, and mesh densities were chosen. This was done to attempt to minimize the uncertainty associated with calibrating a material response using one set of techniques but using a different set of techniques to model puncture in the tank car impact simulation. If the tank car model was run using a different solver or different mesh density, it was expected that the material behaviors would need to be recalibrated using coupon simulations that used similar solvers and mesh density.

A 2-inch gage length, 0.5-inch thick and wide dog-bone specimen was used in the pre-test models, and a 1.4-inch gage length, 0.35-inch diameter smooth round bar specimen was used in the post-test models. Within the tensile coupon FE models, a soft (1 x 10^{-6} lbf/in) spring was included in the model to represent an extensometer attached to the ends of the 2-inch (pre-test) or 1.4-inch (post-test) gage. This spring was surrogate for an extensometer in the model and simplified the process of requesting the change-in-length of the gage section from the model.

Previous simulations of puncture tests used mesh sizes in the coupon and tank shell that were the same (typically approximately 0.085 inch) (Rakoczy, P., & Carolan, M, 2016) (Rakoczy, P., Carolan, M., Gorhum, T., & Eshraghi, S., 2019) (Carolan, M., & Rakoczy, P., 2019). The 0.083-inch mesh size used in the DOT-111 puncture models and pre-test coupon simulations (as shown in Figure F1) could not be applied to the smaller (0.35-inch diameter) post-test coupons because it resulted in a mesh that was too coarse. The mesh size was reduced to 0.050 inch and then further reduced to 0.035 inch for the post-test smooth round bar coupons which resulted in four and five elements across the radius respectively as shown in Figure F2. For comparison, the 0.5-inch thick solid tank patch was modeled with six elements through it (see Figure D5).
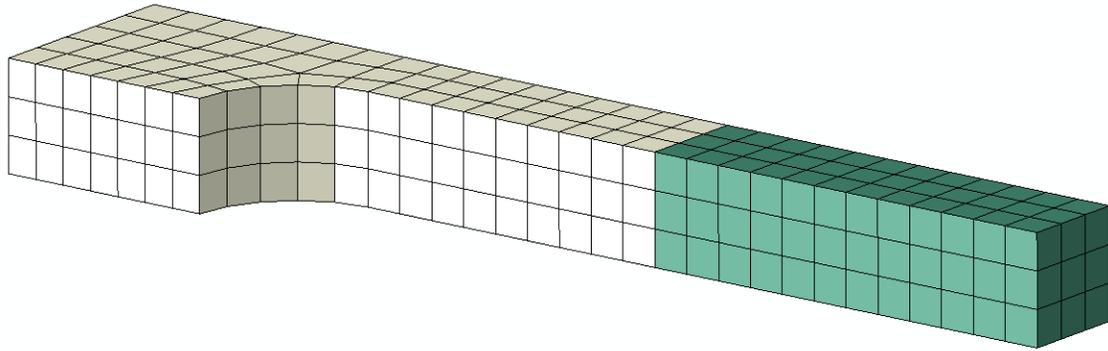
Figure F1. FE Model of Pre-test Dogbone Tensile Coupon Used to Estimate Lower and Upper TC128 Material Response
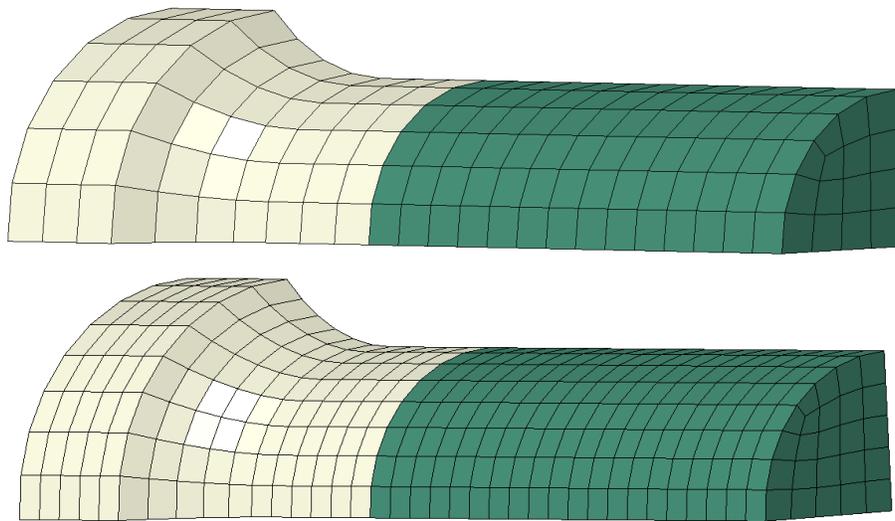
Figure F2. FE Model of Post-test Smooth Round Bar Tensile Coupon Used for Calibration of TC128 Material with 0.050-inch Mesh (top) and 0.035-inch Mesh (bottom)

Abaqus/Explicit requires metal plasticity to be defined in terms of true stress and PEEQ. The plastic behavior of each estimation of TC128 was input to the Abaqus model as isotropic hardening using a discrete number of data points. True stress can be calculated from the nominal stress-strain tensile coupon data according to Equation F1.

$$\sigma_{true} = \sigma_{nom} \cdot (1 + \varepsilon_{nom})$$

$$\bar{\varepsilon}^{pl} = \ln(1 + \varepsilon_{nom}) - \frac{\sigma_{true}}{E}$$

σ_{nom} nominal (engineering) stress
ε_{nom} nominal (engineering) strain
σ_{true} true stress
$\bar{\varepsilon}^{pl}$ plastic equivalent strain (PEEQ)

Equation F1. True Stress-strain Transformation

Because necking dominates the nominal stress-strain response of the tensile coupon characteristic after the max force is achieved, the true stress-PEEQ relationship was extrapolated for strains beyond the strain at maximum force.

Figure F3 shows a schematic of the Bao-Wierzbicki (B-W) triaxiality (η) based damage initiation envelope (Bao, Y., & Wierzbicki, T., 2004), which was used in the TC128 material failure models. Triaxiality is defined as the ratio of the hydrostatic stress (mean stress) divided by the von Mises stress (equivalent stress) and describes the general stress state of an element. The B-W envelope consists of three regions: Mode I – Ductile Fracture, Mode II – Mixed Fracture, and Mode III – Shear Fracture.
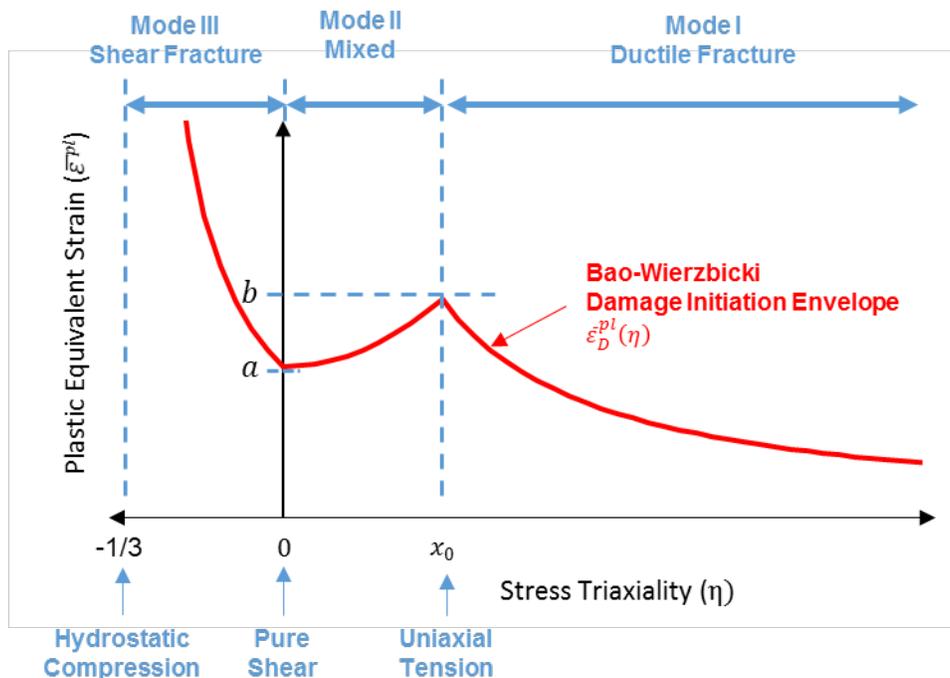
Figure F3. Schematic of B-W Damage Initiation Envelope

When $\eta < 0$ the element is in a state of compression, and when $\eta > 0$ the element is in a state of tension. A triaxiality of $\eta = -1/3$ corresponds to a stress state of hydrostatic compression and $\eta = 0$ corresponds to pure shear. The cusp of the B-W envelope is located at the average triaxiality on the fracture surface of a smooth round bar specimen under uniaxial tension at $\eta = x_0$ and is typically close to a value of 0.4.

Three constants (a, b, x_0) govern the shape of the B-W damage initiation envelope (see Equation F3) and are calibrated based on coupon test results. The critical strain to fracture in pure shear (a) corresponds to the PEEQ on the B-W envelope $\left(\bar{\varepsilon}_D^{pl} \right)$ when $\eta=0$ (pure shear). The critical strain to fracture in uniaxial tension (b) corresponds to $\left(\bar{\varepsilon}_D^{pl} \right)$ at the cusp of the B-W envelope when $\eta=x_0$.

$$\bar{\varepsilon}_D^{pl}(\eta) = \begin{cases} \dfrac{a}{1 + 3 \cdot \eta} & -\dfrac{1}{3} \le \eta \le 0 \\[2ex] (b - a) \cdot \left(\dfrac{\eta}{x_0}\right)^2 + a & 0 \le \eta \le x_0 \\[2ex] \dfrac{b \cdot x_0}{\eta} & x_0 \le \eta \end{cases}$$

Equation F3. B-W Damage Initiation Envelope

The complete damage initiation envelope can be developed through a series of mechanical tests on 11 unique specimen geometries intended to cover a wide range of stress triaxialities; however, a simplified "quick calibration" approach was developed for industrial use by Lee and Wierzbicki (Lee, Y., & Wierzbicki, T., 2004) (Lee, Y.-W., 2005), which requires only one uniaxial tensile geometry to estimate the entire failure envelope. According to Lee, the quick calibration approach is intended to be within 10 percent agreement with a failure envelope that was developed using the complete set of 11 specimens.

The quick calibration procedure for smooth round bar tensile tests allows the calculation of the B-W envelope constants (a, b, x_0) by measuring the initial radius (a_0), final radius (a_f) displacement at maximum force (δ_d), and initial gage length (L_0). As seen in Equation F4, the quick calibration procedure also uses the hardening exponent (n) which is typically used to describe the plastic hardening behavior of metals.

$$n = \ln\left(1 + \frac{\delta_d}{L_0}\right)$$

$$b = 2 \cdot \ln\frac{a_o}{a_f}$$

$$x_0 = \frac{1}{3} + \frac{0.22}{b} \cdot (b - n)^{1.8}$$

$$a = b \cdot \left(\frac{\sqrt{3}}{2}\right)^{1/n}$$

Equation F4. Quick Calibration Procedure for Smooth Round Bar Uniaxial Tensile Tests

For ductile metals in Abaqus, the damage threshold of an integration point is reached when the ductile criterion (DUCTCRT) reaches a value of 1. The DUCTCRT is calculated by integrating the change in PEEQ divided by the PEEQ where damage initiates as a function of triaxiality (i.e., the B-W envelope) according to Equation F5.

$$DUCTCRT = \int \frac{d\bar{\varepsilon}^{pl}}{\bar{\varepsilon}_D^{pl}(\eta)}$$

Equation F5. Calculation of Ductile Criterion (DUCTCRT) in Abaqus

After DUCTCRT reaches a value of 1, the stiffness of the element is degraded according to the damage progression in the material definition. In this report, energy-based damage progression values are calibrated for each material; however, the damage progression could also be specified based on displacement.

F3 – AAR TC128 Grade B Steel

Three characterizations of TC128 steel were developed over the course of this study. Prior to the test, lower and upper estimates of TC128 steel with respect to toughness were developed based on publicly available tensile coupon data as described in Section 5.3.4. After the test, a third characterization was developed based on the measured properties of the TC128 steel from the tested DOT-111 tank car. For comparison, the results of tensile coupon simulations with the TC128 material models are summarized in Table F1. The pre-test lower and upper estimates of TC128 were successful in bounding the actual (post-test) material behavior.

Table F1. Summary of Mechanical Properties of TC128 from Coupon FE Models

| Material Model Name	YS	UTS	EB
	ksi	ksi	%
Pre-test Lower	57	85	31
Pre-test Upper	63	89	42
Post-test	60	86	32

F3.1 – Pre-test Characterization

Because the mechanical properties of the TC128 steel in the DOT-111 tank car were unknown prior to the test, upper- and lower-bound pre-test material models were developed using publicly available tensile test data from DOT-111 (National Transportation Safety Board, n/a) (Transportation Safety Board of Canada, 2013) (National Transportation Safety Board, 2012) (National Transportation Safety Board, 2016) and DOT-117 (Rakoczy, P., Carolan, M., Gorhum, T., & Eshraghi, S., 2019) tank cars. Three rail accidents involving DOT-111 tank cars were identified as having resulted in the publication or public docket release (National Transportation Safety Board, n/a) of tensile test data for TC128B steel. These accidents occurred in Lac-Mégantic, Quebec (Transportation Safety Board of Canada, 2013), Cherry Valley, IL (National Transportation Safety Board, 2012), and Lynchburg, VA (National Transportation Safety Board, 2016). The minimum, maximum, and average properties obtained from analyzing the tensile test data are summarized in Table 10 in Section 5.3.4.

TC128 elastic-plastic material responses were developed based on previous material modeling efforts for tank cars performed by Volpe (Rakoczy, P., & Carolan, M, 2016) (Rakoczy, P., Carolan, M., Gorhum, T., & Eshraghi, S., 2019) (Carolan, M., & Rakoczy, P., 2019). Pre-test TC128 elastic-plastic material responses were developed that approximated the minimum (lower bound) and maximum (upper bound) properties. Table F2 shows the lower and upper bounds of the collected test data along with the results from the calibrated FE models that were used to approximate the material response. Figure F4 is a plot of UTS and EB of the compiled TC128 test data (Rakoczy, P., Carolan, M., Gorhum, T., & Eshraghi, S., 2019) (Transportation Safety

116

Board of Canada, 2013) (National Transportation Safety Board, 2012) (National Transportation Safety Board, 2016) with the pre-test tensile coupon FEA results shown for comparison.

Table F2. Material Properties for Publicly Available TC128 Samples Compared with Pre-Test Tensile Coupon FEA Results

	TC128 Survey		FEA Results	
	Lower	**Upper**	**Lower**	**Upper**
Yield Strength (*ksi*)	55	66	57	63
Ultimate Strength (*ksi*)	78	89	85	89
Elongation-2 in (%)	28	43	31	42
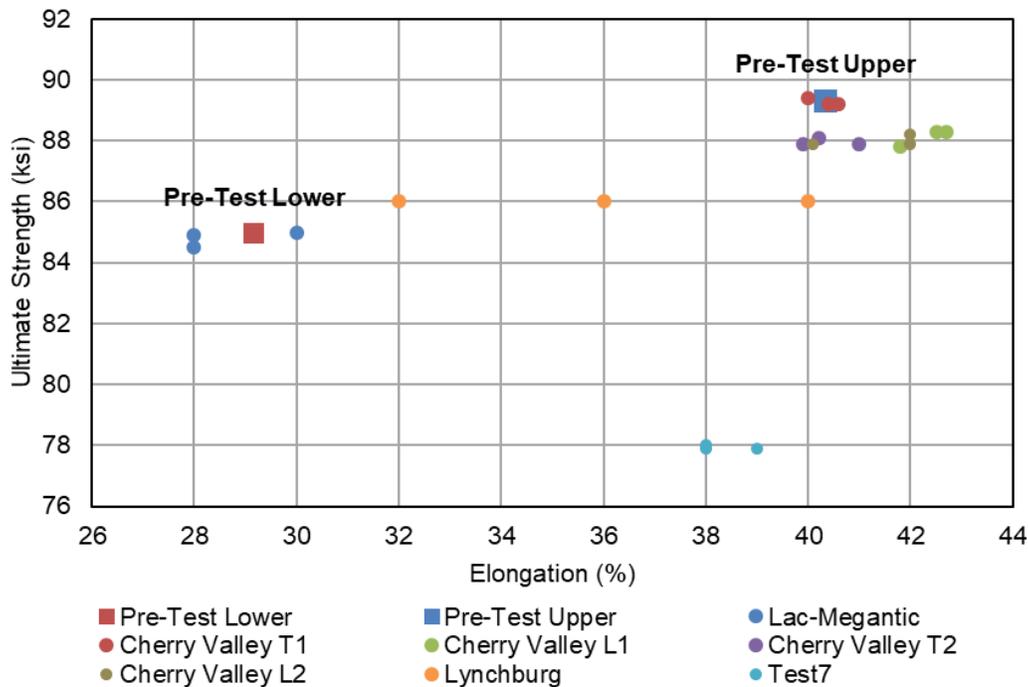
Figure F4. Ultimate Strength and Elongation at Break (2-inch gage) Tensile Properties from Publicly Available TC128 Tensile Data Compared with Pre-test FEA

In order to estimate the material response of the TC128 steel in the DOT-111 tank car to be tested, the plastic material behavior used in modeling a previously performed impact test (Test 2) (Kirkpatrick, S. W, 2010) was applied to an FE model of a 2-inch dog-bone tensile coupon (see Figure F1) which was then used to simulate a tensile test in Abaqus Explicit to measure the YS and UTS. The input plastic behavior was then iteratively changed until the resulting YS and UTS agreed with either the lower or upper bounds of the compiled TC128 data. The calibrated plastic material behavior inputs are shown in Figure F5 and Table F4.
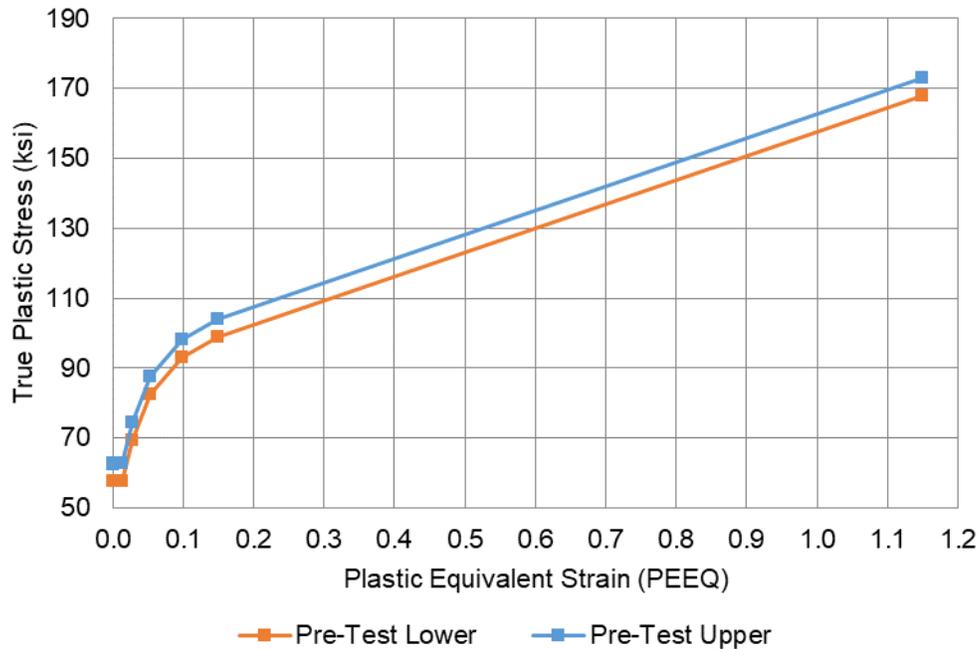
Figure F5. True Plastic Stress/Strain Behavior for Pre-test Lower and Upper Estimates of TC128 Steel

Table F4. True Stress/True Plastic Strain Inputs for Pre-test Lower and Upper Estimates of TC128 Steel Behavior

PEEQ in/in	Lower Estimate True Stress psi	Upper Estimate True Stress psi
0	57,500	62,500
0.000822	57,600	62,600
0.013	57,800	62,800
0.0276	69,500	74,500
0.0541	82,500	87,500
0.0987	93,200	98,200
0.149	99,000	104,000
1.15	168,000	173,000

The B-W damage initiation envelopes for the TC128 materials definitions used in the pre-test puncture models are shown in Figure F6. The damage initiation envelopes were calibrated in an iterative approach by using the B-W envelope developed for the post-test model of the DOT-117 (Rakoczy, P., Carolan, M., Gorhum, T., & Eshraghi, S., 2019) as a starting point and iteratively updating it while trying to achieve the desired strain at break. While the damage initiation envelope was being modified, the triaxiality value of the cusp (x_0) was constrained to occur at

118

the approximate average triaxiality of the fracture surface in the round bar uniaxial tension coupon model. The values for the hardening exponent (n) and critical strain to fracture in uniaxial tension (b) were manually adjusted while using Equation F3 and Equation F4 to recalculate the other constants for the B-W envelope during each iteration. The lower estimate was calibrated after three iterations and the upper estimate was calibrated after two iterations. The constants for the B-W damage envelopes are given in Table F3 and the curves are plotted in Figure F6.

Table F3. B-W Damage Initiation Envelope Constants for Pre-test TC128 Lower and Upper Estimates

B-W Constant	Lower Estimate	Upper Estimate
n	0.200	0.400
b	0.600	1.200
x_0	0.404	0.456
a	0.292	0.838
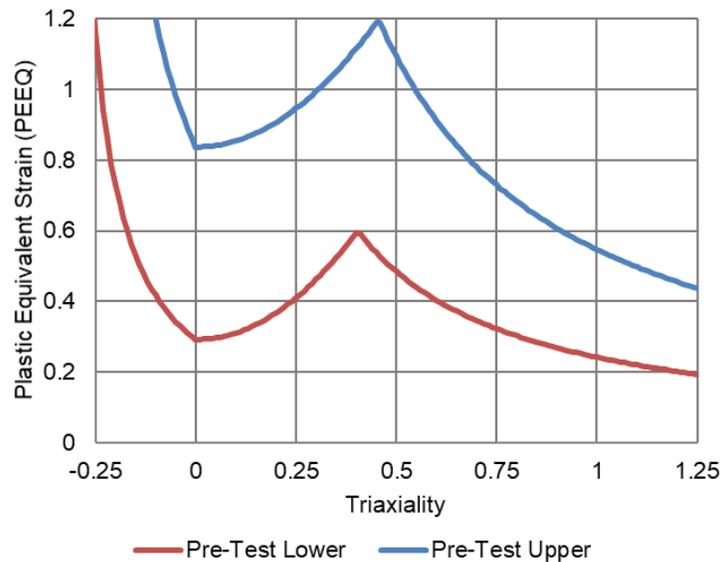
Figure F6. Damage Initiation Envelopes for TC128 from Pre-Test Models

The resulting engineering stress-strain responses from the 2-inch gage length dog-bone tensile coupon simulations are shown Figure F7. The engineering strains where damage initiated are marked with vertical dashed lines. Both the lower and upper estimates of TC128 used an energy-based linear damage progression in Abaqus/Explicit with a value of 1,200 in-lbf/in^2 which resulted in a moderately soft damage progression.
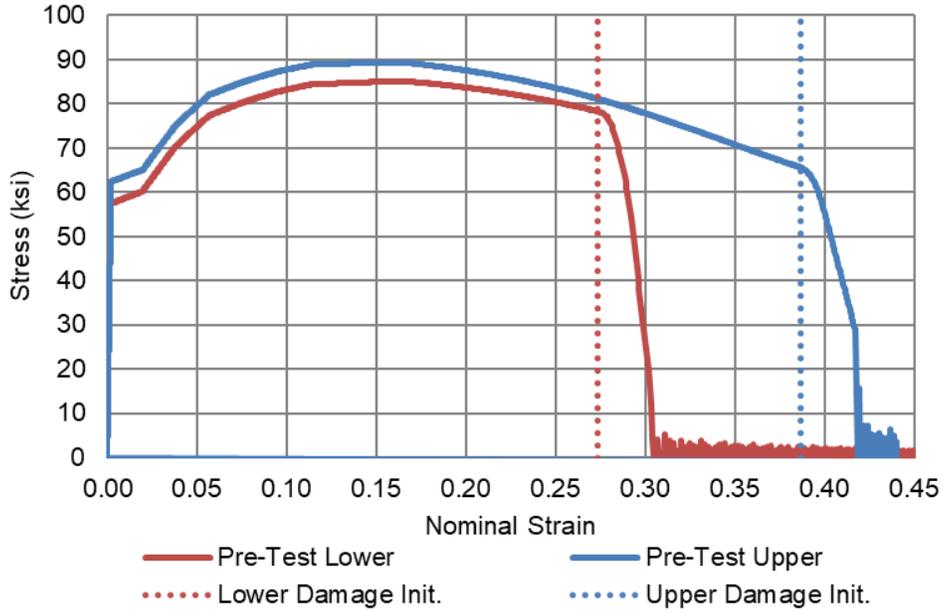
Figure F7. Pre-Test Engineering Stress-Strain Dog-bone Coupon (2-inch gage length) FE Results (solid) and Damage Initiation Engineering Strains (dashed)

F3.2 – Post-test Characterization

Following the test, material coupons were excised from the tested DOT-111 tank car and sent off for tensile testing. The material was cut into 1.4-inch gage length smooth round bars for tensile testing. The results of the tensile tests are included in Section B4. Additionally, the raw stress-strain data was provided to Volpe for use in developing a material response for the material in the tested tank car. Figure F8 contains a plot of the three-nominal stress-strain responses from the tested tank car. The straight lines at the end of each curve represent linear interpolation from the last data point measured by the load cell and extensometer to the reported EB from the test lab.
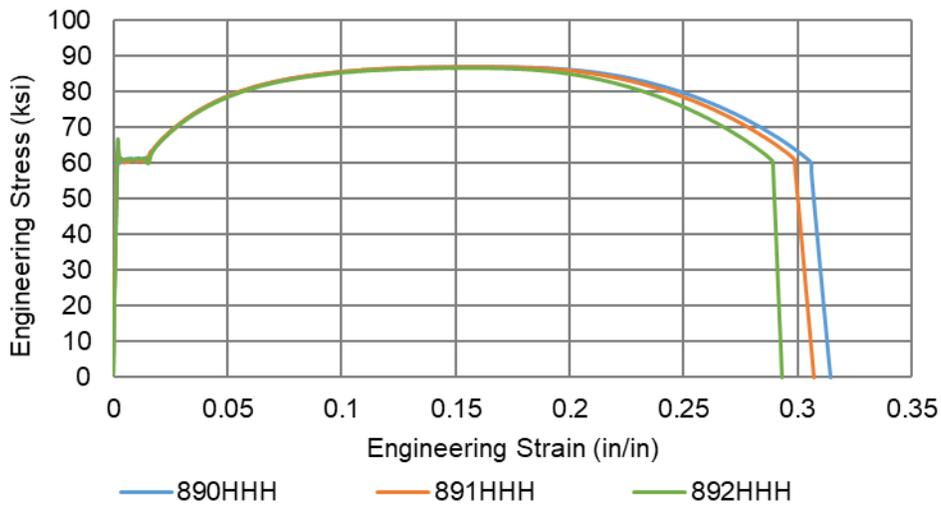

Figure F8. Smooth Round Bar (1.4-inch gage length) Test Results of Three Samples Extracted from Tested DOT-111 Tank Car

120

The nominal stress-strain characteristic of the mid-range tensile coupon (891HHH in Figure F8) was used to calculate (see Equation F1) a true stress-PEEQ input for the FE model. A discrete number of points were manually fit onto the true stress-PEEQ curve up to the UTS of the specimen. In the region after UTS, where necking dominates the response, the isotropic hardening of the material was estimated using a power law fit up to a large (1 in/in) strain. The power law equation is given in Equation F6, and the constants ($A = 134.149$ ksi, $n = 0.14876$) were determined by a least-squares regression on the true stress and PEEQ characteristic of the representative tensile coupon sample using a window of the test data prior to the UTS.

$$\sigma_{true}\left(\bar{\varepsilon}^{pl}\right) = A \cdot \left(\bar{\varepsilon}^{pl}\right)^n$$

Equation F6. Power Law Equation Used to Extrapolate True Stress at Large Strain

The start of the window was adjusted manually until the extrapolated plasticity input curve resulted in an output from the tensile coupon FE model that accurately represented the necking behavior observed in the test data. Figure F9 shows: (1) the calculated true stress-strain curve from tensile coupon 891HHH, (2) the windowed test data where regression was applied, (3) the extrapolated plasticity using the power fit equation, and (4) the calculated true-stress strain response from the tensile coupon FE model, which can be compared with the test data.
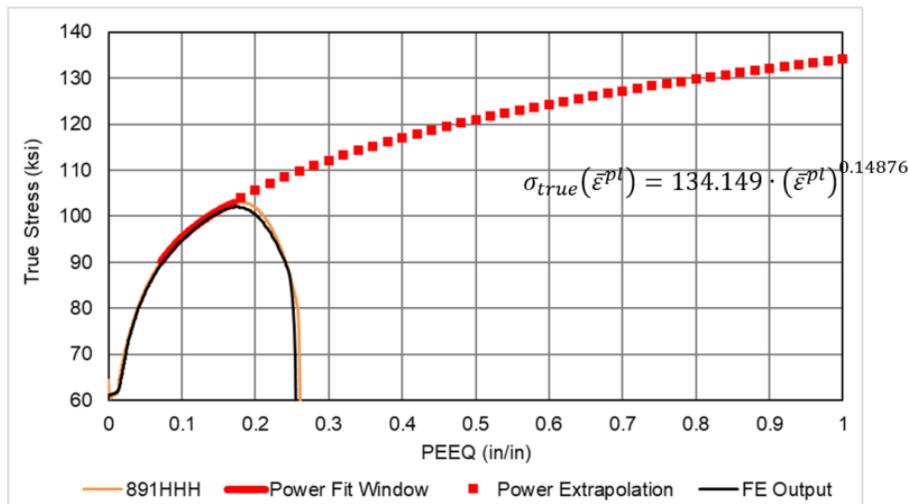
Figure F9. Calculated True Stress-Strain Characteristic of a Post-Test Tensile Coupon 891HHH (solid orange), Power Fit Window (solid red), Power Law Extrapolation (red squares), and FE Results (solid black)

Table F4 contains the tabular data used to define the isotropic plastic hardening of the TC128 material in the post-test FE model. The true stress response was extrapolated for large strains (according to Equation F6) starting at a plastic equivalent strain of 0.16 in/in, which was just before the UTS of the tensile coupon.

Table F4. True Stress and Plastic Equivalent Strain Inputs for Post-Test TC128 Material

True Stress ksi	PEEQ in./in.	True Stress ksi	PEEQ in./in.	True Stress ksi	PEEQ in./in.	True Stress ksi	PEEQ in./in.
61.50	0	102.1385	0.16	118.726	0.44	127.7507	0.72
61.50	0.0065	103.9439	0.18	119.5138	0.46	128.2725	0.74
61.50	0.013	105.586	0.20	120.2728	0.48	128.7824	0.76
65.75	0.016	107.0937	0.22	121.0054	0.50	129.281	0.78
69.00	0.020	108.4889	0.24	121.7135	0.52	129.7688	0.80
72.25	0.025	109.7885	0.26	122.3988	0.54	130.2464	0.82
75.25	0.030	111.0055	0.28	123.0628	0.56	130.7141	0.84
80.25	0.040	112.1507	0.30	123.7069	0.58	131.1725	0.86
84.00	0.050	113.2327	0.32	124.3324	0.60	131.6219	0.88
87.25	0.060	114.2585	0.34	124.9403	0.62	132.0626	0.90
89.75	0.070	115.2342	0.36	125.5318	0.64	132.4952	0.92
93.75	0.090	116.1648	0.38	126.1078	0.66	132.9197	0.94
97.50	0.115	117.0546	0.40	126.6691	0.68	133.3367	0.96
100.50	0.140	117.9072	0.42	127.2165	0.70	133.7463	0.98

Figure F10 shows the true stress-PEEQ inputs for Abaqus in the pre-test (lower and upper estimates of TC128) and post-test models. The pre-test and post-test input plastic behaviors are similar up to a PEEQ of 0.4 in/in but diverge afterward due to the pre-test models using linear extrapolation and the post-test model using a power law extrapolation at large strains.
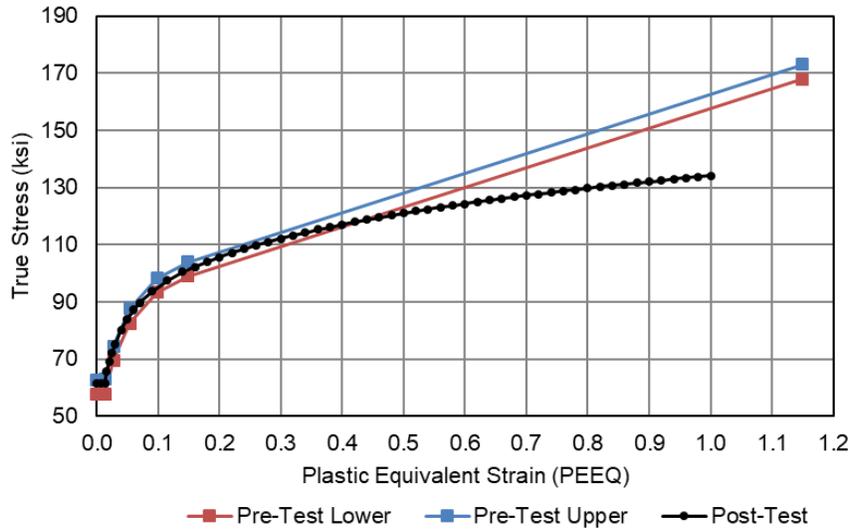
Figure F10. True Stress-Plastic Equivalent Strain Abaqus Inputs for Pre-Test (lower and upper) and Post-Test TC128 Models

Table F5 contains the B-W damage initiation envelope constants (refer to Equation F3) used to define the damage initiation envelope of the post-test TC128 material. The damage initiation envelope was calculated based on the Lee-Wierzbicki quick calibration procedure (Lee, Y., & Wierzbicki, T., 2004) (Lee, Y.-W., 2005) using the average mechanical properties (see Section F2) from the round bar tensile coupon samples that were cut from the tank shell after the side

impact test. The hardening exponent calibrated for the plasticity model (0.14876) was not used in the quick calibration procedure. Instead, the hardening exponent (0.14632) used in the quick calibration procedure was calculated according to Equation F4 but still resulted in a similar value. The damage progression was specified as energy-based with linear softening and maximum degradation, and the fracture energy was set to 300 in-lbf/in^2.

**Table F5. Damage Initiation Envelope for Post-Test TC128 Material**

B-W Constant	Post-Test
a	0.423558
b	1.132035
x_0	0.522706

Figure F11 compares the pre- and post-test B-W damage initiation envelopes. For Mode III-Shear Fracture and Mode II-Mixed Fracture, the post-test envelope lies between the lower and upper pre-test estimates of TC128. In Mode III-Ductile Fracture, the post-test envelope is nearly identical to the pre-test upper estimate.
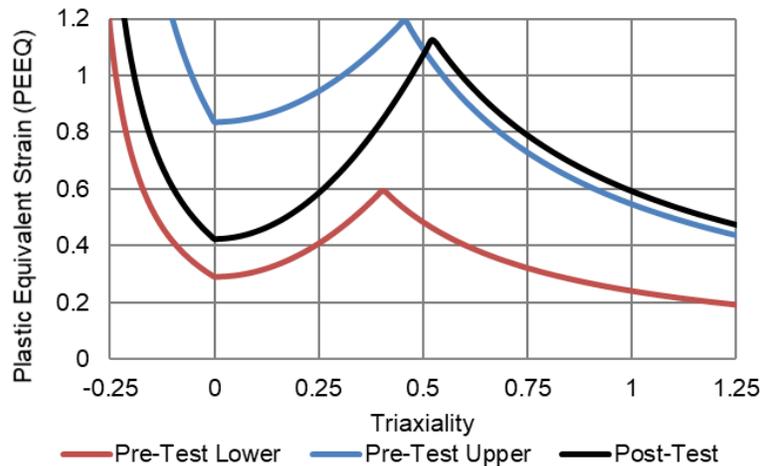
Figure F11. B-W Damage Initiation Envelopes from Pre-Test (lower and upper estimates) and Post-Test TC128 Material Behaviors

Figure F12 shows the engineering stress-strain response from a simulation of a uniaxial tension smooth round bar simulation with a 1.4-inch gage length. By comparing the simulation result (solid black line) with the uniaxial test results (solid color lines), it was observed that the true stress-PEEQ input resulted in an engineering stress-strain output that agreed with the test data up to crack initiation, and the quick calibration procedure resulted in a suitable threshold for damage initiation (dashed red line).
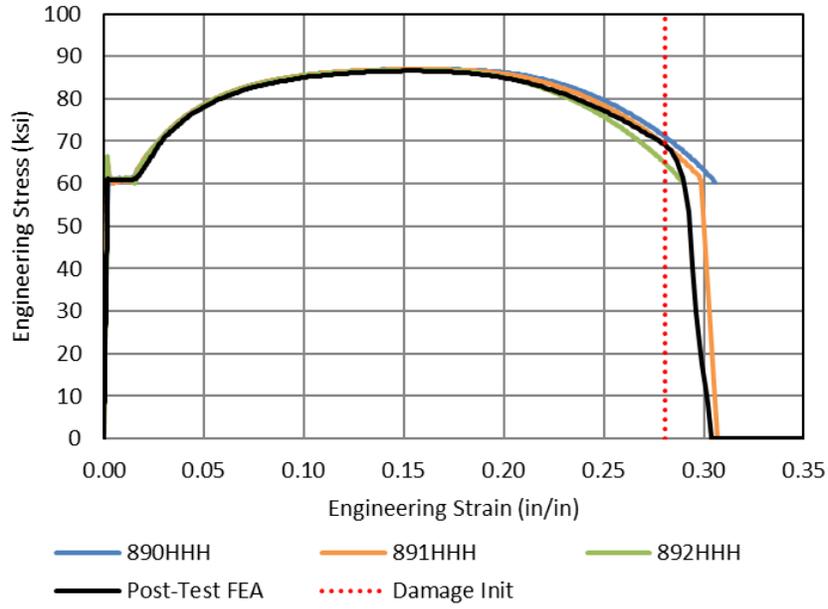
Figure F12. Engineering Stress-Strain Response from the Post-Test Smooth Round Bars (1.4-inch gage length); FE Model (solid black); Test Data for Comparison (solid colors); FE Model Damage Initiation also Shown (dashed red)

Abbreviations and Acronyms

ACRONYMS	EXPLANATIONS
AAR	Association of American Railroads
B-W	Bao-Wierzbicki
CFC	Channel Frequency Class
DOF	Degrees-of-Freedom
DOT	Department of Transportation
EB	Elongation at Break
EOS	Equations of State
FE	Finite Element
FEA	Finite Element Analysis
FPS	Frame Per Second
FRA	Federal Railroad Administration
HD	High Definition
HS	High Speed
PEEQ	Plastic Equivalent
PHMSA	Pipeline and Hazardous Materials Safety Administration
PRV	Pressure Relief Valve
SAE	Society of Automotive Engineers
SCFM	Standard Cubic Feet per Minute
SPH	Smoothed Particle Hydrodynamics
SSC	Shell-to-solid Coupling
TC	Transport Canada
TTC	Transportation Technology Center (the site)
TTCI	Transportation Technology Center, Inc. (the company)
UST	Ultimate Strength
Volpe	Volpe National Transportation Systems Center
YS	Yield Strength